Internal Report
DESY F1-88-01
September 1988

Analysis of B–jets in Electron–Positron Annihilations at 35 GeV CM Energy

J. M. Pawlak

Analysis of B-jets in Electron-Positron Annihilations at 35 GeV CM Energy.

Jerzy Michal Pawlak

A thesis submitted in partial fulfillment of the requirements
for the degree of Doctor of Philosophy (Physics)
at the Warsaw University.

September 1988

Abstract

A technique for tagging the b quark events produced in e^+e^- annihilation has been developed. The metod is based on a reconstruction of the decay vertices of the relatively long-living B hadrons. The technique is general in nature and can be applied at any detector with sufficient tracking precision. When applied to the data collected by the TASSO detector at 35 GeV CM energy, the method yielded a sample of 806 tagged jets with estimated b content of $64 \pm 8\%$. The tagged sample was used to measure the kinematical properties of the b quark jets created in the e^+e^- annihilations, and to compare them with predictions of the LUND fragmentation model version 6.3. The electroweak induced forward-backward asymmetry in the b quark production was measured to be $A_{b\bar{b}} = -0.14 \pm 0.14 \pm 0.04$, to be compared to the Standard Model prediction of -0.24 ± 0.03.

Contents

List of Figures

Chapter 1

Introduction

Experiments at e^+e^- colliding beam accelerators have proven to be a unique tool in studying certain aspects of high energy particle interactions. The basic reaction studied by those experiments is the e^+e^- annihilation into a virtual photon (or Z^0) followed by a fermion pair production. The Feynmann diagrams corresponding to those processes are shown in figure 1.1.

At centre-of-mass energies much below the Z^0 mass the contribution from the Z^0 exchange can be neglected. The Quantum Electrodynamics (QED) allows then to compute the cross-section for the first process pictured in fig. 1.1 as

$$\frac{d\sigma}{d\Omega} = \frac{\alpha^2}{4s} Q_f^2 \beta [1 + \cos^2\theta + (1 - \beta^2)\sin^2\theta]$$

where s denotes the center-of-mass energy squared, Q_f is the fermion electric charge, β is the final state fermion velocity and θ is the angle between the incoming electron and the outgoing fermion. Integrating the above formula over the full solid angle and putting $\beta = 1$ (i.e. neglecting the fermion mass in comparison with its energy) one can obtain the lowest order formula for the total fermion pair production cross-section

$$\sigma(e^+e^- \to f\bar{f}) = \frac{4\pi\alpha^2}{3s} Q_f^2 \approx \frac{86.5\, Q_f^2}{s\,[\mathrm{GeV}]}\ \mathrm{nb}$$

This formula is valid for any fermion f except the electron. For quarks the formula gives the cross-section for one colour state, to obtain the total quark production cross-section one has to multiply the above cross-section by 3. For the process $e^+e^- \to e^+e^-$ (Bhabha scattering) one has also to include in the calculation the diagram with t-channel photon exchange.

The above formulae show already the main experimental feature of e^+e^- interactions: at high energies (after passing any threshold effects) the cross-sections for different fermion pairs are of the same order of magnitude. This makes e^+e^- experiments an ideal tool to study the physics of higher fermion generations. Also, the angular distribution of resulting fermions is quite uniform - this makes it easier to detect and identify reaction products, but also calls for detectors covering as large part of the solid angle as possible.

Including the Z^0 exchange diagram modifies the cross-section. At PETRA energies the correction to the total cross-section is however small, the main modification appears in the θ distribution of the outgoing fermions, through appearance of the term proportional to $\cos\theta$. Another important correction to the above cross-section comes from the radiative effects. The most important diagrams contributing to the corrections are the initial or final state bremsstrahlung diagrams, pictured in figure 1.2.

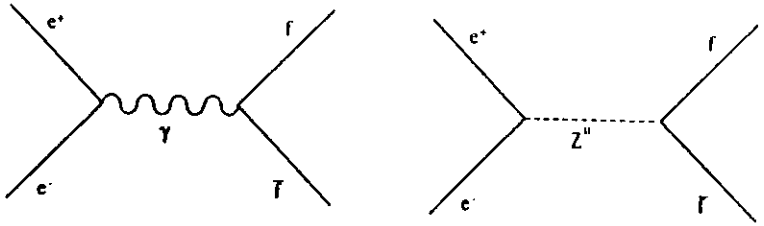

Figure 1.1: Lowest order Feynmann diagrams contributing to the process $e^+e^- \to f\bar{f}$.

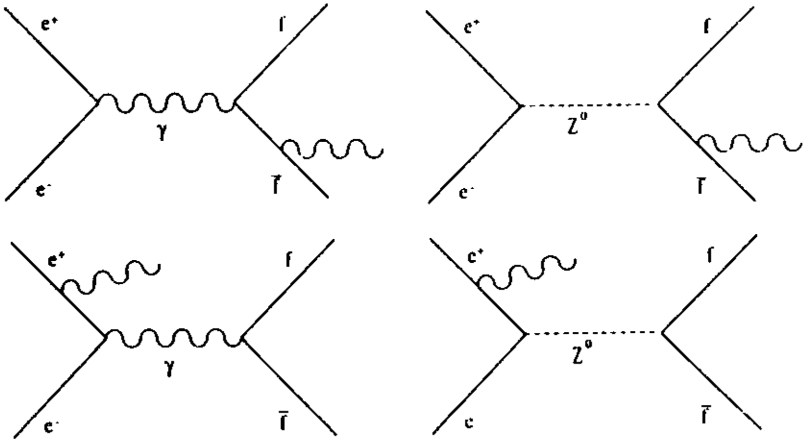

Figure 1.2: Diagrams contributing to the $O(\alpha^3)$ radiative corrections to the fermion pair production. Only generic diagrams are shown.

The b quark is the heaviest quark known by now. Its partner, the t quark has not been up till now seen experimentally – although its existence is essential for the electroweak theory to be renormalisable.

The b quark has been discovered, as a $b\bar{b}$ bound state, in 1977 by finding a bump in the invariant mass distribution of $\mu^+\mu^-$ pairs created in hadronic collisions [1]. The discovery was quickly confirmed by e^+e^- experiments at DORIS [2] by observation of narrow peaks in the cross-section for the reaction $e^+e^- \to$ hadrons. The peaks have been interpreted as resulting from the production and decay of $b\bar{b}$ bound states with $J^{PC} = 1^{--}$ (Υ states). Of the Υ family the most interesting is the fourth resonance called $\Upsilon(4S)$. It width is much higher than the width of the lower three resonances – this indicates that the $\Upsilon(4S)$ can decay strongly into a pair of B hadrons. The mass difference between the $\Upsilon(4S)$ and the two B hadrons was measured to be about 60 MeV – this is not enough to produce any additional hadrons in the decay The $\Upsilon(4S)$ is thus a beautiful laboratory for studying the B hadron properties.

Today, ten years after the discovery, the b quark physics is still a comparatively little explored territory. The experiments running at the $\Upsilon(4S)$ resonance were able to fully reconstruct a small number of B_u^- and B_d^0 meson decays [3,4,5] (the subscripts u and d stand for the flavour of the bound antiquark) and measure their masses. No excited B meson states or B baryons have been observed. The exclusive decay branching ratios have been measured only for a few of the simplest decay modes – on the other hand the B decay multiplicity is known to be quite high. Two important recent discoveries are the observation of mixing phenomena in the B^0 - $\bar{B}^0$ system [6] and observation of the charmless decays of B mesons [7]. Still missing are more precise measurements concerning both those phenomena.

The high-energy e^+e^- experiments at PEP and PETRA also contributed to the b quark physics. They found the B hadrons to be relatively long-lived (the recent compilation of the average lifetime gives 1.18 ± 0.14 ps [8] measured for an unseparated mixture of various B hadron species). This fact alone allowed to establish that the mixing between the third generation and the lower two ones is weaker than the mixing between the first two generation. Together with the results on electron spectra and charmless B decay from $\Upsilon(4S)$ experiments this result indirectly measured the KM mixing matrix elements V_{bc} and V_{bu}. On the other hand virtually nothing is known about the individual lifetimes of various B hadron species – this comes from experimental difficulties associated with B hadron identification at high energies.

The other b physics topic which is up till now a domain of high-energy e^+e^- experiments are the phenomena associated with the b quark production and its fragmentation. The experiments have established that the b quark fragmentation is hard, that means that a B hadron created in the fragmentation tends to carry a large fraction of the original b quark momentum. This effect was predicted by simple kinematical considerations [9]. Two experiments have attempted a more detailed study of the b quark fragmentation by trying to select events with $b\bar{b}$ production and studying their properties [10,11]. These experiments have not seen any unexpected effects, however their b event statistics was rather low, making more precise tests impossible. This work presents an attempt to improve the situation by using a somewhat larger b event sample.

The e^+e^- experiments have also studied the weak neutral current interaction of the b quark, by observing the asymmetry in the b quark production. Also here the results do not show any unexpected effects, but again due to low statistics the results are not very conclusive. A measurement of this type has been also performed and is presented in this work.

All the above mentioned measurements can be greatly improved by increasing the number of $b\bar{b}$ events used. Most of the analyses up till now operated on samples of at best a few hundred events. On the other hand most of the experiments have during their operation collected thousands of B's, the problem is to find them among all the hadronic events. A direct reconstruction of a B decay is a very difficult and inefficient technique in the moment feasible only at $\Upsilon(4S)$ experiments. High-energy experiments have up till now used either the high transverse momentum leptons or event shape variables for the purpose of $b\bar{b}$ selection. Both those methods have however their intrinsic limitations: the lepton method has its efficiency limited by the semileptonic branching ratio of the B decay, the event shape method has an inherent limitation on the purity of resulting b samples. A good method for tagging the B's will be even more needed at the future colliders – SLC, LEP and HERA will produce heavy quarks in great numbers.

One potentially very powerful technique of b event selection is the lifetime tagging technique, which uses the relatively long B hadron lifetime as a b quark signature. In this method an observation of a high multiplicity secondary decay among the reaction products is treated as a signal of a b quark production and subsequent decay. The work presented here is one of the first attempts to apply the lifetime tagging technique for b physics studies.

Chapter 2

Experimental Environment

2.1 The PETRA Storage Ring

The PETRA e^+e^- storage ring is located at the DESY laboratory in Hamburg (Germany). Officially proposed in 1974 the accelerator started operation in the end of 1978. During eight years of physics operation PETRA was the world highest energy e^+e^- machine, the record center-of-mass energy of 46.8 GeV was reached in 1984. The machine design energy was 35 GeV, and at this energy the majority of data were collected. The last PETRA e^+e^- run took place on 3. November 1986 – the ring was then rebuilt to serve as an injector for a new HERA ep collider currently under construction.

Figure 2.1 shows the layout of the DESY accelerator complex including the PETRA ring. PETRA has eight straight sections – four of them housed during physics running the particle detectors, the other four were occupied by accelerating cavities. Electron and positron beams were injected from the DESY synchrotron at the energy of 7 GeV per beam, then ramped to the desired energy by PETRA itself. The whole process of injection and ramping took typically less than half an hour. In the normal mode of operation two electron and two positron bunches were injected, the collisions occurred thus in four points on the ring circumference. The time between two successive bunch crossings at a given intersection point was 3.8 μs. Typical beam currents at the start of the run were between 10 – 12 mA. At 17.5 GeV beam energy the current was limited by single beam instabilities (satellite resonances) [12]. Under normal conditions the beam was dumped and the machine refilled after about four hours, the beam currents were by that time around 6 mA.

An important parameter of an accelerator is its luminosity L. The luminosity multiplied by a cross section for some particular interaction gives the rate at which this interaction occurs. In the case of an e^+e^- storage ring L may be expressed as

$$L = \frac{I^+ I^-}{4\pi e^2 f B \sigma_x \sigma_y}$$

where I^+ and I^- are the beam currents, e is the electron charge, f the revolution frequency, σ_x, σ_y are the beam sizes at the interaction point and B is the number of bunches in one beam. PETRA average luminosity at 35 GeV was about $1.5 \times 10^{31}\,\mathrm{cm}^{-2}\mathrm{s}^{-1}$. An integral of L over time, the integrated luminosity, delivered per day of smooth running reached 1 pb^{-1}.

For the purpose of this analysis it was important to know also the beam sizes at the interaction point. The beam size can be calculated from the machine parameters: amplitude functions β_i^* (which depend on focusing) and emittances ϵ_i (which are complicated functions of the ring optics)

$$\sigma_i^2 = \beta_i^* \epsilon,$$

with $i = x, y$. The amplitude functions after installation of the so-called mini-beta focusing were $\beta_x^* = 120\,\mathrm{cm}$ and $\beta_y^* = 8\,\mathrm{cm}$. The ϵ's are much more difficult to calculate, they depend on the machine optics, imperfections in magnet positioning and on the degree optimisation of the machine. The optimisation was performed so to minimise $K = \epsilon_y/\epsilon_x$, as this gives highest luminosity. Reference [12] cites $K = 0.013$ as a value achieved with 17 GeV beam. Assuming this is rather a best case, $K = 0.02$ was assumed as average value. Using the average currents and luminosities one may estimate

$$\sigma_x \approx 400\,\mu\mathrm{m}, \qquad \sigma_y \approx 15\,\mu\mathrm{m}$$

consistent with values given elsewhere. This σ_x value is also consistent with the result of the measurement done at TASSO, described in chapter 3.4.

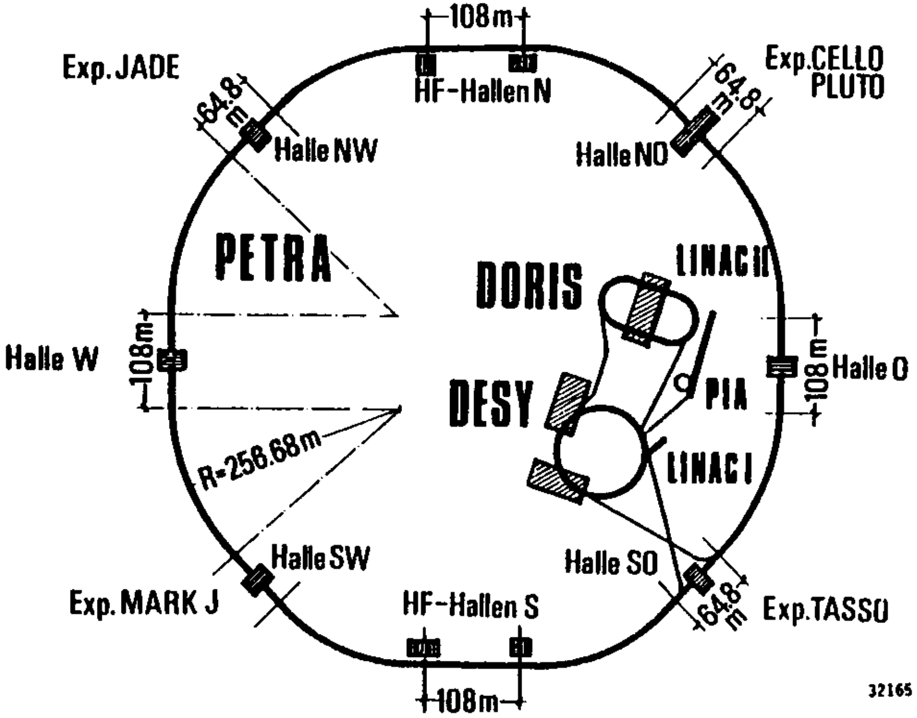

Figure 2.1: Layout of the DESY accelerator complex with the PETRA storage ring.

2.2 The TASSO Detector

The TASSO detector (Two Arm Spectrometer SOlenoid) was one of four big detectors operating at the PETRA storage ring. The name was given to it after its most prominent feature - two "hadron arms" for particle identification. Figures 2.2 and 2.3 present the detector in two different views.

The central part of the TASSO detector was placed in 0.5 T magnetic field of the solenoid coil. Inside the coil three tracking detectors were installed: the main drift chamber (DC), the central proportional chamber (CPC) and the precision vertex detector (VXD). Between the coil and the outer vessel of the drift chamber a layer of scintillator time-of-flight counter was located. The part of the detector outside the coil consisted, apart from the above mentioned hadron arms, of the liquid argon electromagnetic calorimeters and the muon detection system. Finally, in the forward region a system consisting of scintillators, proportional chambers and lead-scintillator shower counters was installed. These detector components which are relevant to this analysis will be now described in some detail.

2.2.1 The Vertex Detector

This was the innermost part of the TASSO detector. The VXD was a high-precision pressurized drift chamber with eight layers of sense wires, and with the spatial resolution of about 100 μm. Due to its fundamental role in the analysis presented in this work, the vertex detector will be described in detail in the next section.

2.2.2 Central Proportional Chamber

The Central Proportional Chamber (CPC) [13] was the next component of TASSO encountered by the track coming from the interaction point. It had four sense layers located at radii between 18 and 29 cm. Each sense layer had 480 axial anode wires providing the $r-\phi$ track information and two sets of helical cathode strips, 120 strips per set, wound in opposite directions at an angle of 36.5°. The cathodes together with the anode wire information allowed to reconstruct the z position of the tracks passing the CPC.

The CPC played an important role in the triggering system. A special hardware processor [14] was built to make a quick search for track elements among the anode hits. The processor returned the search results as 48 bits, marking the ϕ sectors containing the track candidates. Another processor was fed with the cathode strip information – its role was to locate the event origin in z. This information was then used by the triggering system as an aid in beam-gas events rejection for certain types of triggers.

2.2.3 Drift Chamber

The big Drift Chamber (DC) [15] was the largest inner component of the detector and its main charged particle tracking device. It had 2340 sense wires of 3.5 m length located in 15 cylindrical layers. The first layer had 36.7 cm radius and 72 sense wires, each next layer had 6.11 cm larger radius and 12 more wires than the preceding one. This arrangement made all the drift cells to have the same dimensions, the cell structure is shown in fig. 2.4. The anode sense wires were 30 μm diameter gold-plated tungsten, the field shaping wires were 120 μm gold plated molybdenium. An aluminium vessel together with an epoxy-fiberglass laminate inner tube provided the mechanical rigidity and enclosure of the construction. The

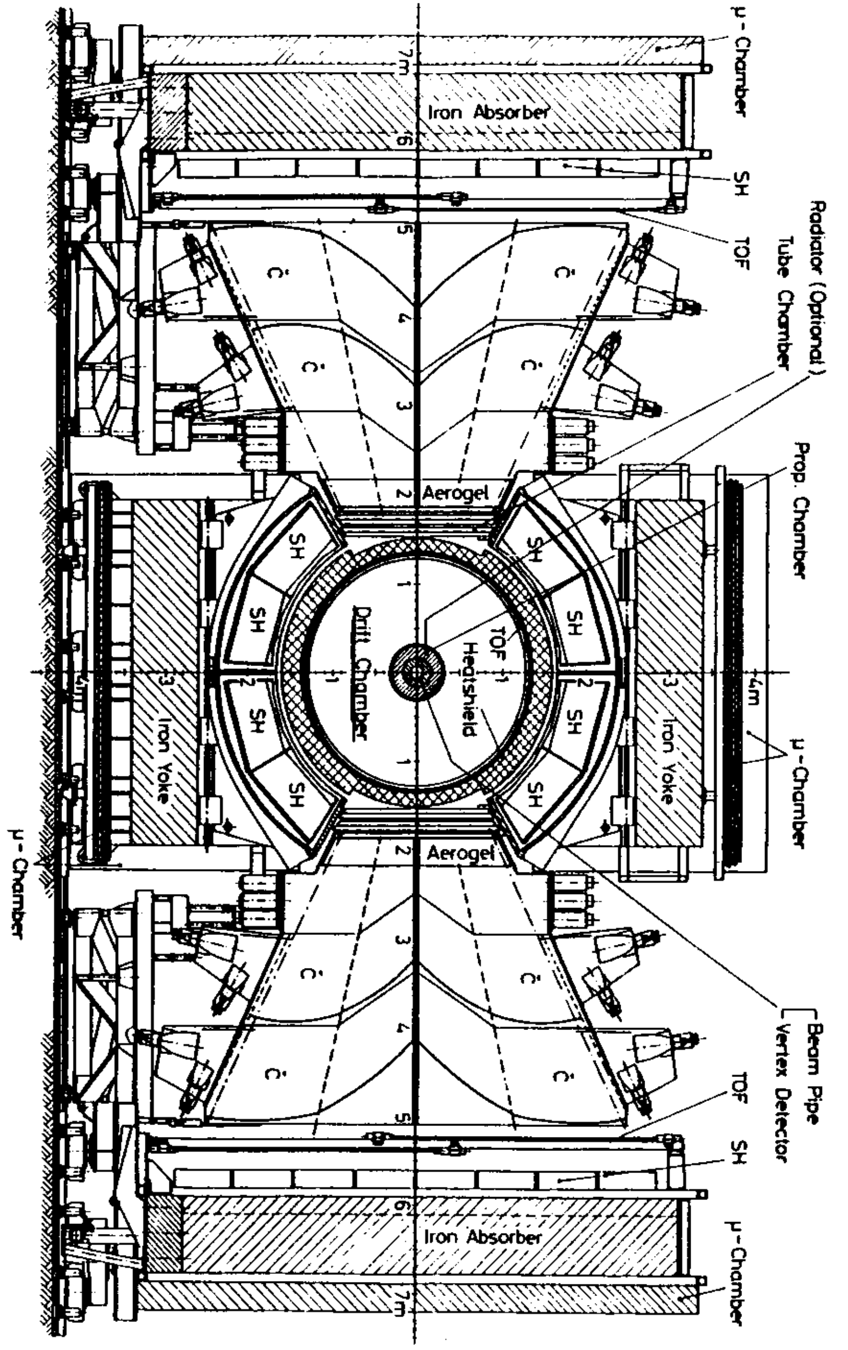

Figure 2.2: The TASSO detector - section perpendicular to the beam.

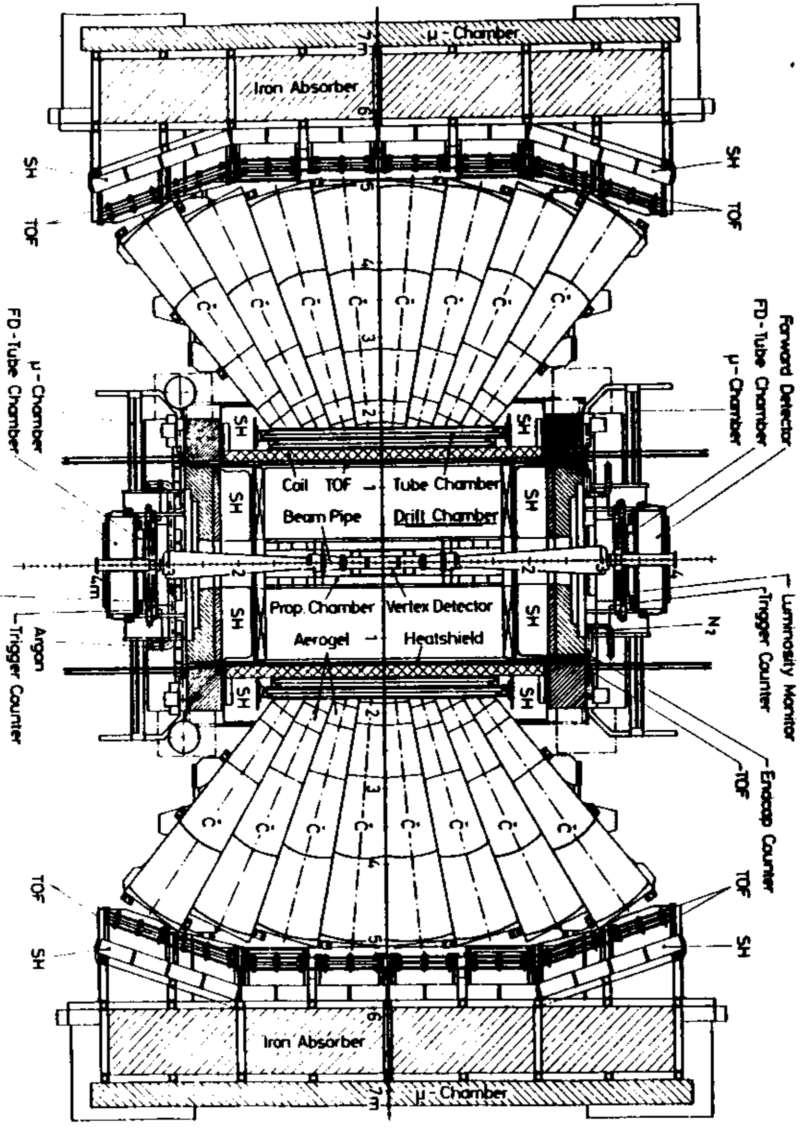

Figure 2.3: The TASSO detector - top view.

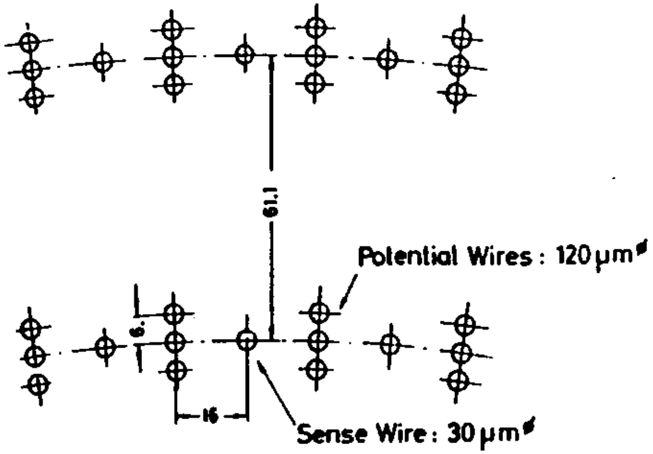

Figure 2.4: Cell structure of the Drift Chamber.

chamber operated with the gas mixture of 50% Ar and 50% CO_2, at 2400 V. This gas replaced the original 90% Ar + 10% CH_4 mixture cited in [15], reducing the cross-talk between neighbouring cells and improving the resolution at the cell edges.

Nine of the chamber layers had the wires strung in the axial direction while in the other six layers the wires made a small angle (3.4 – 4.5°) with the chamber axis (so-called stereo layers). The stereo layers were the only source of three-dimensional information about the tracks in the standard TASSO track reconstruction.

The spatial resolution achieved was about 200 μm for separated tracks at normal incidence angle [16]. To achieve this resolution non-linear drift-time corrections were applied in order to correct for electric filed inhomogenities at the edge of a cell. The total hit efficiency (including the efficiency of the electronics) was 98%. The momentum resolution achieved was $\sigma_{p_\perp}/p_\perp^2 = 0.02$ when fitting to the drift chamber alone and $\sigma_{p_\perp}/p_\perp^2 = 0.011$ if a beam spot constraint was added in the fit, for tracks found in the muon pair production events.

Another important quantity affecting the chamber performance is the amount of material which the track must traverse before reaching the sensitive volume. More material degrades the momentum resolution by multiple scattering effects and introduces additional background tracks from γ conversions. In the configuration with the vertex detector this amounted to about 0.08 radiation lengths - mostly in form of the aluminum outer pressure vessel of the VXD and the CPC suspension system.

In addition to its tracking tasks, the DC participated also in the triggering system. A hardware processor called PREPRO was built for this purpose and connected to six of the 0° layers of the chamber. For each of the 72 wires of the inner DC layer PREPRO had a set of predefined masks which indicated which wires in other five layers should be hit by different momentum tracks coming from the interaction point. PREPRO accepted the track if for a mask at least 5 of 6 wires were hit. The efficiency of PREPRO track finding for high momentum tracks was about 95%. In the trigger it was usually required that the PREPRO track should be accompanied by a CPC processor track and an inner time-of-flight (ITOF) counter hit.

2.2.4 Inner Time of Flight System

Between the outer drift chamber vessel and the solenoid a set of 48 scintillator time-of-flight counters was installed. The scintillators had 390 cm length and were viewed on both sides by photomultipliers, each photomultiplier read out with two TDC-s (high and low-gain). The timing resolution depended on the position of the track along the scintillator strip, average resolution was measured to be about 380 ps. These counters were used for particle identification and in the triggering system.

2.2.5 Outer Detectors

The outer components of TASSO were scarcely used in this analysis and will be described only very briefly.

An electromagnetic calorimeter was installed outside the coil, on the top and bottom of the detector. It was built of lead stacks with liquid argon as an active medium. The calorimeter consisted of 8 identical modules, had a depth of 14 radiation lengths and resolution of $\sigma_E/E \approx 13\%/\sqrt{E}$ for photons. It was used to identify electrons and to detect photons. Two similar construction endcap calorimeters occupied the regions at both ends of the coil, providing electron and photon detection capability in the forward and backward regions.

The hadron arms covered about 20% of 4π. The detector system of each arm consisted of a set of planar tube drift chambers, three Čerenkov counters filled witch aerogel (refractive index $n = 1.025$) freon 114 ($n = 1.0014$) and CO_2 ($n = 1.00043$), a layer of time-of-flight scintillators and a lead-scintillator calorimeter (shower counter). The Čerenkov counters allowed for $\pi : K : p$ separation up to the highest particle momenta.

Behind the iron yoke of the magnet and in the hadron arms behind iron walls, muon chambers were installed. They consisted of four layers of aluminum proportional tubes, two in each direction. The total coverage of the muon system was 43% of 4π, minimal muon momentum needed to reach them was 1.2 GeV/c.

Forward detectors were installed close to the beam pipe on both sides of the experiment. They consisted of scintillator counters, proportional chambers and lead-scintillator shower counters. These detectors were used to measure luminosity by identifying electrons from Bhabha scattering and as an aid in studying $\gamma\gamma$ processes.

2.3 The TASSO Vertex Detector

The Vertex Detector [17] was installed in TASSO at the end of 1982. This installation improved the tracking precision allowing to measure the lifetimes of heavy flavour particles, and also made plausible the idea of resolving the secondary decay vertices of heavy flavour decays. Figure 2.5 shows the VXD mounted inside the detector.

As already mentioned, the vertex detector was a small pressurized drift chamber, with 8 axial layers of sense wires. The four inner layers located at radii 8.12 to 10.22 cm had 72 sense wires each, the outer four with 108 sense wires each were located between 12.82 and 14.92 cm from the detector axis. The wires were 20 μm gold plated tungsten, aligned with 15 μm precision in the azimuthal direction. The anodes were separated by pairs of cathode wires which defined the cell structure. Figure 2.5c shows a fragment of the VXD end flange with the cell structure visible. The wires in successive layers were staggered by half a cell - this feature should aid in resolving the left-right hit ambiguity during pattern recognition

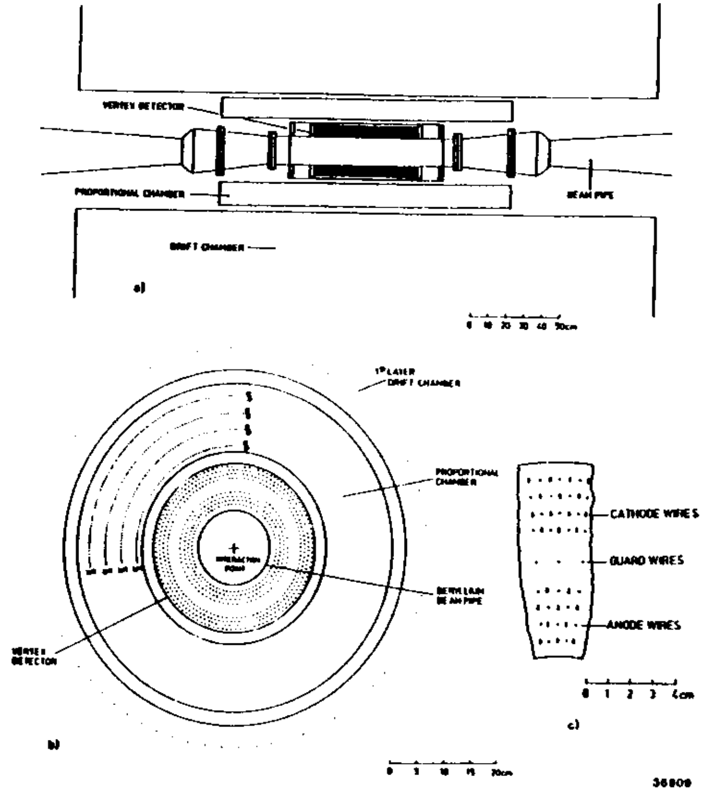

Figure 2.5: The TASSO Vertex Detector
a,b - two views of the VXD mounted inside the detector
c - fragment of the VXD end flange showing the cell structure.

and also assure that tracks pass different layers at different distances from the wires. The last point is important in case the resolution depends on the region inside the cell passed by the track - it ensures that no systematic bias appears in the track reconstruction.

Mechanically the chamber was mounted directly on the beryllium beam pipe - beryllium was chosen in order to minimise the radiation depth of material before the chamber. The beam pipe had inner radius of 6.67 cm and 0.18 cm thickness. A thin copper film on the inside of the pipe should absorb the synchrotron radiation coming with the beam. The end-flanges were made of aluminum as well as the outer pressure vessel. The active length of the chamber was 57.2 cm. A layer of capton foil inside the detector isolated a part of its volume next to the beam pipe. It was originally planned to fill this area with Xenon gas which should absorb low energy photons emitted from the beam pipe copper coating excited by synchrotron radiation. The synchrotron radiation background turned out, however, to be lower than anticipated and the Xenon chamber was not needed - it was therefore filled with the same gas as the rest of the chamber. The gas mixture used was 95% Ar and 5% CO_2 with an admixture of water and ethanol. The gas pressure was 3 bar.

The anode wires were kept at high potential, about 2800 V. The exact setting of the high voltages varied somewhat from layer to layer, the optimum value was found from the plateau curves taken in cosmic runs. The hit efficiency reached with this voltage setting was about 99% (excluding the dead wires). The efficiency was somewhat lower in even-numbered layers than in the odd-numbered, the reason was the mapping of the HV supplies on the chamber. There were 48 power supplies, each of them fed the wires located in a 30° sector and belonging to two successive layers. As a consequence, the two layers had always the same voltage setting. The larger drift cells in outer layer of the pair demanded however slightly higher voltage in order to keep the same gain. Lower gain led to efficiency losses on the cell edges.

To reduce the field shape disturbance in the cells belonging to the inmost and outmost layers, two equipotential planes were introduced at radii 7.5 cm and 15.4 cm. These layers were kept at 1 kV potential.

The VXD readout system was somewhat different for layers 1, 2, 5 and 6 than for the other four. The wires were read from one side only, the other end of the wire was kept open. The signals were amplified, fed into constant fraction discriminator and then into a commercial TDC system. The system operated in a "common stop" mode - individual TDC's were started by the pulses from the chambers, the stop signal was derived from delayed beam pickup strobe. The TDC scale was 0.5 ns/count.

In layers 3, 4, 7 and 8 the wires were read from both sides. The same TDC readout was used, but in addition to it two ADC's analysed the amplified signal from both ends of the wire. It was planned to use these ADC's to get a z coordinate measurement by charge division. The precision obtained turned out however to be too low and this feature was not used in the standard track reconstruction.

The Vertex Detector had also its own trigger processor searching for track candidates. The short length of the VXD gave it small acceptance for tracks coming from beam-gas interactions, while leaving the solid angle coverage similar to that of the other tracking devices. The VXD participated therefore in a low multiplicity track trigger, rejecting events with no tracks coming from the interaction point.

Calibration

To find the spatial coordinates of hits in the detector a relation between the measured drift time and the drift distance was needed. This relation was provided by the offline calibration tasks.

The hit coordinate was calculated from the TDC count by calculating first the drift time

$$t = s(T_0 - T)$$

where s is the TDC scale (0.5 ns/count) and T_0 is a common TDC start count (i.e. count for 0 drift distance). For calibration purposes and for precision track fits t was additionally corrected for the particle flight time and signal propagation time along the wire. Those corrections could be however applied only if the hits were already associated with known tracks - otherwise the z coordinate of the hit (needed to find the corrections) was not known. t was then translated into drift distance x by a third order polynomial:

$$x = a_0 + a_1 t + a_2 t^2 + a_3 t^3$$

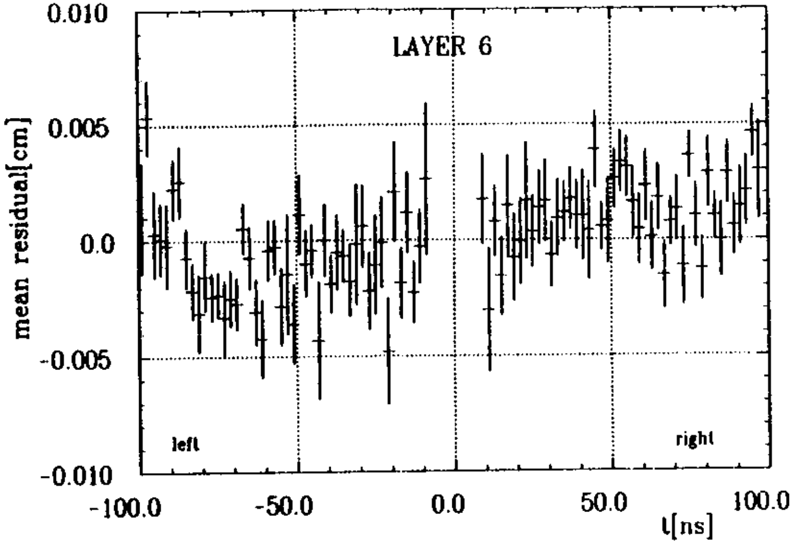

Figure 2.6: Average residuals of the VXD tracks in one of its layers.

a_i are the calibration constants to be determined. As each of the VXD layers had a different electric field (due to voltage and cell size differences) each layer needed its own set of calibration constants. The presence of the a_0 term in the formula ensured that T_0 did not need to be precisely determined - in fact T_0 was usually found by eye examination of the TDC distributions.

The calibration was performed periodically, depending on the amount of data collected. In 1986 this was done every 100 - 200 runs. A sample of clean high energy two-prong events (mostly Bhabhas) was first selected. For these events the spatial hit coordinates in the VXD were calculated using the calibration from the previous run period. The TDC count distribution for the hits seen in these events was then examined to find the T_0 value and to check its stability (in the early VXD runs rapid T_0 jumps of unknown origin were sometimes observed). In 1986 the T_0 was found however to be very stable.

The PASS 5 algorithm (see section 3.2) was then applied to fit the tracks to the VXD hits found. The residuals of the hits $d_i = x_i^{track} - x_i^{hit}$ were then calculated and a new constants set minimising the residuals was found. The tracks were then refitted to the new hit coordinates and the entire procedure was iterated until the values were stable. Figure 2.6 shows the track residuals as a function of the drift time t (negative t indicates hit in the left half of the cell) for one of the layers. The figure shows that the mean residuals are indeed consistent with zero in all regions of a drift cell. The figure offers thus some justification for the assumed form of the space-drifttime relation. A small systematic difference between the left and right cell halves is probably caused by a small ($\sim 15\,\mu m$) misalignment between the different VXD layers.

The above described calibration enabled already to fit the tracks in the VXD coordinate system. In order to fit the tracks globally to all the tracking devices one additional step has to be taken -- the relative positions of the detectors must be known. This is true, especially

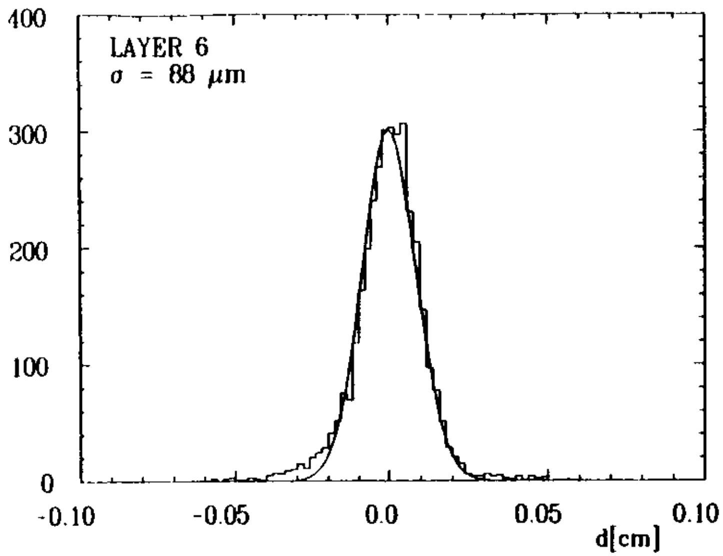

Figure 2.7: Distribution of the track residuals in one VXD layer obtained with Bhabha scattering events. Solid curve shows the gaussian fit.

as the VXD was not attached firmly to other detectors. The alignment between them had therefore to be continuously controlled.

To fully describe the position of the VXD in the drift chamber coordinate system six parameters are needed: three translations x_v, y_v, z_v and three Euler angles α_1, α_2, α_3. Out of those z_v is unimportant for the analysis as the vertex detector did not provide any track z information. The alignment parameters were determined from the data, with the same frequency as the space-drifttime relations and using the same sample of Bhabha events. The track parameters obtained from the Drift Chamber fit were compared with those given by the Vertex Detector fit, in attempt to find a set of positions which will minimise the differences. Three algorithms, differing by the choice of the comparison criteria and numerical approach, were used. The alignment constants were considered final if all three methods agreed on the result. Judging from the differences between the results of different methods, the precision of the relative alignment was $\sim 10\,\mu$m.

Operating Conditions

Three parameters affect the precision of the measurements done with the VXD: its spatial resolution, number of noise hits and the chamber efficiency. All of them have been carefully studied in the data, the goal of these studies was twofold: to get the best possible tracking precision by putting the resolution and noise data into track fitting programs, and to get the best description of the chamber behaviour for the detector simulation program. A very careful study of the VXD operating conditions was done by D. Su [18], the results relevant to this analysis are cited below.

Resolution: The spatial resolution was normally measured by making a distribution of the track residuals $d = x^{hit} - x^{track}$ for good tracks and making a gaussian fit to the distribution. x is here the distance from the wire, so d is negative if the hit was closer to the wire than a track. An example of such distribution obtained from two-prong events for one of the layers is shown in figure 2.7. The solid curve is the result of a gaussian fit to the central part of the distribution. The tail of the distribution at negative d comes probably from hits caused not by the track itself but by soft photons or δ electrons accompanying it. Due to the lack of multi-hit electronics such hits will be registered instead of the track position if they appear closer to the wire than the track.

The gaussian fits as shown in figure 2.7 gives however only some crude estimate of the resolution. One expects, for example, to find different resolutions in the Bhabha and hadronic events, due to different ionisation, different track momenta and pattern recognition problems in dense jets. These effects pull generally towards worse resolution in hadronic events. Another effect to be taken into account comes from the small number of layers in the VXD. The residuals in the figure were calculated from tracks fitted to the VXD including the layer examined – this of course biased the residual distribution. The correct procedure would be to calculate the residual from the track fitted with the hit in question excluded. Finally, it is expected that the resolution will vary across the drift cell, being worse close to the wire and at the cell edges (due to field inhomogenities and sampling length differences).

A study of the resolution taking into account the above effects was presented in [18]. The resolutions were inferred from the residual distributions of tracks with $p > 500$ MeV/c and 8 VXD hits found in the hadronic events. Resolution was measured as a function of the drift distance. It was seen that the tracks in hadronic events indeed give worse spatial resolution. Table 2.1 gives the values obtained for tracks at "middle" distance from the wire. In the other cell regions the resolution was worse by up to 25%, in the region very close to the wire (where ionisation fluctuations play most important role) 46% increase in the spatial resolution was observed.

Table 2.1: Spatial resolution in mid-cell (in μm) of various VXD layers found from 1986 hadronic events. Values taken from [18].

Layer	1	2	3	4	5	6	7	8
Resolution	110	109	99	106	83	87	93	95

Noise: The main tool for noise studies were the events collected using the "random" trigger feature (see next section). These events contained normally only hits coming from synchrotron radiation or off-momentum particles, the probability of an interaction occurring at a randomly picked beam crossing being very low.

The number of hits found in the VXD in a random trigger event varied between the layers. Table 2.2 shows the average number of hits in each detector layer. It can be seen that the amount of noise depends on the chamber radius – layers farther away form the beam see less noise.

A careful study [18] revealed two different mechanisms creating noise in random trigger events. One of them is the synchrotron radiation. The detector was protected from direct radiation by two sets of moveable collimators located inside the beam pipe at about 4.5 m

Table 2.2: Average number of hits in the VXD layers in random trigger events.

Layer	1	2	3	4	5	6	7	8
$\langle n \rangle$	13.0	9.6	7.4	5.4	3.0	2.7	3.0	2.5

from the interaction point. The synchrotron photons could however pass through the opening in one collimator, backscatter on the back face of the other one and enter the detector. Soft photons entering the chamber can produce slow electrons via the Compton process or argon atom excitation. These electrons have very short range and give only local energy deposits. The synchrotron radiation hits should therefore be rather isolated and, on average, delayed (comparing to the track-induced hits) by the time needed for a return path to the other collimator. Hits with this characteristics have indeed been observed. A few percent of the random trigger events were however seen to have a different noise characteristics. In addition to the isolated hits they had also larger hit clusters, the TDC distribution of the cluster hits was peaked at very short times (close to T_0). The clusters were interpreted as due to off-momentum electrons which left their orbits and produced showers in the material of the beam pipe or detector elements. This source of noise was more dangerous than synchrotron radiation - due to the short time of arrival the hits from this source can easily mask those caused by tracks, and large clusters of hits (especially extended over few layers) can easily confuse the pattern-recognition. Fortunately larger clusters have been seen to occur only in less than 2% of the events.

Apart from the beam-associated noise one can expect also some interaction-associated noise in the hadronic interactions. This could come from soft photons created in the interaction or radiated by charged particles during traversing the detector materials and from δ electrons. They can also come from real tracks crossing the chamber at very low θ angles, and thus leaving only isolated hits in the innermost layers. This kind of noise can not be studied by random triggers - a crude estimate of this background was done by counting in the hadronic events the number of hits not used by the pattern recognition program. The number of non-associated hits in the hadronic events turned out to be higher than the number of hits seen in the random trigger events by about 1 hit per layer. This demonstrates that the track-induced background plays only a secondary role comparing to the beam-induced one.

2.4 Trigger and Data Acquisition

The time between the subsequent beam crossings at the PETRA interaction points was 3.8 μs in the two-bunch mode of operation. In most of those crossings no interaction producing particles in the detector occurred (except for the synchrotron radiation photons which accompanied each beam crossing). Interesting physics interactions occurred at a rate of maximum few hundred events per day. As the time needed to read all the detector channels was of the order of 40 ms, it is clear that the detector could not register all beam crossings, nor even all interactions (mostly originating from uninteresting beam-gas collisions) - the task of the triggering system was to decide within the time between crossings if an interesting interaction occurred. A positive decision caused the system to disable further detection and trigger actions and start reading out the detectors, otherwise a CLEAR signal was distributed to the readout modules causing the system to prepare for a new event. The timing for the trigger, as for the rest of the experiment, was derived from a beam pickup electrode located on the beam pipe about 7 m from the interaction point.

In normal runs about 15 various trigger sources were active, the final trigger decision was issued as a logical OR of their decisions. Out of those the most important for this analysis was the so-called multihadron trigger, supposed to select the annihilation events with hadron production. It required that at least 4 tracks were found in the central detector, where a track was defined as a PREPRO tracks with $p_\perp > 250\,\mathrm{MeV}/c$, with at least one of three closest ITOF counters hit and a track in one of three closest CPC sectors found by the CPC anode processor. The efficiency of this trigger for multihadron events which passed the offline selection criteria (see section 3.3) was very high - 98.7% of the events selected as multihadrons in the offline analysis had this trigger bit set.

Several other triggers use the track information from the chamber processors. Coplanarity trigger, used for Bhabha scattering and muon pair production studies required at least two tracks in the opposite sectors of the chambers. There was also a two-track trigger requiring at least two tracks in the central detector, including the vertex detector. The small length of the VXD allowed for efficient reduction of the number of beam-gas interactions seen by this trigger. Neutral energy triggers required some minimal energy deposits in the calorimeters and were used mainly to check the efficiencies of other triggers. A special $\gamma\gamma$ trigger which demanded a track in the central detector with an OK from the CPC cathode processor ($|z| < 30\,\mathrm{cm}$) in coincidence with a forward detector hit was also installed. A few more special triggers were used mainly for calibration and efficiency control - the most interesting of them used a strobe scaler to force the readout of every 3×10^7-th beam crossing. This so-called random trigger feature (random means here uncorrelated with activity in the detector) was found very useful for background studies.

After a positive trigger decision the experiment was read out by a four-branch CAMAC system under control of a 68000 front-end processor. The events were then transferred to a VAX 11/750 computer. There they were for a short time buffered in memory, so that statistics an monitoring tasks could have an access to them, then were given to a 370/E emulator to perform a preliminary reconstruction and finally were sent via the online link to the main DESY IBM computer to be written onto tape. The capability of the emulator and the link was about 5 events/second - for higher trigger rates (and for the case of IBM downtime) the VAX had also a local FIFO buffer located on disk. The disk capacity allowed to store events for about eight hours of non-stop running. The control of the experiment (downloading, performing the calibration runs, interaction with operator) was done by the VAX as well.

Chapter 3

Offline Analysis

The task of the detector and the data acquisition system is finished at the moment the data reach the storage tape. The selection, classification and interpretation of this data is the task of the offline analysis. This chapter describes the standard procedure of selection and reconstruction which was applied to the TASSO data before any physics analysis was done. The event classification in TASSO was based on the information about charged particles from the tracking detectors. The methods used for track reconstruction are therefore discussed first. Then the standard selection and reconstruction steps are explained. The last section describes the detector simulation.

3.1 The TASSO coordinate system

Before explaining the track finding procedure it is worthwhile to introduce the standard TASSO coordinate system and symbols used for various parameters. These will be used throughout the analysis without further explanations.

The coordinate system is defined by the large drift chamber. The origin lies in its centre, and its axis is used as z axis. The e^+ beam moves in the positive z direction. The y axis points vertically upwards, the third axis, x, is horizontal and points toward the centre of the PETRA ring. The cylindrical symmetry of the tracking detectors makes it convenient to work in the cylindrical coordinates r, ϕ, z. Therefore the plane perpendicular to the beam is usually referred to as $r - \phi$ plane.

Figure 3.1 illustrates the standard definition of the track parameters in the $r - \phi$ plane. The axial magnetic field causes the track to form a circle in the $r - \phi$ projection. Three parameters are needed to fully define a circle - TASSO has chosen:

1. R_0, the radius of curvature of the circle. In the TASSO convention it is always positive, the charge of the track is given by an additional parameter Q,
2. d_0, the distance of closest approach to the origin of the coordinate system,
3. ϕ_0, the angle between the line tangent to the track at a point of closest approach and the x axis.

By convention d_0 is positive if the origin of the coordinate system lies inside the circle (as in figure 3.1), negative otherwise.

For three-dimensional track reconstruction the so-called $s - z$ view is used. The s coordinate measures the track arc length in the $r - \phi$ plane from the point of closest approach.

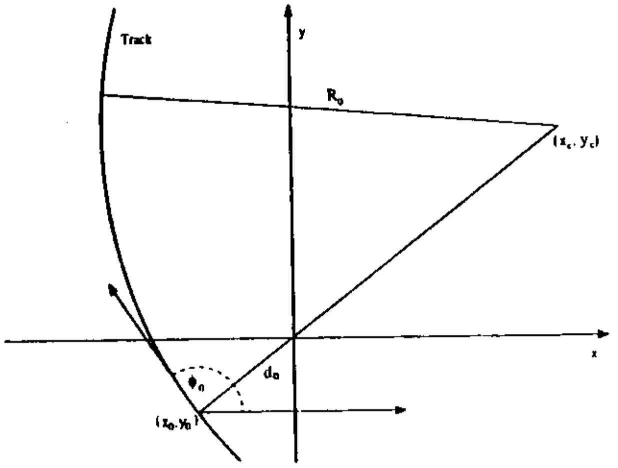

Figure 3.1: Illustration to the definition of track parameters.

In the $s - z$ projection tracks appear as straight lines, as the magnetic field is parallel to the z axis. Two parameters are therefore needed to describe the track - chosen were λ, the slope of the track in $s - z$ and z_0, the track z coordinate at $s = 0$ (so that the track may be parametrised as $z = z_0 + \lambda s$). Another variable often used is the angle θ between the track and the z axis. It is related to λ by $\lambda = \cot\theta$.

3.2 Track finding in TASSO Detector

The role of the track-finding program is to reconstruct trajectories of charged particles traversing the detector from hit coordinates in tracking chambers. The algorithm must resolve the left-right ambiguity associated with drift chamber hits, allow for noise (i.e. hits which do not belong to any tracks), and for finite chamber efficiency causing some hits to be missing. The kind of problem encountered by such a pattern-recognition program is illustrated by figure 3.2 which shows a typical hadronic event as seen by the TASSO inner detectors. Crosses mark the spatial positions of the Drift Chamber 0°, CPC and VXD hits (for the DC and VXD both the left and right hits are shown). One can see that in the regions of higher track density track finding is quite a difficult job, by eye it is even difficult to say how many tracks can be actually seen in the picture.

Three different algorithms were used by TASSO for the purpose of track finding. The analysis presented in this work depends crucially on tracking - therefore each algorithm will be now presented in some detail.

3.2.1 MILL

MILL [19] is a basic TASSO pattern-recognition program, used for finding tracks in the drift chamber and CPC. The track finding by MILL is done first in the $r - \phi$ plane, using only

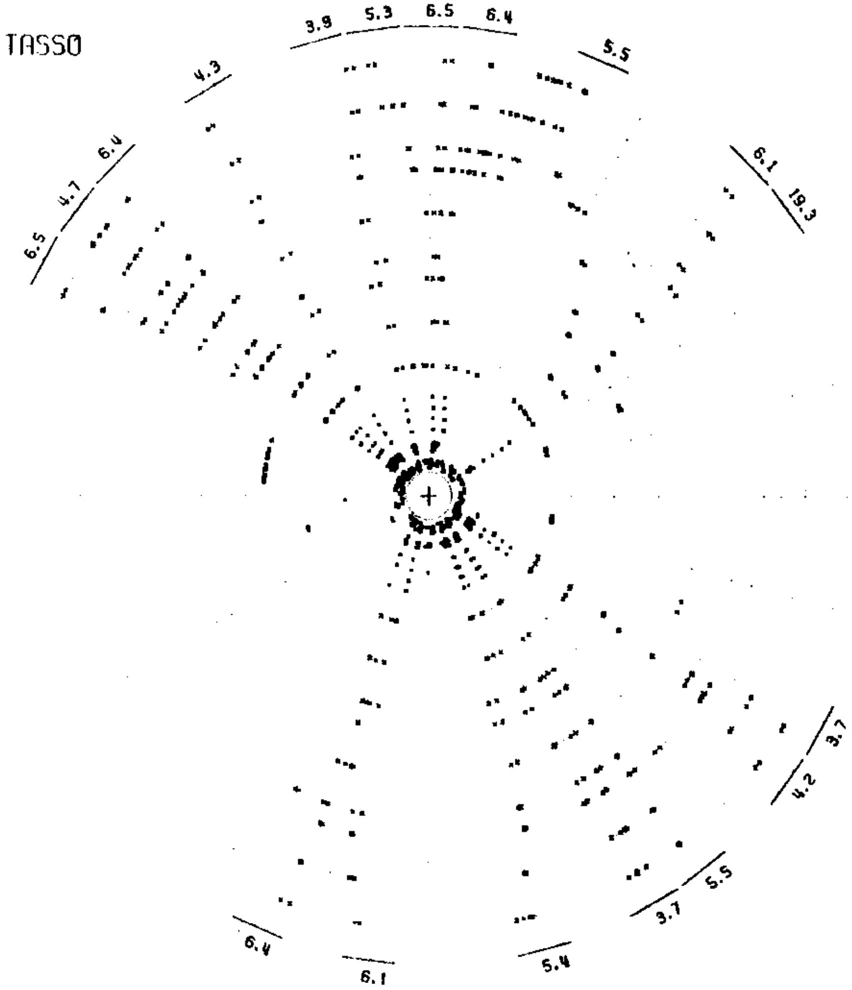

Figure 3.2: An $r-\phi$ view of the central detector showing hits caused by tracks in a typical hadronic event.

the information from the 0° DC layers. The basic structure MILL operates on is a link - an association between two hits in different layers. Lists of possible links are formed, where each link is assigned a curvature (by finding a circle passing through both its hits and the detector centre). A fast tree search algorithm is then applied to look for chains of links sharing hits and with similar curvature. The longest chains found are considered as track candidates. A road around each such candidate is then searched for hits (including the CPC anode wires) and a fit is attempted to various hit combinations. The procedure is repeated several times, starting with tight track acceptance cuts (low curvature, few missing hits, origin near the detector centre) and releasing them in each next step after the hits used already by other tracks have been deleted. This assures that good tracks are found first, and also shortens the time spent in the search, as searches through more lists of longer links (i.e. links skipping some planes) are performed after the number of available hits has been reduced. The method as described works well only for tracks which originate near the detector centre - other tracks are found at the end by making a combinatorial search through the remaining hits.

A similar algorithm is used to find tracks in the $s-z$ projection. First, for each $r-\phi$ track a list of hits on the stereo wires which could have been hit by the track is made. The position of each hit in z is calculated using known $r-\phi$ track parameters and the stereo angles of the wires. Then the links are formed and searched in the above described way - this time the search is simplified by the fact that the tracks are straight lines in the $s-z$ projection.

The first part of the MILL algorithm (tree search) was also called FOREST and used, with tight track acceptance criteria, as a separate program for quick filtering of raw data. FOREST is fast enough to be applied to the collected events before writing them to the tapes (it was actually run on a 370/E emulator connected to the online computer and could cope with incoming event rates up to about 5 Hz). MILL itself needs on average a few seconds on an IBM 3084 processor for a full reconstruction of a hadronic event.

3.2.2 PASS 5

The MILL algorithm does not make use of the precision vertex detector information. In order to make use of the vertex detector another pattern-recognition program is needed.

The PASS 5 program [20] takes the simple approach to the problem, in which VXD tracks are treated as extensions of the drift chamber tracks. The program picks the tracks found by MILL, extrapolates them to the vertex detector and defines a search road around the extrapolated track position. The width of this road depends on the uncertainty of the MILL track parameters and the estimated amount of multiple scattering between the detectors. Combinatorial search is then performed on the VXD hits found inside the road. Tracks are fitted to the VXD only, and only d_0 and ϕ_0 are free parameters - the radius of curvature is kept at the value found by MILL. Only tracks with at least four VXD hits assigned are considered. No three dimensional reconstruction is attempted, as the vertex detector does not provide any z information.

The PASS 5 is a reasonably fast algorithm, it takes a few seconds per hadronic event. Its efficiency is also good, especially for isolated tracks (in the back-to-back two-prong events it is very close to 100%). In dense jets the efficiency drops somewhat, as it often happens that the tracks which are searched for first steal hits from the others, leaving too few hits for a remaining track to be acceptable. Still, nearly 90% of clean high-momentum and low-d_0 MILL tracks in the hadronic events get a corresponding PASS 5 track.

3.2.3 FELIX

The other program used in TASSO for pattern recognition in the track chambers including the vertex detector is called FELIX [21]. The reasons behind introducing and using another track finding program were some disadvantages of PASS 5. First, PASS 5 fits tracks to the vertex detector hits only - the drift chamber information is used in the final fit only to get the track R_0. It would be certainly advantageous to fit a track simultaneously to all the available hit coordinates. Second, PASS 5 does not make a real track finding - even a clean vertex detector track will not be found if the corresponding drift chamber track was lost (due to chamber inefficiency, falling outside the chamber acceptance or secondary interaction). A program which could use all the information available for track finding should therefore be more efficient. Finally, in certain situations it was desirable to find the tracks in the vertex detector only, without information from other chambers (e.g. in cosmic runs with the drift chamber switched off).

FELIX is a program which does the full track finding simultaneously in all the tracking detectors. It is flexible enough to allow the user to specify the set of chamber layers which should be used.

The FELIX algorithm uses the backtrack search technique [22]. The tree search of MILL is not well suited for pattern recognition in non-homogenous detectors, and finds efficiently only tracks originating close to the detector centre. The idea of the backtrack method is to grow a track hit by hit, proceeding from the outmost layers inwards. Having a partial track, the algorithm tries to add a hit from the next chamber layer. Each time a hit is added, the track parameters are reevaluated to check if the combination forms an acceptable track. If yes, the algorithm proceeds to next layer, if not the next hit is attempted. After all the possible hits have been tried the program goes back to check the next hit in the previous layer. The algorithm proceeds, until no more hits can be added. The track is then accepted it it has a minimum number of hits assigned to. Similar to MILL, FELIX makes several search passes, each time releasing the criteria which define an acceptable track. Also the track finding in $s - z$ projection is done in a similar way as by MILL - FELIX runs the backtrack search on the $s - z$ hit positions reconstructed using the $r - \phi$ track parameters.

As it performs the track search in all the tracking chambers, FELIX is potentially the most efficient track finding program. This has to be paid for in the execution speed - FELIX needs about 30 seconds of IBM 3084 CPU time per hadronic event, most of this time is spent in fitting to partial track vectors.

Some comparisons of the results given by PASS 5 and FELIX were done [23,24]. It is concluded that FELIX was indeed more efficient for tracks with small angles to the detector axis. In case of good tracks with many hits both programs gave very similar results. Also, the efficiency for finding a VXD track associated with a good DC track is similar for both programs. FELIX was seen to give a better impact parameter resolution (measured from width of the d_0^{beam} distribution) - this was probably due to using the drift chamber hits in the fit. The author of [23] recommended usage of FELIX for studies involving the precision vertex fits, as slightly better than MILL-PASS 5, and this recommendation was followed in this analysis.

3.2.4 Track Refitting

Track parameters given by the pattern-recognition programs are normally obtained from a fit to the coordinates of the associated hits. However the actual fitting procedures used by trackfinders are usually optimized for speed, rather than for precision. The reason is obvious - pattern-recognition programs spend most of their time in performing fits to various hit combinations, and the most efficient way to speed up the program is to optimize its fitting routine. For these reasons it was found advantageous for studies requiring high tracking precision to perform an additional refit of the tracks, using an algorithm optimized for high accuracy rather than speed. Another reason for doing the refit is that at this stage one may make certain small corrections to the hit coordinates - for example apply non-linear corrections in the space-drifttime relation (which are often not known when the track finding is made) or correct the timing for the particle flight time and the signal propagation on wire (this is not possible before the three-dimensional reconstruction has been done).

A program package which can refit the tracks has been written by D. Saxon [25]. The package was extensively used in the analysis - it is therefore worthwhile to briefly describe the algorithm used.

The program is able to cope with tracks found by any of the TASSO trackfinder programs. Its first step is to get all the hits which the pattern-recognition program assigned to the track and (optionally) to correct their positions for the small effects described above. The program can be set up to refit either in the $r - \phi$ projection only, or simultaneously in three dimensions. The track circle in the $r - \phi$ plane is parametrised by three variables. K, b_0 and ϕ_0, which relate to the standard TASSO track parameters by

$$K = \frac{-Q}{R_0 - d_0}, \qquad b_0 = d_0 Q$$

The distance of a point (x, y) from a track can be approximately expressed as

$$d(x,y) = \frac{K}{2}(x^2 + y^2 - b_0^2) + x \sin\phi_0 - y \cos\phi_0 + b_0$$

This expression is exact for $K = 0$ and for points laying on the circle. For points close to the circle (hits assigned to a track) the approximation is usually good to better than 0.1%. An advantage of using this parametrisation is that for very high momentum tracks $K \to 0$, so no discontinuities appear and no precision loss occurs. Also, all the partial derivatives of d are easily calculable. If used to fit to the VXD and DC simultaneously, the program can optionally consider track deflection by multiple scattering in the detector material, approximating it to occur at a single layer in the middle of the CPC. This is done by adding to the above calculated hit distance a correction in the form $\vartheta \cdot (r - a)$ if $r > a$, a is the radius of the scattering layer. ϑ denotes here the track deflection angle in the $r - \phi$ plane and is a free parameter of the fit. The addition of this simple scattering model was seen to significantly improve the tracking resolution for tracks refitted simultaneously in the DC and VXD.

The three-dimensional refit requires also to calculate the distance from the stereo layer hit to the track. This depends on the above variables, as well as on the $s - z$ track parameters λ and z_0. The simultaneous six parameter fit is thus performed in this case. The formulae used are given in [25], for this work this feature is less important, as only two-dimensional fitting was used.

Using the above given formula one can calculate the distances of all the associated hits from the track fitted, and from them the χ^2 of the track

$$\chi^2 = \sum_{hits} \frac{d_i^2}{\sigma_i^2} + \frac{\vartheta^2}{\vartheta_0^2}$$

Here d_i denotes the hit distance in the i-th layer of the detector and σ_i is the spatial resolution of this layer. ϑ_0 is the R.M.S. scattering angle and is calculated from the track momentum and the amount of material traversed. The fitting routine tries to find the track vector $\mathbf{v} = (K, b_0, \phi_0, \vartheta)$ which minimises the above χ^2. This is done by solving the equations

$$\frac{d\chi^2}{dv_\alpha} = 0$$

The solution is found iteratively using the Newton method. The program contains safeguards against oscillatory behaviour and non-convergent fits. For clean tracks the fit converges usually after 3 to 5 iterations. The program returns then the track parameter vector found and the error matrix.

An additional feature of the program allows for an attempt to improve the fit quality by excluding from fitting those hits which give the highest contributions to χ^2. This is done only for the fits with high χ^2 (normally if χ^2/D.F. > 2). The program just masks out the hits with highest contribution to χ^2 in turn, and tries to fit to the remaining ones. The fit with lowest χ^2 is kept, the offending hit is permanently masked out and the procedure is – if needed – repeated. The maximum number of rejections allowed is controlled by the user – but the number of hits remaining can not fall below certain minimum (if the multiple scattering option is in use the program may switch it off if the number of remaining VXD hits falls below three).

To check the effectiveness of this hit rejection procedure a Monte-Carlo simulation was used. In the simulated data is was possible to trace the origin of each hit in the chamber, i.e. to tell if the hit came from noise, mirror image or a track, and get the identification of the parent track. The first hit rejected by the program was in more than 50% of the cases not caused by the track under consideration (i.e. was stolen from another track or caused by noise). The second and third hits rejected were wrong in 40% resp. 35% of the cases. On average FELIX tracks were seen to have 0.95 misassigned hits per track – this improved to 0.8 misassigned hits/track if the rejection of two points was allowed for. After these studies it was concluded that the hit rejection was an useful feature, helping to avoid some tracking mistakes (i.e. tracks with fitted parameters off from the true values by significantly more than their statistical errors). The hit rejection has however also its disadvantage – it biases the distribution of the resulting χ^2, invalidating its statistical meaning.

3.3 Data Reduction

During the 1986 running TASSO recorded a total of about 4×10^7 triggers. The integrated luminosity collected was about 110 pb^{-1}. The cross section for a reaction $e^+e^- \rightarrow f\bar{f}$ at $\sqrt{s} = 35$ GeV is on the other hand of the order of 80 pb per fermion, so one can expect to have $O(10^4)$ annihilation events per fermion type in the collected data. The role of the offline data reduction process is to remove background events (caused by noise, cosmic rays, beam-gas interactions...) without losing the physics events, and to classify the remaining ones according to the underlying physics processes.

The basis of the event classification in TASSO were the results of track finding. The first step was to apply a fast FOREST algorithm to all the events. As already mentioned, this phase was usually done on the 370/E emulator before sending the events to a tape. Those events which had more than a minimum number of tracks (two back-to-back or three in any configuration) seen by FOREST were given to MILL for full trackfinding. All the events, irrespective of the FOREST or MILL results, were then written to the so-called PASS1 tapes, which were kept as the basic archive media.

The analysis then proceeded in three further steps, at each step some selection was applied and some reconstruction done. The rejection criteria at each step were based mainly on the number of acceptable tracks, where an acceptable track had to have the following properties:

1. three dimensional reconstruction,
2. $|d_0| < 5$ cm,
3. $p_\perp > 0.1$ GeV/c, $p_\perp$ denotes the momentum component perpendicular to the z axis,
4. the χ^2 of the two dimensional fit, $\chi^2_{r-\phi} < 10$,
5. reach at least 6-th 0° layer of the Drift Chamber (this effectively excluded tracks with $|\cos\theta| < 0.87$,
6. the χ^2 of the $s - z$ fit $\chi^2_{s-z} < 20$,
7. $|z_0 - z_v| < 20$ cm, z_v denotes the z coordinate of the event vertex, found by averaging the z_0's of all the tracks passing cuts 1.–6.

The above cuts are in fact very loose and meant to remove only very poor quality tracks and obvious trackfinder errors.

The most important part of the event selection procedure for this work was the last step, which was supposed to select the annihilation events with hadrons produced in the final state. The events selected by this step were written to the so-called PASS4 tapes.

In order to reach the PASS4 tape an event had to fulfil the following criteria:

1. have at least 5 acceptable tracks,
2. the sum of momenta of the acceptable tracks, $\sum |p_i|$ must exceed $0.53 \cdot E_{BEAM}$, E_{BEAM} is the beam energy,
3. the z coordinate of the event vertex z_v must lie within 6 cm from the origin,
4. if the event has a $3-3$ topology, i.e. if it has exactly three tracks in each hemisphere, the invariant mass of at least one of this triplets must exceed the τ lepton mass (if pion masses are assumed for the tracks).

Events passing these cuts were then scanned visually in order to remove wide angle Bhabha scattering events with one or both electrons creating showers in the detector material and obviously faked events, caused by the excessive noise or with clear pattern-recognition errors. This scan removed typically about 1.5% of the selected events.

31176 events from 1986 running passed all the above tests and got onto the final PASS4 tapes. It was estimated [26] that the events on PASS4 tapes contain still 1.2±1.2% background from τ pair production and 1.6 ± 0.8% $\gamma\gamma$ events (events of the type $e^+e^- \rightarrow e^+e^- q\bar{q}$). Other sources of background were estimated to give a negligible contribution.

The next step was then to run PASS 5 and FELIX trackfinders on the data. This was done only at this point to limit the computer time consumption. The tapes created in this step, called PASS 5 tapes were used as input for the analysis described in this work.

3.4 Beam Spot Reconstruction

One step of the analysis, which was normally performed between recording the event and creation of the PASS4 tape, was of particular importance for the following analysis - therefore it will be now described in more detail. This was the reconstruction of the beam spot location.

Beam spot finding was performed on a run-by-run basis, where one run corresponded normally to one PETRA fill. Sometimes in short runs there were not enough data collected to make the beam spot finding in this case several successive runs were merged. Short runs were usually a consequence of some technical problems with either the detector or the PETRA ring.

The procedure itself started from the reconstructed events taken from the so-called PASS3 tapes (before the hadronic selection). Candidate events for use in the beam spot finding were selected by requiring them to have at least two MILL tracks with three-dimensional reconstruction, $|z_0| < 15\,\mathrm{cm}$ and with all tracks intersections well inside the beam pipe (to remove events coming from interaction of the off-momentum particles with the beam pipe itself). The selected events were then passed through the PASS5 reconstruction to include the vertex detector information. Those PASS5 tracks with $|d_0| < 1\,\mathrm{cm}$, $p_\perp > 0.2\,\mathrm{GeV}/c$ and $\chi^2 < 3$ were then used for the beam spot determination. It was required that at least 50 such tracks were found in a given run.

The reconstruction itself was done by considering the points of closest approach of the tracks to the centre of the interaction region (x_b, y_b). This distance is a sum of two contributions: the displacement of the event vertex form the centre of the beam spot, and the displacement of the track from the event vertex. One can thus define the χ^2 contribution of the track considered as

$$\chi_t^2 = \frac{(x_i - x_b)^2}{\sigma_x^2} + \frac{(y_i - y_b)^2}{\sigma_y^2} + \frac{d_t^2}{\sigma_t^2}$$

(x_i, y_i) denote the (unknown) coordinates of the event vertex, σ_x, σ_y are the sizes of the interaction region and σ_t is the tracking error of the track. Putting in the values for σ_x and σ_y known from the machine optics, and an estimation for σ_t:

$$\sigma_t^2 = \sigma_0^2 + a/p^2$$

with $\sigma_0 = 250\,\mu\mathrm{m}$ and $a = 200\,\mu\mathrm{m}/(\mathrm{GeV}/c)^2$ one can find x_i and y_i for each track by minimising χ_t^2. Substituting these values back into χ_t^2 and summing over all the tracks gives the total χ^2 which is now a function of (x_b, y_b) only. Minimising this χ^2 with respect to these variables one can find the estimation of the location of the centre of the beam spot. This minimisation was iteratively repeated, rejecting after each step those tracks which had $\chi_t^2 > 25$ (these were probably not coming from the interaction point). The typical errors on the beam spot position returned by this procedure were between 30 and 50 μm. The final χ^2 per degree of freedom was also stored, and could be later used to reject the runs with poorly determined beam spot.

The results of the beam spot finding in 1986 data are shown in figure 3.3, separately for the x and y coordinates, as a function of the run number. Note different vertical scales on both plots. It can be seen that the beam position in y was generally stable over longer run periods, changing significantly only a few times during the entire period. On the other hand the x position was rather unstable, undergoing sizeable changes from run to run. This was probably a result of frequent optimisations of the beam orbits performed in order to reduce background at the experimental regions.

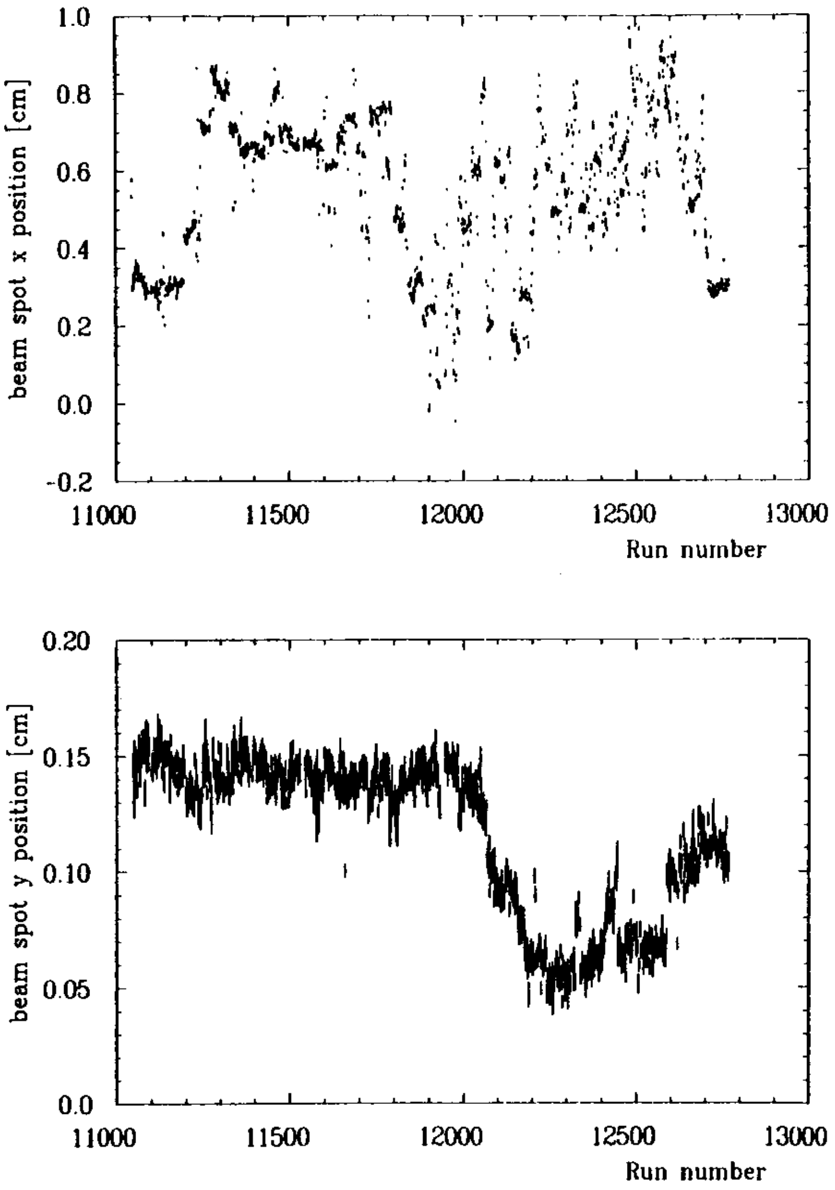

Figure 3.3: Beam spot positions in 1986 data as a function of the run number.

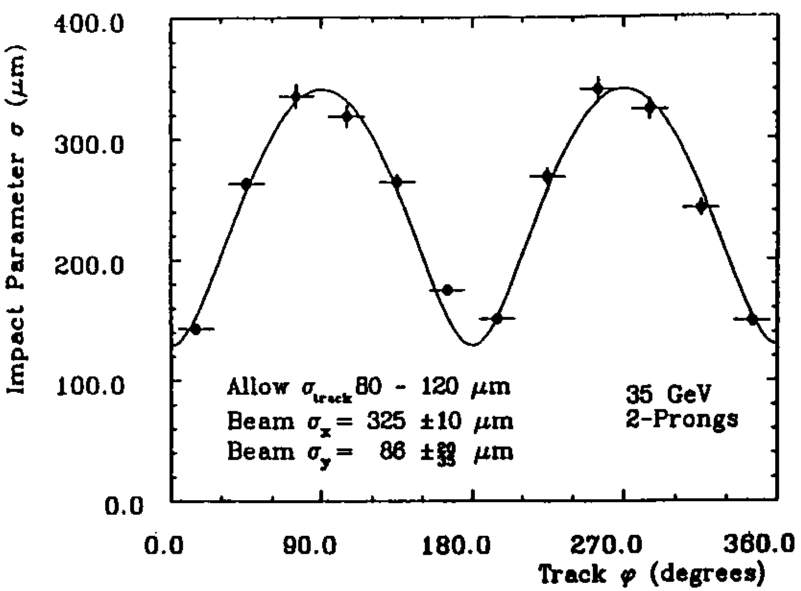

Figure 3.4: The track impact parameter resolution shown as a function of the track azimuth. The line shows the fit results.

In [23] an interesting method for the determination of the size of the interaction region was proposed. It envisaged plotting the RMS width of the track impact parameter distribution as a function of the track ϕ_0. This is expected to follow the relation

$$\sigma_d^2 = \sigma_t^2 + \sigma_x^2 \sin^2\phi_0 + \sigma_y^2 \cos^2\phi_0$$

A fit to the plot allows to unfold the interaction point position errors σ_x and σ_y. The result is shown in figure 3.4, the impact parameter resolution plotted was calculated from clean two-prong events. The x size of the interaction region obtained from the plot agrees well with the expectation from the machine parameters, the y size is consistent with the estimated error of the beam center determination.

3.5 Simulated Data

For an estimation of the effects introduced by the detector response and event acceptance criteria a Monte-Carlo simulation was used. The task of Monte-Carlo simulation consists normally of two steps: the first step generates the particles created in the interaction, the second simulates the detector response to these particles.

3.5.1 Simulation of the Hadron Production Process

This part of the simulation program has the task of modelling the production of particles in e^+e^- annihilation, using some theoretically motivated approximations to describe the production process. The task is usually broken into three parts: first one generates the initial parton configuration using the theoretical input given by the Standard Model (mainly by the QCD) - this is called the vertex part. In the second step the partons are generating the physical particles - this process is called fragmentation, and is a domain of phenomenological models. Finally the short-living particles or resonances created in the previous step are decayed, usually using experimental information about the decay modes and branching fractions, but also some phenomenological models where the experimental information is missing.

Three different physics simulation programs were used, and are described below.

1. QCDFF [27]. The vertex part of this program generated initial parton configurations using the $O(\alpha^2)$ QCD matrix elements calculated in the extended FKSS scheme [28,29], α_s was set to 0.155. The fragmentation model used the independent jet fragmentation idea of Field and Feynmann [30]. The relative probabilities used for different quark production in the fragmentation chain were $u : d : s = 1 : 1 : 0.4$. The average p_T given to the created particle was 350 GeV/c, the probability of baryon production was set to 0.1 (however no c or b baryons were produced). The fraction of pseudoscalars among the mesons produced in the fragmentation was 0.42, same was the fraction of octet states among all baryons. No tensor mesons or higher states were produced. The fragmentation function of the heavy quarks was the one of Peterson *et al.* [9] with $\epsilon_b = 0.01$ and $\epsilon_c = 0.075$. All the parameters were chosen to give the best agreement of the simulation results with the TASSO data [29]. In the decay part particular care has been put into simulation of the B meson decays. As very little is known about the exclusive decay channels of the B meson, a model was used [31]. It assumed the spectator decay with 100% $b \to c$ transition. The c and spectator quarks were forced to form a single meson, the virtual W was decayed according to phase space, (or just created a lepton-neutrino pair). The parameters were carefully tuned to match the available data on the B meson decays from CLEO.
2. LUND program with second order QCD effects [32]. Version 6.3 of the LUND simulation program was used. The program generated the initial partons according to $O(\alpha_s^2)$ QCD cross section [33]. These partons were then fragmented according to the LUND string fragmentation model [34]. The LUND symmetric fragmentation function was used for all the flavours, with the parameters $a = 0.96$ and $b = 0.70\,\text{GeV}^{-2}$. The other parameters set were $\Lambda_{QCD} = 0.520\,\text{GeV}$ and the width of the primary hadron transverse momentum distributions $\sigma = 0.42\,\text{GeV}/c$. All the remaining program parameters were kept at the values recommended by the authors of the program [32]. These parameters gave the best agreement of the simulation results with the data [35].
3. LUND program with a coherent parton shower option. This program used the same fragmentation and decay model as the previous one, apart from a different setting of some parameters ($a = 0.44$, $b = 0.7\,\text{GeV}^{-2}$, $\sigma = 0.36\,\text{GeV}/c$ and other changes recommended by the authors). The vertex part was however generated using the leading logarithm coherent parton shower approach. This model incorporates in principle also the higher order QCD effects, although included only in an approximate way. The Λ_{QCD} value used in the shower evolution was to 0.38 GeV. Also here the parameters have been tuned to obtain the best agreement with the data [36].

All the programs described above incorporated the QED radiative corrections to the order α^3 as calculated by Berends and Kleiss [37]. Also the lowest order electroweak effects were taken into account in the relative cross sections, and in the LUND model also the forward-backward charge asymmetry was simulated. The three data sets produced by the above described programs will be further referred to as "QCDFF", "LUND62" and "LUND63" respectively.

3.5.2 Simulation of the Detector Response

All the particles generated in the previous step were then passed through the detector simulation routines. The SIMPLE program of S. Lloyd was used for this purpose. The event vertex position was generated from the (input) beam spot position smeared with the size of the interaction region. The program contained a full description of all the active components and materials of the TASSO inner detector. The particles generated in the previous step were tracked through the magnetic field. The positions of the intersections between the tracks and sensitive layers of the detector were found, and hits were generated by smearing these positions with the chamber resolutions. The finite chamber efficiencies and known dead areas were taken into account. Secondary interactions were simulated when the tracks traversed the detector materials – these included energy loss and multiple scattering of the charged particles, secondary hadronic interactions, bremsstrahlung from electrons and pair creation by photons. Also decays of the long-lived particles (π, K, hyperons) were under responsibility of the detector simulation program. A parametrisation of the TASSO track triggers efficiency was used to evaluate if the simulated event would fire the detector.

Particular care was taken in simulation of the vertex detector. The resolution was calculated from the data for each layer individually, and was varied across the cell in the way seen in the data. Noise hits were included by overlaying on the simulated hits a hit pattern found in the real events taken with a random trigger.

The output of the SIMPLE program were hit banks in the same format as in the data and the event history information, which allowed to trace the entire fragmentation history starting from the primary partons up to the origin of every hit in the chambers. The normal data reduction procedure was then run on the simulated data, including MILL, data reduction procedure and FELIX track finding. Each of the simulated data sets had about 70,000 events remaining after the selection.

Chapter 4

The B Tagging Method

4.1 Introduction

An e^+e^- ring provides an ideal tool to study physics of the b quark. At energies well above the $b\bar{b}$ threshold b production contributes 1/11 to the total hadronic cross section, and even more at energies corresponding to the Υ resonances. Contrary to the hadron collisions the events are clean, free from fragments of colliding particles. Most information about b physics comes thus from experiments operating at e^+e^- storage rings.

In order to study the b physics one needs however some way to select the $b\bar{b}$ production events from the background of all annihilation processes with hadron production. The direct way would be to reconstruct the decaying B particle, thus unambiguously tagging the event as $b\bar{b}$ production event. Such a method has been widely used for studying charm physics by reconstructing the decay $D^{*+} \rightarrow D^0\pi^+$ [38,39,40,41]. The low Q value of this decay and sizeable branching ratios of D^0 decays into easy to reconstruct few body final states, make it possible to obtain relatively pure samples of D^* production events. In the B case nature does not offer us such a nice system as D^*/D^0. The lowest energy B states decay with high multiplicity, rendering the task of full reconstruction virtually hopeless.

Up till now the full B meson reconstruction has been possible only at the e^+e^- machines running at the $\Upsilon(4S)$ resonance [3,4,5]. As mentioned in chapter 1, the $\Upsilon(4S)$ resonance decays predominantly into a pair of B mesons. Due to the low Q value of this decay, both B mesons are produced nearly at rest. This facilitates greatly the reconstruction, as one can constrain the energy of the B candidate to agree with the beam energy to significantly reduce the background. This trick does not work in the PEP and PETRA energy range. Also, at higher energies there are generally more particles produced in addition to the two B hadrons, and the particle identification is much more difficult for the high momentum decay products. Because of this no B hadrons have been successfully reconstructed at high energy e^+e^- collisions. We are thus forced to go for less direct selection techniques in search for the $b\bar{b}$ events. The selection methods which have been used up till now for this purpose can be broadly divided into two classes: the 'high p_T lepton tag' and the 'event shape method'.

The 'high p_T lepton' method exploits the semileptonic decays of the B hadrons. The 'prompt' leptons (i.e. those leptons not coming from processes like pion decays or γ conversions) are relatively easy to identify experimentally. The only source of such leptons in annihilation events are decays of heavy quarks (c or b). To distinguish between the two one takes advantage of the much higher mass of the B hadrons compared to the charmed ones. Those leptons with momentum relative to the decaying particle falling outside the kinematical limit for the charm decay point unambiguously to the B decay. Experimentally the momentum of the decaying object is not known, but its direction of flight can be approximately reconstructed. Thus these leptons with big momentum component perpendicular to this direction are used to signal the B hadron production and decay. This technique has been widely applied by the PEP and PETRA experiments, yielding samples of up to a few hundred events with $b\bar{b}$ content of 60 to 80% [10,42,43,44]. The efficiency of lepton tagging is limited by the b semileptonic branching ratio.

The 'event shape method' is based on a difference in event topology between the $b\bar{b}$ events and lighter quark ones. In the latter case all the particles produced come either from fragmentation of primary partons, or decays of light particles and resonances. Both sources tend to produce particles collimated along the directions of the primary partons. The topology of a $b\bar{b}$ event is dominated by high multiplicity decays of two heavy objects (the B hadrons) producing particles in much wider range of momentum space. One thus expects that a jet produced by a primary b quark should on average have higher multiplicity and be more spherical than a lighter quark one. This expectation has been confirmed experimentally [10]. In practice it is however quite difficult to utilise this difference for b enrichment. The reason is the existence of multi-jet final states, which can simulate the b jet characteristics also in lighter quark jets. Event shape methods are thus limited to produce samples with relatively low purity. Additional disadvantage is that the purity of the resulting samples can be derived only from a Monte-Carlo simulation, and results are strongly dependent on the details of the model used.

An example of application of the event shape separation is the boosted sphericity product method used by TASSO [45]. In this method two jets were constructed by collecting together the tracks within 41° from the sphericity axis on both sides of the event. The tracks in either jet were then Lorentz boosted in the jet direction to bring the jets towards the B hadron rest frame. The sphericities of the resulting systems were calculated separately and multiplied together. Events with high sphericity product were then selected – it was estimated that about 32% of them were $b\bar{b}$ production events The tagging efficiency (defined as the probability that a $b\bar{b}$ event accepted by the detector will get a tag) was about 35%. Another variable proposed for this purpose was the jet transverse mass $M = 2\frac{E_{beam}}{E_{vis}}\sum|p_T^{out}|$ used by JADE [46] in addition to the muon p_T for b separation.

In this work it has been decided to use the relatively long lifetime of B hadrons combined with their high decay multiplicities to tag the $b\bar{b}$ production. The idea of using the secondary decay vertex as a tag of heavy flavour production is not new, see e.g. [47] for an extensive study of its features and comparison with other methods. It is not easy however to apply this idea in practice. Assuming the average B hadron lifetime of about 1.3 ps one can estimate the average B flight path before decay to be of the order of 1 mm for hadrons produced at 35 GeV e^+e^- CM energy. On the other hand a detector at a storage ring can not be brought arbitrarily close to the interaction point, the minimal distance at which the first measurement can be obtained is of the order of 10 cm. This means that neither the B track, nor the decay point can be directly seen by the detector. One must instead infer the decay vertex by extrapolating tracks seen in the detector towards the interaction point. Very good tracking resolution is required. Also, the amount of material in front of the detector must be minimised in order to avoid smearing of tracks by multiple scattering. For these reasons up till now the idea of tagging the b by the secondary vertex reconstruction has not been applied to the existing data (TASSO has worked out a method to tag B hadrons by lifetime without actual reconstruction of the decay vertex, details can be found in [18]).

This chapter describes in detail the method of tagging the b by vertex reconstruction and its application to the data collected by the TASSO detector. Section 4.2 explains the idea and presents the overview of the procedure used. Event and track selection criteria are described in section 4.3. Section 4.4 describes the procedure of finding the interaction point. The vertex reconstruction is described in section 4.5. Finally section 4.6 deals with the problems of determination of the purity of resulting samples and of the systematic effects.

4.2 The Idea of the Method

The basic idea of the method is presented in figure 4.1. Figs. 4.1 a,b,c picture the charged track pattern around the interaction point in a typical light quark, charm and bottom jets respectively. In the light quark case all tracks come from either the primary parton fragmentation or the decays of resonances. Both these processes occur at the strong interaction scale, the size of the production region is thus of the order of fermi. As a result all the tracks appear to emanate from a common point – the production point. The only process which could create tracks out of this production point are weak decays of strange hadrons. These however occur usually at the scale of centimetres and the multiplicity of their products is relatively low - both these features make it easier to tag those decays.

Charm jets present a more complicated structure in the vertex region. In addition to the production point with its fragmentation tracks a second track source appears – the decay point of a charmed hadron created in the fragmentation process. For charm jets produced at 35 GeV this secondary vertex lies on average about 1.3 mm away from the production point, the numbers of charged tracks coming from both sources are similar.

The bottom jet presents the richest structure in the vertex region. One sees again a few primary fragmentation tracks, then the decay point of the B hadron, and at the end the decay point of the charmed hadron usually created in the B decay. Typical distances between vertices in a jet from a 35 GeV e^+e^- annihilation are of the order of 1 mm. Due to high mass and hard fragmentation of the b quark, the energy left for other fragmentation products is low – the number of tracks coming from the production point is thus expected to be lower than in the lighter quark case. This effect together with the high multiplicity of the B decay make the majority of tracks in the b jet appear not to come from the production point. This fact is exploited in this work for tagging the b production.

The problem posed by this rich structure is illustrated in figure 4.2. As mentioned above, in the real life one does not see the decay points directly, the only information obtained from the detector are track parameters far from the interaction point, which must be extrapolated toward the IP in order to find the origin of tracks. Figure 4.2a shows the same jet as 4.1c, with all the tracks extended beyond their origins towards the production point. The clean vertex structure of fig. 4.1c gets much obscured. Furthermore, in the real experiment tracks are measured with finite precision. Fig. 4.2b shows the same jet again, after smearing the tracks with a typical detector resolution. The original vertices disappeared completely in the jumble of intersecting tracks.

There are two conclusions from the above considerations. First, one should never force all tracks in the jet to share a common vertex (unless the track resolution is much worse than the distance between vertices). This would not be correct, as the b and c jets simply do have more than one vertex. Secondly, it is very hard to locate all jet vertices and to make unique assignment of tracks to them. This is true even if the track resolution is very good

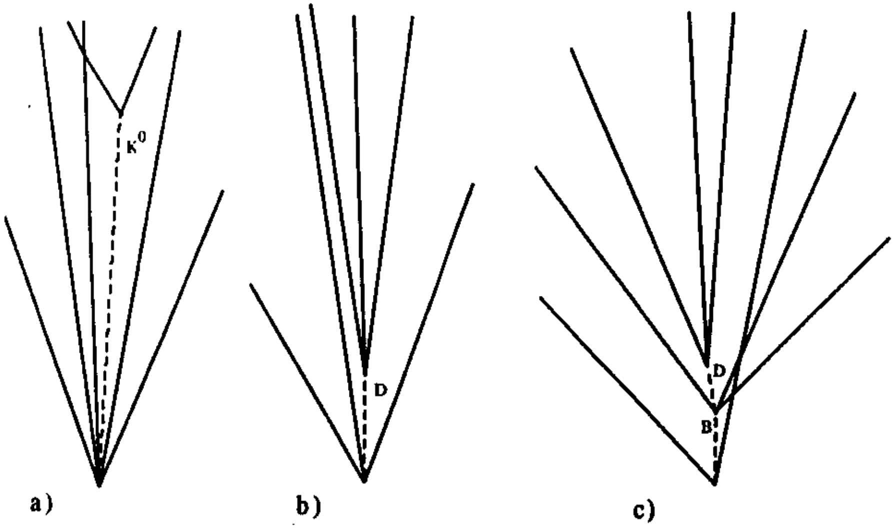

Figure 4.1: Typical jet vertex structures of jets from different primary quark types: a) *u*, *d* or *s* jet; b) *c* jet; c) *b* jet.

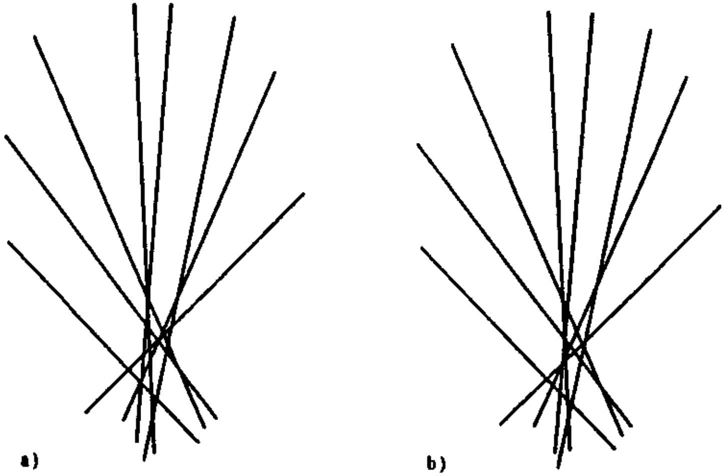

Figure 4.2: The vertex structure of the *b* jet from fig. 4.1c as seen in the experiment: a) The tracks have been extended beyond their origin. b) The tracks have been in addition smeared by measurement errors.

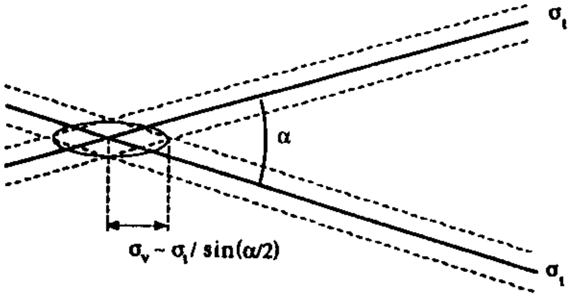

Figure 4.3: Dependence of the intersection reconstruction error on the track opening angle.

(fig. 4.2a). It seems therefore that the optimum strategy would be to try to find a point which is consistent with being an origin of the majority of tracks. In case of a light quark jet this would normally be the production point, for a *c* jet this should locate the production point or the decay point with similar probability, for a *b* jet the common origin should usually lie away from the production point towards the decay vertices.

One more problem remaining is how to get rid of correctly found decay vertices in charm jets. Even if the probability of reconstructing the secondary vertex in a charm jet is smaller than in a *b* jet, there are four times more charm jets in the data than bottom jets. Thus *c* might constitute a serious background to the *b* jets tagged. The way out of this problem proposed here uses the fact that the decay products of a charmed hadron have on average much smaller opening angle than the decay products of a bottom hadron (due to much smaller mass of charm). This results in poorer determination of the vertex position along the flight direction of the decaying particle in the case of charm jets (see fig. 4.3). It is therefore proposed not to use the decay distance as a measure of vertex separation, but to combine it with the estimated error on this distance. Only those vertices which are far away from the production point *as compared with their position determination errors* should be used as *b* tags. This requires that the statistical error of the vertex position is computed for each vertex.

The following procedure for *b* tagging was proposed (see fig. 4.4). First, clean annihilation events should be selected. As the jet vertices are to be compared against the production point, it is necessary that the beam spot is well reconstructed. The tracks found in these events should be then assigned to jets. One has to be careful on this stage to remove from consideration any tracks which are suspect of being poorly reconstructed, or which could have been substantially affected by multiple scattering. The two jets, defined as two lists of tracks, are then to be passed to the vertex finder. This part of the program picks various combinations of tracks belonging to a jet and tries in turn to force them to intersect at a common point. The vertex candidates obtained in this way are then compared with each other, in attempt to find the best one (the comparison criteria are: number of participating tracks, their quality and how well they fit to the common intersection point). The candidate which wins the competition is then called the 'jet vertex' and its coordinates and the error matrix are given to the 'Calculate separation' process.

Meanwhile the production point is found. Starting point is the beam spot location determined on a run-by-run basis. An attempt is made to locate the production point more precisely inside the beam contour by using all good tracks in the event. The reasons for doing

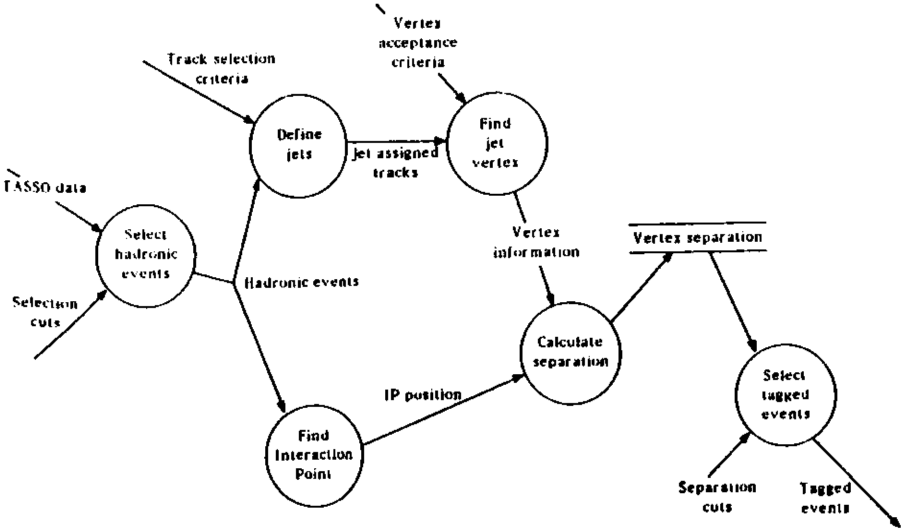

Figure 4.4: Data flow diagram of the tagging procedure.

it, together with some justification for the procedure used can be found in section 4.4.

The production point and jet vertices are then compared against each other. The results of this comparison, referred as separation data, are computed and stored. By imposing various cuts one can now define b tagged samples of different purities.

The rest of this chapter describes in detail application of the above procedure to the TASSO data.

4.3 Event and Track Selection

The analysis started from the event sample selected by the standard TASSO hadronic cuts (as described in section 3.3). It has been decided to use only the data collected during the 1986 running at 35 GeV CM energy. The data taken during the high-energy runs in years 1983-85 had higher background in the tracking chambers and are quite inhomogenous, their analysis would be therefore more difficult. It has been decided to abandon those data, especially in view of their low statistics (nearly 4 times lower than from 1986 running). The data collected before installation of the vertex detector are for obvious reasons unusable in this analysis.

There are 31176 hadronic events selected from the data collected in 1986. Two additional cuts were applied: first, for a few runs the VXD had known hardware readout problems or was completely off. These runs were rejected. Second, it was required that the run had a well reconstructed beam spot, with χ^2/D.F. < 1.5 in the beam spot fit. After these cuts 30520 events were left.

Due to required good tracking efficiency, tracks found by the FELIX trackfinder were used (see section 3.2). As the tracking precision in the $r-\phi$ plane is in TASSO by an order of magnitude better than in the z direction, all the vertex finding has been done in the two dimensional projection onto the $r-\phi$ plane. The tracks used were nevertheless required to be reconstructed in three dimensions, in order to reduce the background of badly reconstructed or 'ghost' tracks (tracks constructed by the pattern recognition program mainly from noise and stolen hits). Three dimensional track information was also needed to measure the angles between tracks for the purpose of jet definition.

All the tracks in the event were first refitted in $r-\phi$ using the program written by David Saxon (described in section 3.2). Pion mass has been assumed for calculation of the multiple scattering effects. The purpose of this fit was twofold; to improve the measurement of the track parameters before using them and to prepare for the vertex fitting in the next stage. Refitted tracks were subject to selection with the following cuts:

1. track had to be reconstructed in three dimensions,
2. the refit of the track had to be successful,
3. $\chi^2_{r-\phi}$/D.F. < 3, χ^2 given by the refit was used,
4. χ^2_{s-z}/D.F. < 20,
5. $d_0 < 5\,\mathrm{cm}$,
6. $p_T > 0.1\,\mathrm{GeV}/c$,
7. $|\cos\theta| < 0.87$,
8. $z_0 < 20\,\mathrm{cm}$,

all symbols are in standard TASSO notation explained in section 3.1. These cuts were modelled on the normal TASSO track quality criteria (see section 3.3) but have been applied here to the refitted FELIX tracks. Those tracks which passed the above cuts were used to calculate the event sphericity axis and for the interaction point finding.

After the sphericity axis had been found, a second stage of track selection was performed. Its purpose was to select candidate tracks for vertex finding. The following cuts were applied:

9. Track had to pass the cuts 1.-8.,
10. $p > 0.6\,\mathrm{GeV}/c$,
11. $\chi^2_{r-\phi}$/D.F. < 1.8,
12. $d_0^{beam} < 0.2\,\mathrm{cm}$, d_0^{beam} denotes the distance of closest approach to the centre of the beam spot,
13. $z_0 < 10\,\mathrm{cm}$
14. There had to be at least 4 VXD hits associated with the track.

These cuts are supposed to remove all poor quality tracks and all tracks coming from secondary processes like V^0 decays or γ conversions. The momentum cut was done to reduce effects of multiple scattering in the beam pipe and in the VXD. The last cut removed tracks which, due to lack of VXD hits, had big tracking errors. Those tracks are not interesting for this analysis as they do not give any reasonable constraint on the vertex position. There were on average 5.2 tracks per event surviving the selection.

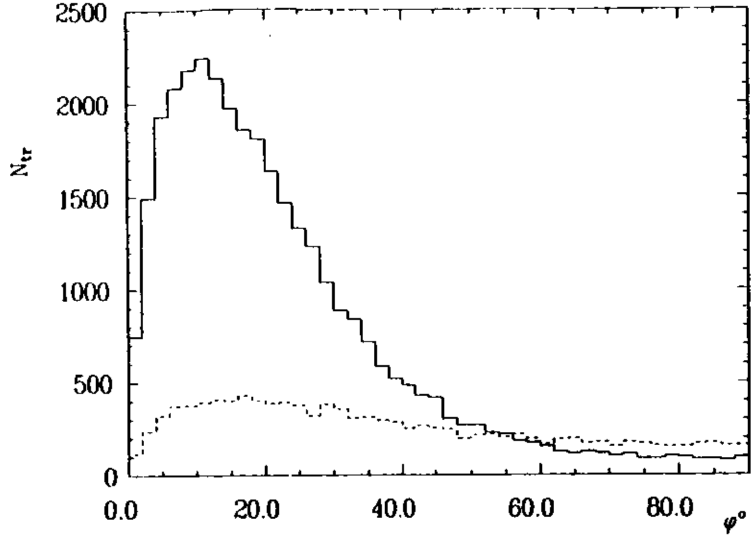

Figure 4.5: The Monte-Carlo distribution of the angle between the track and event sphericity axis in b events. Solid line shows tracks coming from decay of a B hadron (directly or via secondary decays), the broken one shows primary fragmentation tracks.

In the next step was to group the surviving tracks into jets. For the purpose of this analysis a jet was defined as a collection of tracks laying within a cone of 50° from the event sphericity axis, on one side. As the Monte-Carlo studies show, the angular cut enriches the jet with tracks coming from B decay (fig. 4.5). Two lists of tracks, corresponding to the two jets, were assembled in this way and passed to the vertex finder. From this point on both jets were considered separately, i.e. vertex finding was done twice per event, each time using the tracks from one list only.

4.4 Finding the Interaction Point

The idea of tagging is to locate the decay point in the b jet. To do this two things are needed: the vertex and the reference point against which it can be compared. One can think of using as a reference point either the vertex of the opposite jet or the interaction point. The former idea, at first sight attractive as not requiring any measurements in addition to the vertex finding, has however several serious drawbacks. First it requires good vertex finding efficiency in order to get a significant number of events with two reconstructed vertices. Secondly, it would be more difficult to use the tagged events for any physics analysis, as one has to make some assumptions about the whole event (e.g. that there are enough tracks to fit a vertex in both jets). Using the interaction point as reference leaves the jet opposite to the one constituting a tag as 'unbiased' by the tagging method, the resulting sample is more suitable for analysis of the b jet properties. It has been therefore decided to use the separation between the interaction point and jet vertex as the tagging variable.

Chapter 3.4 explained how the position of the beam spot centre was reconstructed for a run. The individual event interaction points are scattered around the centre with spread of about 350 μm in the horizontal (x) direction and 80 μm in the vertical direction. On the other hand the track impact parameter resolution was measured to be around 150 μm. This suggests that it should be possible to get a better estimate of the x position of the interaction point on the event-by-event basis.

The procedure for finding the interaction point was proposed by D. Su [18]. His procedure has been adopted in this work with some modifications. These modifications were necessary, as an event-by-event estimate of the interaction point position error was required.

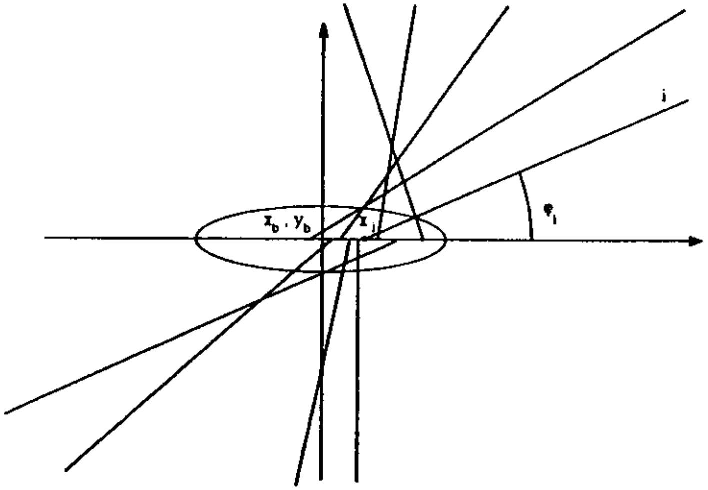

Figure 4.6: Illustration of the idea of the interaction point finding procedure.

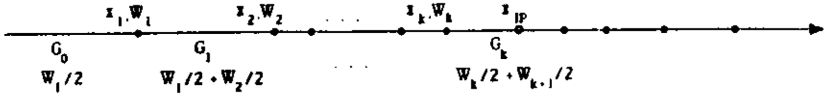

Figure 4.7: Illustration to the gap weighting in the IP finding.

Tracks remaining after the first stage cuts (cuts 1.–8. described in previous section) were used. It has been assumed that the y coordinate of the beam represented also y of the interaction point $y_{IP} = y_{beam}$. The reason for this assumption is that the intrinsic vertical size of the beam spot is much smaller than the error in its location – consequently the run-by-run reconstruction gives the best estimate one can have in this coordinate.

In order to find the x location of the interaction point the following procedure was used:

For all tracks with $p > 0.2\,\mathrm{GeV}/c$ the intersection points x_i of their $r - \phi$ projections with the horizontal line $y = y_{beam}$ were found (fig. 4.6). The intersections laying far from the beam spot centre $|x_i - x_{beam}| > 0.25\,\mathrm{cm}$ were rejected. Each remaining intersection was assigned a weight $W_i = |\sin\phi_i|$, the weight accounted for worse precision in the determination of x_i for horizontal tracks (compare fig. 4.3). This choice of weight was recommended in the original work of Su [18]. The weight of the tracks with momentum $p < 0.7\,\mathrm{GeV}/c$ was in addition halved to reflect their poorer tracking precision due to multiple scattering. The intersection points were then sorted according to increasing x, and each gap was assigned a weight equal to the mean of the weights of neighbouring tracks (fig. 4.7). The weights of the gaps were then added from left to right, until the sum reached $W/2$ where $W = \sum W_i$. Assuming it happened at gap k the interaction point was estimated to lie inside this gap at

$$x_{IP} = \frac{W_k x_k + W_{k+1} x_{k+1}}{W_k + W_{k+1}}.$$

The above procedure used only the two middle track intersections to locate the interaction point. This was preferred over calculating the weighted average of all the tracks for two reasons. First, a single badly reconstructed track with x_i far from the true location does not affect the reconstructed IP position. Second, this procedure remains approximately correct even when tracks from secondary decays are included. To see this, notice that the secondary decays produce on average an equal number of particles to the left and to the right from the direction of the decaying particle. For a vertically going jet the decay is thus no problem - the intersection points simply get more spread around the interaction point. For a horizontal jet the intersections of the decay product tracks with the axis will appear shifted form the interaction point. The method will however tend to pick for the calculation tracks from the primary fragmentation, which have their x intersections in the region between the decay points.

The above algorithm was checked using the QCDFF Monte-Carlo set (see section 3.5). Figure 4.8 shows the distribution of the difference between the Monte-Carlo generated interaction point coordinate x_{true} and the reconstructed one x_{IP}. For comparison, the broken line shows the beam profile used by the Monte-Carlo program - this is how the distribution would look like if the beam spot centre had been used as an approximation of the production point.

One problem is however left - it is a question of the error of the reconstructed IP position. The dotted line in figure 4.8 is the gaussian fit to the central part of the distribution. It can be seen, that the distribution deviates from the gaussian shape in the tails. The deviation is caused by events events in which the IP was poorly reconstructed due to lack of tracks, or with a majority of tracks going in the horizontal direction. It was therefore not possible to assign an universal error value to all the reconstructed interaction points - a more sophisticated algorithm for finding the error for each individual event was required.

To find the error estimate it was assumed that the error of the interaction point reconstruction depends primarily on W, the sum of weights in the reconstruction procedure. This seems a reasonable assumption, as one expects the precision to increase with the number of tracks, and also to increase for vertical events as compared with horizontal ones. In order to check this assumption a number of distributions of $x_{IP} - x_{true}$ were made in different intervals of W for the Monte-Carlo events. Figure 4.9 shows the r.m.s. width of those distributions as a function of W. The dependence of the width on W has been parametrised as

$$\sigma_{x_{IP}} = \frac{550}{\sqrt{W}} + 50\ [\mu\mathrm{m}]$$

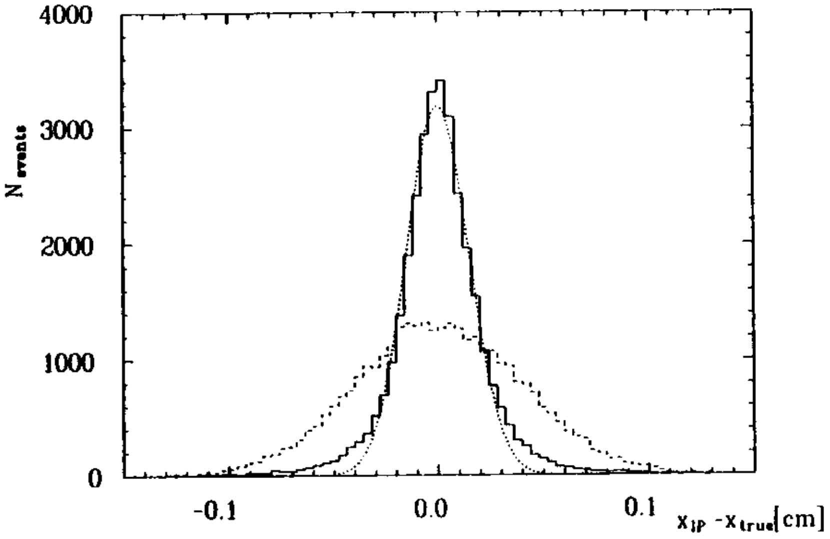

Figure 4.8: The Monte Carlo distribution of the difference between true and reconstructed interaction point. The dotted line is a gaussian fit to the central part of the distribution. For comparison the beam profile is shown as a broken line.

(in figure 4.9 this parametrisation is shown as a dashed curve). The parametrisation was deliberately made to overestimate the error in order to compensate for the fact that the centre of the beam spot in the data was known with finite precision while in the MC it was just put in and thus known exactly. Figure 4.10 shows the Monte-Carlo distribution of the deviation $x_{IP} - x_{true}$ divided by the error estimated from the parametrisation in fig. 4.9. For comparison a normal gaussian curve has been superimposed. The plot confirmed the assumption that the error in the IP determination depends mainly on W. The tails of the distribution are now approximately gaussian.

The full algorithm of interaction point finding was thus as follows: first, the x_{IP} was estimated according to the above described procedure of 'weighted median point' finding. Then its error was calculated according to the parametrisation given above. This error was then compared to the beam spot x size (assumed to be $350\,\mu\mathrm{m}$). If it was greater, then the beam spot centre position was used as the interaction point x coordinate, and the beam spot size as the error. Otherwise the calculated values were used. The y coordinate of the beam spot centre was taken as the y coordinate of the interaction point, and error from the beam spot position determination was used as σ_y.

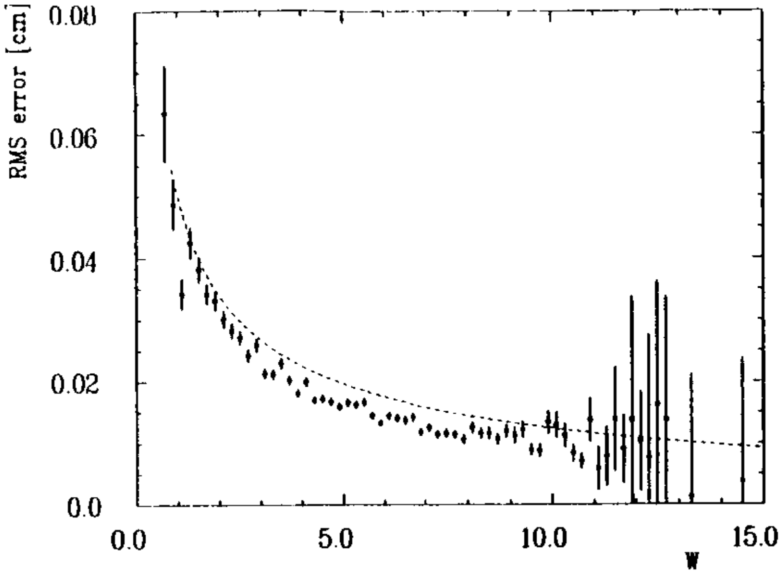

Figure 4.9: The interaction point reconstruction error as a function of sum of track weights W. The dashed line shows the parametrisation used.

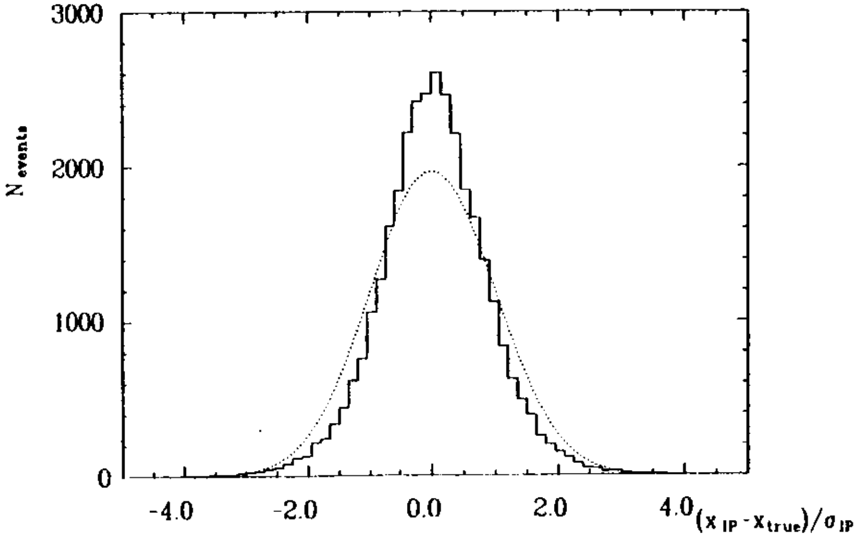

Figure 4.10: MC distribution of the IP reconstruction error normalized to the estimated error.

4.5 Vertex Reconstruction

4.5.1 Vertex fitting

Before describing the procedure of finding the jet vertex it is worth to present the algorithm used to fit a vertex to a given track combination. This vertex fitting routine has been called always when the vertex finder decided to try a particular combination of tracks as a vertex candidate.

As a first step a number of cuts were applied to the vertex candidate.

1. $|\sum q_i| \leq 3$, q_i is charge of the i-th track,
2. $\max \Delta\phi > 0.3\,\text{rad}$, $\Delta\phi$ is the angle between a pair of tracks measured in the $r-\phi$ plane (thus $\max \Delta\phi$ is the total opening angle of the track combination considered),
3. $\min \Delta\phi > 0.02\,\text{rad}$,
4. $\max \varphi > 0.4\,\text{rad}$, φ is the three-dimensional angle between a pair of tracks.

The first of these cuts required that the total charge of the vertex candidate was reasonably balanced. As the true total charge of a secondary vertex can only be 0 or ±1, this cut was expected to remove some spurious candidates. Cuts 2. and 4. dealt with the opening angle of the vertex candidate. They did not allow vertices with a big error along the flight path to compete with the better reconstructed ones. Second, they removed some of the charm decay vertices, which, as explained earlier, were expected to have smaller opening angles. Cut three forbade fitting to a combination with two tracks very close in $r-\phi$. Such a pair of tracks usually does not constrain the vertex position more than better track of the pair does – but it gives a false assurance of having a high multiplicity vertex. Also, tracks belonging to a close pair have more often misassigned VXD hits, due to pattern recognition problems. It was therefore considered safer to allow at most one of the close pair tracks to participate in the vertex fit.

If the candidate passed the above cuts the vertex fit was attempted. The program of David Saxon [25] was used again. The fitting procedure used was the same as for the track fits, only in this case the fit was performed simultaneously to the list of tracks, and the tracks were constrained to have a common point (technically it was done by making the x and y position of the intersection point free parameters of the fit, and removing d_0 as fit parameter from the tracks). It is easy to see that an additional constraint exists only when fitting to three or more tracks. The fitting procedure returned the fitted parameters (of which x and y of the vertex were further used), full error matrix, χ^2 of the fit and the increase of χ^2 as compared to unconstrained track fits. This quantity, further called $\Delta\chi^2$, has itself a χ^2 distribution with $n-2$ degrees of freedom (n is number of tracks) – if the tracks indeed originate from a common point. $\Delta\chi^2$ could thus be used to reject those fits in which the tracks did not share a common vertex.

The following cuts were applied after the vertex fit:

1. The vertex fit had to be successful,
2. $\chi^2/\text{D.F.} < 1.3$ in the vertex fit,
3. The confidence level associated with $\Delta\chi^2$, $\text{CL}(\Delta\chi^2, n-2) > 5\%$.

The last step of vertex fitting was evaluation of the quantity called vertex quality for those vertices which passed all the above cuts. The need for a single number which somehow describes the 'usefulness' of the vertex is clear: as said in the previous section, at some point in the analysis the best vertex found in a given jet should be chosen. This best vertex should maximize the number of participating tracks, ensure that the tracks intersect well and be constructed, if possible, of the best tracks found. In practice it would be rare that a single vertex is the best one in all categories. Various trade-offs were therefore needed, vertex quality was the quantity which implemented those trade-offs.

The basic formula used for calculating the quality was

$$Q = \log_{10}\mathrm{CL}(\chi^2, N_{DF}) + 2\log_{10}\mathrm{CL}(\Delta\chi^2, n-2) + 0.09N_{VXD}$$

where:

$$\mathrm{CL}(\chi_0^2, n) \overset{\mathrm{def}}{=} \int_{\chi_0^2}^{\infty} d\chi^2\, P_n(\chi^2)$$

is the confidence level associated with χ_0^2 for a χ^2 distribution with n degrees of freedom, N_{DF} is a number of degrees of freedom in the vertex fit and N_{VXD} is the number of Vertex Detector hits associated with all the participating tracks. The usage of log in the formula ensured that fits with accidentally low χ^2 or $\Delta\chi^2$ were not rewarded too much compared to good but less 'lucky' ones, but on the other hand that the vertices with low confidence levels were strongly discouraged. The first term measures the quality of the overall fit – this is dominated by the χ^2 contributions from the track fits, as the cut on $\Delta\chi^2$ does not let the intersection quality to contribute too much. The second and most important term measures the quality of the intersection, discouraging the vertices composed of poorly intersecting tracks. The purpose of the third term is twofold: it promotes the vertices composed of tracks with many VXD hits (thus having smaller tracking errors) and also encourages the vertices with many tracks (as more tracks mean more VXD hits). The coefficients in the above formula have been chosen with the help of a Monte-Carlo, as to give possibly low quality to background vertices in light quark events while mantaining the good quality of well reconstructed B decay vertices. The actual procedure of tuning them will be explained in the next section with more detail.

Two additional corrections have been also suggested by the Monte-Carlo to the above formula in order to avoid badly reconstructed vertices in light quark events (which contribute then to the background). One was to discourage the vertices having a track with momentum just above the cut (it was not possible just to raise the momentum cut, as the efficiency dropped then rapidly due to lack of tracks). A correction in the form

$$\Delta Q = 8(p_{min} - 0.75) \qquad \text{if } p_{min} < 0.75$$

with p_{min} being the momentum of the softest participating track in GeV/c, was introduced. This way vertices constructed exclusively of high momentum tracks (less affected by multiple scattering) were preferred.

A second correction was introduced after the discovery that good vertices sharing more than four tracks should be additionally rewarded, as they made a negligible contribution to the background. The vertex finder however often preferred a worse four track vertex due to its better χ^2. An additional bonus of 0.4 was therefore added to the quality of the vertices composed of more than four tracks.

Parameters of a successfully fitted vertex were then stored for the vertex finder.

4.5.2 Vertex finding

The role of the vertex finding algorithm was to find among possible track combinations in a jet the one with gives the best vertex and to locate this vertex. The criteria used in this search have been explained above. Basically the vertex finder as described here had to generate different track combinations, present them to the vertex fitter and compare the results in order to find the highest quality vertex.

As mentioned in the description of the vertex fitter, the minimum number of tracks which allowed for a constrained vertex fit was three. Therefore if a jet had less than three accepted tracks, no vertex could be found. For jets with exactly three tracks the algorithm was straightforward – the three-track fit was attempted and, if successful, the resulting vertex was marked as 'jet vertex'

In the four track case the algorithm attempted first a fit to the whole four-track list. If the fit was successful and it resulted in a good vertex with quality $Q > 1$, this was immediately accepted as 'jet vertex'. Otherwise the algorithm tried all possible three-track combinations, and picked as a final fit the highest quality vertex found.

The many track case was treated in a different way. Theoretically one could just try all possible combinations of more than three tracks and choose the best one. In practice however this would be a disaster from the point of view of the computer time needed (the time would grow approximately as $n!$ with the number of tracks in a jet). In addition this growth in computing time would not bring a true improvement in the quality of the final vertex location – among this great number of combinations there would be probably more than one precise enough to be used. For these reason the algorithm was applied whose goal was to possibly quickly find one of those good combinations.

The idea of this search was to start with a 'small' vertex with three tracks only and 'grow' it by adding tracks if it seemed promising. The actual algorithm sorted first the list of tracks belonging to a jet, so that good high momentum tracks with many VXD hits associated to them landed on top of the list. Then all combination of three tracks out of top five from the list were formed and the fit was attempted to each of those combinations in turn. Each time a fit was obtained with quality of the vertex $Q > -1.5$, an attempt was made to add a fourth track (by going down the sorted list). Each time the addition gave an improvement in the quality, the program tried to add a fifth track in the same way. The algorithm proceeded until a five-track vertex with $Q > 1.3$ has been found, or all the three-track combination out of the best five have been checked. In the former case the jet vertex was the one at which the search stopped, in the latter case it was just the best one among all tried. No attempt was made to go beyond five tracks, as this did not bring any significant improvement in the precision of the vertex determination.

The above algorithm applied to the data yielded 14460 jet vertices in 61040 jets. The low overall efficiency of the procedure was caused mainly by the tightness of the track quality cuts – only 40% of all the jets had at least three tracks remaining after selection.

Figure 4.11 shows the positions of all the vertices with respect to the interaction point. The jet axis points towards positive x (to the right on the picture). The majority of the vertices are found to occupy an elliptical region of size $\sigma_x \approx 500\,\mu$m and $\sigma_y \approx 150\,\mu$m. For comparison, the average lengths of the long and short axes of the vertex position error ellipse given by the vertex fitter were $\langle\sigma_{long}\rangle = 430\,\mu$m and $\langle\sigma_{short}\rangle = 100\,\mu$m. The spread is thus seen to agree well with the vertex fit error combined with the interaction point position errors. This agreement provided a check of the correctness of the vertex finding procedure and vertex error calculation.

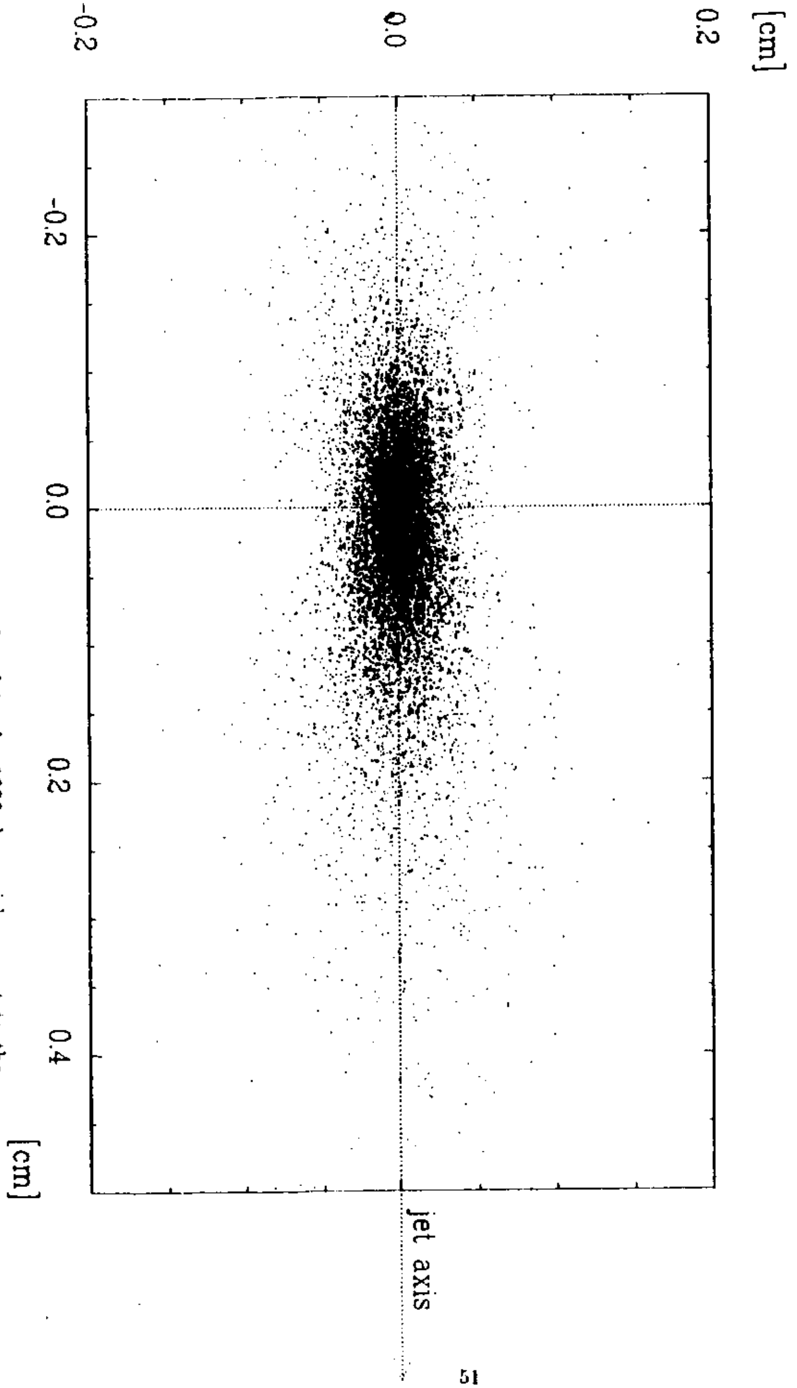

Figure 4.11: Positions of all the jet vertices found in the 1986 data with respect to the interaction point.

While the majority of vertices reconstructed lie within this central region, one can see on figure 4.11 a long halo of vertices far from it. More careful examination of the figure reveals that the halo is asymmetric – there are clearly more vertices shifted from the interaction point in the flight direction of a jet then opposite to it. This asymmetry suggests that at least some of the halo vertices are indeed reconstructed secondary decay points, as the background from wrong reconstructions is not expected to prefer one of the directions.

Figure 4.12 shows a few examples of events with found jet vertices. Each window represents a $5 \times 5\,\mathrm{mm}^2$ fragment of the $r - \phi$ plane around the interaction point. The vertices and the interaction point are marked by crosses with error ellipses (the interaction point by a dashed ellipse). Solid lines are the tracks used for the vertex fit. Other tracks which passed the track quality cuts but have not been used in the vertex reconstruction are shown as broken lines.

Picture a) presents the most typical case – an event with a single vertex close to the interaction point. The errors of both points overlap – one can thus say that the vertex is consistent with coming from the primary fragmentation. The opposite jet had too few tracks to attempt a vertex fit.

The example in figure b) is more complicated: both jets have the vertices reconstructed. The distances from the interaction point are roughly equal for both vertices – however their significance is different. The lower vertex overlaps strongly with the interaction point, while the other is separated from it by about two standard deviations. This example shows why it is important not to use the absolute distances for the purpose of tagging.

The third example (fig.4.12c) shows an event with a vertex nicely separated from the interaction point – unfortunately the vertex lies 'behind' the interaction point as seen by the jet, thus it can not be a secondary decay vertex. Close examination of the figure reveals that the vertex has been pulled out of the IP by a single track – presumably a badly reconstructed one. This example presents a possible source of background to the tagging – the vertex would have been accepted as a decay point if the tracking error went in the opposite direction.

The last picture shows an example of an event with vertices reconstructed in both jets. Both vertices are clearly separated from the production point. This is an example of a 'double tag' – an event with secondary decay points seen in both jets. Events like this were later used for determination of the tagging efficiency (as will be explained in the next section). The probability that this event is an example of $b\bar{b}$ production was estimated to 96%.

4.5.3 Vertex Separation

To define a b tag one needs some means of measuring the relative distance between the vertices and the interaction point. As has been said before, this calculation must take into account the reconstruction errors (compare vertices in fig. 4.12b). A quantity called 'separation' has been invented for this purpose. Its definition is given below.

Assume that the coordinates of two points have been measured in the (x, y) plane. Let (x_1, y_1) and (x_2, y_2) be the measured coordinates of these points. Assume further that the error matrices for both measurements are known:

$$\sigma_1 = \begin{pmatrix} \sigma_1^{xx} & \sigma_1^{xy} \\ \sigma_1^{xy} & \sigma_1^{yy} \end{pmatrix} \qquad \sigma_2 = \begin{pmatrix} \sigma_2^{xx} & \sigma_2^{xy} \\ \sigma_2^{xy} & \sigma_2^{yy} \end{pmatrix}$$

Consider now the hypothesis that both those points represent the measurements of the same 'true' point (see figure 4.13). One can find the most probable coordinates of this common

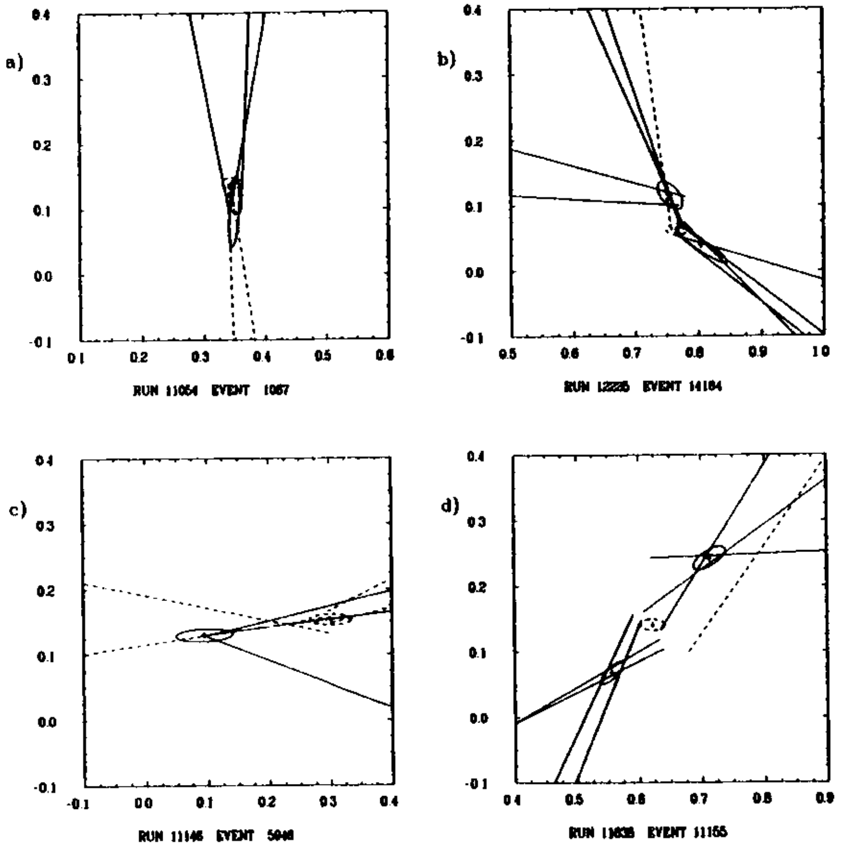

Figure 4.12: Examples of events with found vertices. The scale on the axes is in centimetres.

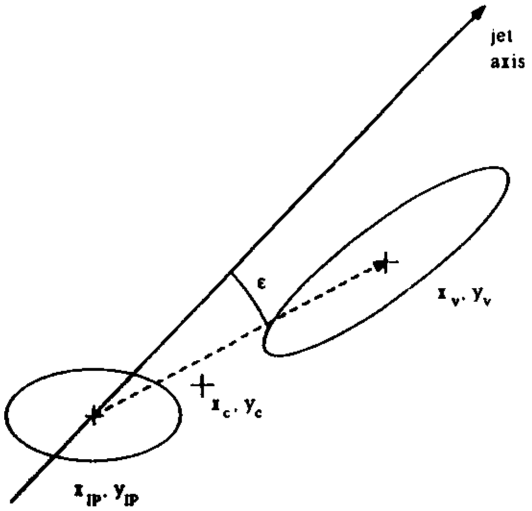

Figure 4.13: Illustration to the definition of separation variable.

point $\mathbf{x}_c = (x_c, y_c)$ by minimising the χ^2

$$\chi^2 = (\mathbf{x})(\sigma_1)^{-1}(\mathbf{x})^T + (\mathbf{x} - \Delta\mathbf{x})(\sigma_2)^{-1}(\mathbf{x} - \Delta\mathbf{x})^T$$

with respect to $\mathbf{x}$. Taking the partial derivatives and solving the resulting equations gives

$$\begin{aligned} x_c &= \frac{(x_2 - x_1)(s^{xx}\sigma_2^{yy} - s^{xy}\sigma_2^{xy}) - (y_2 - y_1)(s^{xx}\sigma_2^{xy} - s^{xy}\sigma_2^{xx})}{s^{xx}s^{yy} - (s^{xy})^2} + x_1 \\ y_c &= \frac{(y_2 - y_1)(s^{yy}\sigma_2^{xx} - s^{xy}\sigma_2^{xy}) - (x_2 - x_1)(s^{yy}\sigma_2^{xy} - s^{xy}\sigma_2^{yy})}{s^{xx}s^{yy} - (s^{xy})^2} + y_1 \end{aligned}$$

where the $\mathbf{s}$ matrix has been introduced as

$$\mathbf{s} = \sigma_1 + \sigma_2.$$

The above solution may be now used to calculate the minimal χ^2:

$$\begin{aligned} S = \chi^2_{min} &= \frac{(x_c - x_1)^2\sigma_1^{xx} - 2(x_c - x_1)(y_c - y_1)\sigma_1^{xy} + (y_c - y_1)^2\sigma_1^{yy}}{\sigma_1^{xx}\sigma_1^{yy} - (\sigma_1^{xy})^2} \\ &+ \frac{(x_c - x_2)^2\sigma_1^{xx} - 2(x_c - x_2)(y_c - y_2)\sigma_1^{xy} + (y_c - y_2)^2\sigma_1^{yy}}{\sigma_1^{xx}\sigma_1^{yy} - (\sigma_1^{xy})^2}. \end{aligned}$$

If the hypothesis that both points are indeed two measurements of the same point is correct, S should have a χ^2 distribution with two degrees of freedom (the other two degrees of freedom have been used up in calculating x_c and y_c). The quantity S is further called the separation of points 1 and 2.

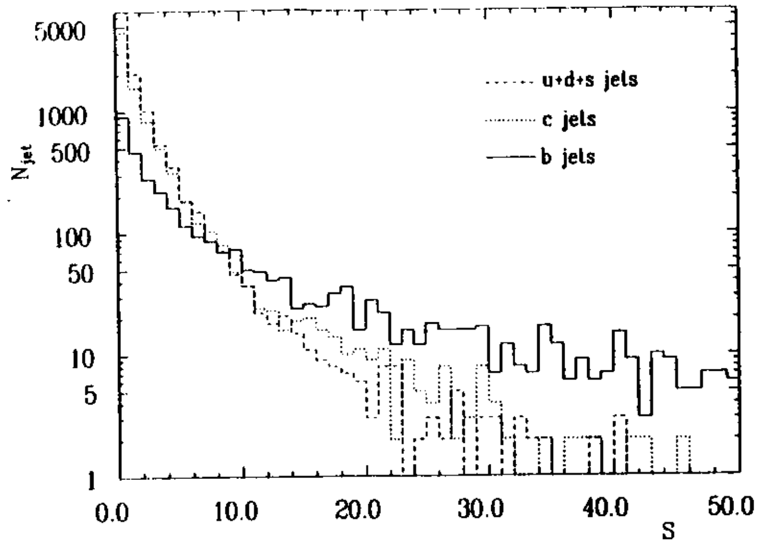

Figure 4.14: Raw separation distribution in the Monte-Carlo.

The above definition conforms to the intuitive notion of separation. If the two points are so close to each other that the error ellipses partially overlap, one feels that they are weakly separated, and can easily think that they are two images of a single point. If on the other hand the points are far away, so that the measurement errors are small compared to the distance between the points, one has to admit that it is difficult to think about the points as having a common origin. The above definition of separation can be trivially extended to more measurements if needed. Also, a definition of three dimensional separation would be an obvious extension.

In the present analysis the two measurements are the position of the interaction point (x_{IP}, y_{IP}) and the jet vertex (x_v, y_v) (or, in another variant, the two jet vertices). A small value of separation between them means that the jet origin is consistent with the interaction point, i.e. that no evidence for a decay of a long lived object can be found. S was thus further used as a basic quantity defining the b tag.

4.5.4 Monte-Carlo modelling and Cut Optimisation

In order to check the feasibility of the method and also to optimise all the program parameters and selection cuts a Monte-Carlo experiment was performed. The input data set was the one described as 'QCDFF' in section 3.5. The simulated events were analysed in the way described above.

Figure 4.14 shows the distributions of the vertex-IP separation S for $u+d+s$, c and b events. Most entries are grouped, as expected, around zero but a long tail of vertices with high separations is clearly visible. This tail is populated mainly by the b events, but there are also some lighter quark jets which found the way there. In order to see how the composition of the tagged sample changes with the separation cut applied, the distributions from fig. 4.14

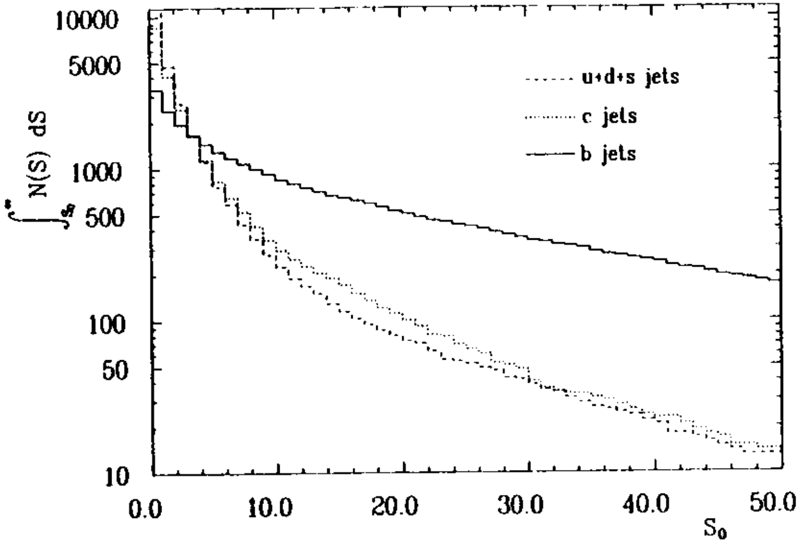

Figure 4.15: The number of events accepted as a function of the separation cut.

have been integrated from right to left, and the results (i.e. the number of events passing the given separation cut) are shown in figure 4.15. Clearly at high cuts b jets dominate – on the other hand even at the highest separation values there remain more than 10% background jets in the tagged sample. It is interesting to notice that the charm contribution is only slightly higher than that from the light quarks – this is the result of using the separation variable instead of just the vertex distance for tagging.

In order to suppress this background some additional selection criteria were introduced. Figure 4.16 shows the the angle between the sphericity axis and the 'vertex direction' (angle ϵ in fig. 4.13) for the vertices with separation $S > 3$. In the light quark case the distribution is forward-backward symmetric, as expected for a background of badly reconstructed vertices. For the b's the distribution is sharply peaked in the forward direction, only a few vertices lie 'behind' the interaction point. Cutting on ϵ can thus purify further the tagged b sample. The optimum value of this cut depends slightly on the separation cut applied, but usually lies between 20 and 25 degrees. At lower values of ϵ one loses good b vertices nearly without gain in purity, at higher values the number of background vertices accepted starts to grow faster than the number of b's.

One more possible way to further purify the b sample was explored. It used the vertex quality Q, originally introduced for the purpose of choosing the best vertex in a jet. As the definition of Q was tuned to give possibly high quality to well reconstructed vertices, one could expect that poorly reconstructed background vertices should have on average lower Q. Figure 4.17 shows the distribution of the quality of the jet vertex, for b and other flavour vertices passing the cuts $S > 3$ and $\epsilon < 23°$. One can see that both distributions are indeed shifted with respect to each other, the average quality of a b vertex is higher by about 0.3 than the average for all other flavours. It is however not possible to exploit this difference for

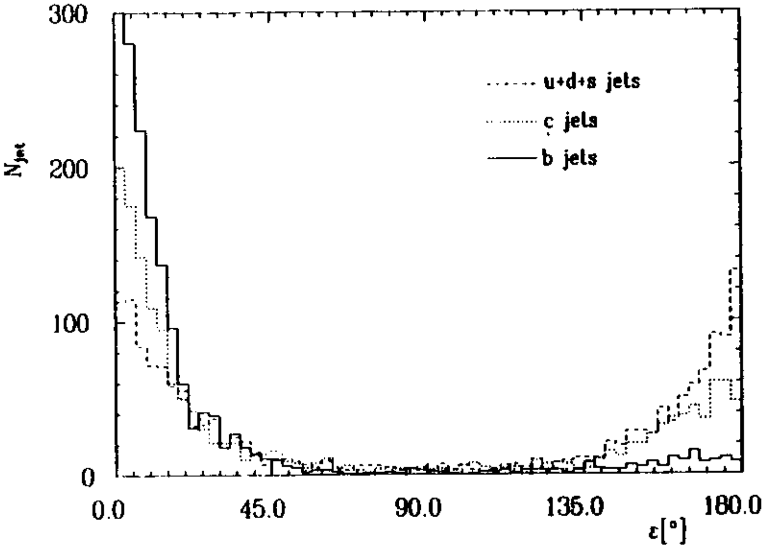

Figure 4.16: The angle between the vertex direction and the sphericity axis.

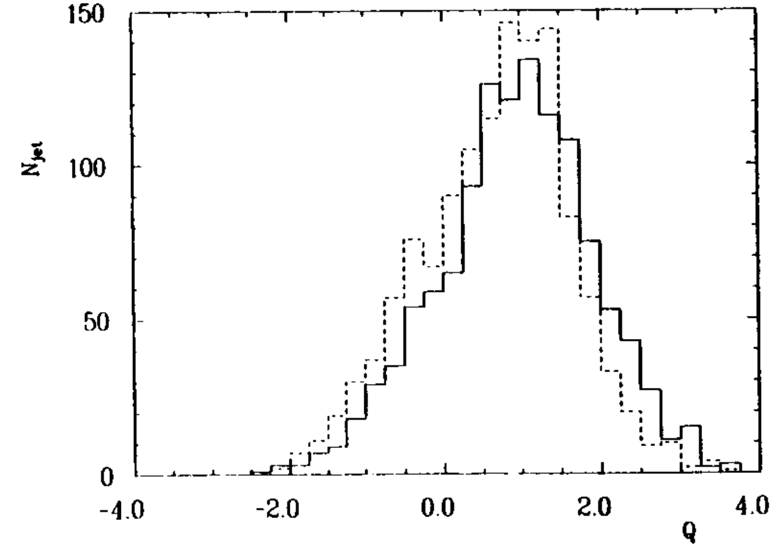

Figure 4.17: Quality Q of the tagged Monte-Carlo vertices. b jets shown as solid histogram, all others added as broken one.

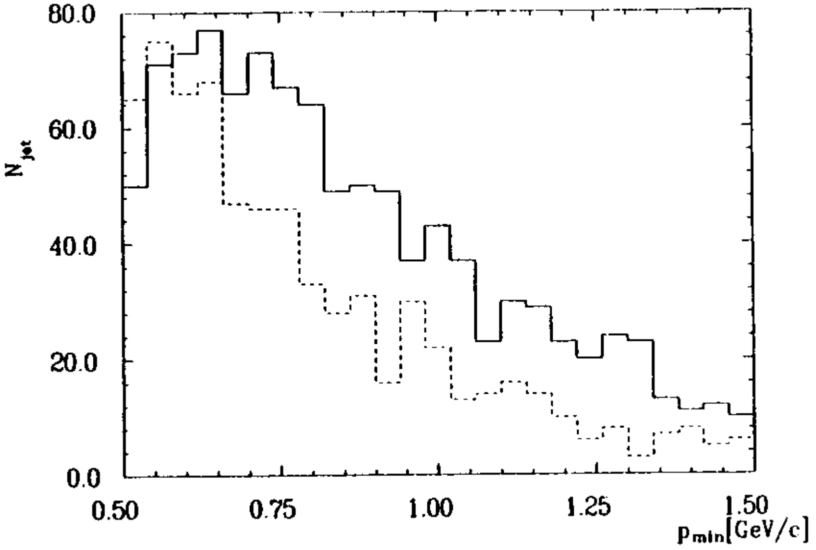

Figure 4.18: Distribution of the momentum p of the softest track participating in the vertex fit for well separated vertices in the Monte-Carlo. Solid line shows the vertices reconstructed in the b events, the broken one those from all other quark flavours.

a significant suppression of the background, unless one is ready to accept a significant loss in efficiency of the tagging, the distributions in fig. 4.17 overlap too much. It was therefore decided to apply only a very soft cut to the data, $Q > -1$, in order to remove very poor vertices (which are often only accidental tags in b jets).

A similar approach was used also to optimize most of the parameters used in track selection and vertex fitting. The general way was to run the vertex finding with some of the cuts more relaxed, and then to compare the distribution of the quantity in question for separated vertices from b's and from other quark flavours. An example of such a distribution is shown in fig. 4.18. It shows the distribution of the momentum of the softest track participating in the vertex found. The momentum cut for tracks was set to 0.5 GeV/c in this case. One can see that the separated $udsc$ vertices more often use a low momentum track than the b ones, their distribution (shown as broken histogram) rises more rapidly with falling p. The analysis of this picture prompted the decision to set the track momentum cut to 0.6 GeV/c, and also caused introduction of the 'low momentum penalty' in the vertex quality formula.

4.6 The Tagged Sample

At this point of the analysis one could already define the 'b tagged sample' by applying the cuts described above. The problem was to determine the number of real $b\bar{b}$ events in the sample. The simplest way would be to apply the same cuts to the above described Monte-Carlo set, count the $b\bar{b}$ events passing them and assume that the same number of events will pass in the data. This proposal raises however several serious objections:

1. The result of the Monte-Carlo simulation depends on physics input of the model used. Input parameters like average B hadron lifetime, b quark fragmentation function, composition of the B hadrons produced or B decay model change the b tag probability by affecting either the decay distance or the probability of secondary vertex reconstruction. Those parameters either have been measured but have significant errors, or (as the composition of B hadrons produced) have not been measured at all. Also, the non-b background estimation given by the model may be wrong, as it may depend on details of the fragmentation process.

2. The results of this analysis strongly depend on the detector parameters – especially on the vertex detector parameters (efficiency, noises, resolution etc.). The detector simulation program must be written so as to reproduce perfectly the detector behaviour. This is of course not possible in practice, one has to make many simplifications, which then affect the outcome of the simulation. This was a quite serious problem, as no independent detector simulation program was available as a cross-check.

As a check for a possible effect of a first cause, the results given by two different Monte-Carlo models were compared. The models used were QCDFF (used earlier for cut optimisation) and LUND63. Already the vertex finding efficiency turned to be quite different for both models (the program found more vertices in LUND events than in the QCDFF). Both models show a systematic difference in the purity estimation for the same sets of cuts – for some cuts the difference can reach 20% in the absolute value of purity! As one can not choose between the models used, the difference would have be put into the systematic error when using the Monte-Carlo.

Also, it was checked that the average size of the vertex error matrix given by the model differed slightly, but significantly from the data. This could indicate that the simulation of the detector was not perfect.

For the above listed reasons it was decided not to use the MC, but instead to deduce the sample purity directly from the data. The method proposed for this purpose was called 'double tag method' and is explained below.

4.6.1 The Double Tag Method for Purity Determination

The double tag method is based on the fact that an event has two sides or two 'jets' (in the sense defined in section 4.3). An event has thus two chances to be tagged. The key assumption now is that the probability of getting a tag in a jet is not affected by presence of a tag in the opposite jet. If this assumption is true then the only mechanism which correlates the tags in both jets is the flavour of the quark initiating the jet, which is the same on both sides. Assume that one started with N events and obtained after the analysis k tagged jets and l events with both jets tagged. One can write

$$\begin{aligned} k &= 2N(f_l p_l + f_c p_c + f_b p_b) \\ l &= N(f_l p_l^2 + f_c p_c^2 + f_b p_b^2) \end{aligned}$$

where f_l, f_c, f_b are fractions of uds, c, and b events in the starting sample and p_l, p_c, p_b are the probabilities of finding a tag in a jet respectively. It has been assumed that the probabilities of finding a tag are equal for u, d and s primary quarks. If the f's are known, then there are only three unknown p's in the above equations. One additional constraint would thus allow to find all the p's and to calculate from them the number of b's in the tagged sample.

Experimentally N, k and l are easily accessible. All the f's can be extracted relatively safely from the Monte-Carlo. The problems are to prove the independence of the tag probabilities and to find the 'third constraint' for the p's.

The independence of the tags in opposite jets is built into the tagging method used - by the fact that the tagging procedure uses always the information from one jet only and does make any assumptions about the properties of the other jet. Also the event acceptance cuts applied at the beginning do not produce jet-jet correlations as they are caused by hardware reasons, independent of the event properties[1].

The additional constraint on the tag probabilities must be unfortunately taken from the Monte-Carlo simulation. It was decided to take for this purpose the ratio between the c and uds tagging probabilities p_c/p_l. This ratio should not be strongly model dependent as the charm lifetimes and decays are reasonably well known, and any 'common' errors introduced by the fragmentation model or detector simulation procedure should tend to cancel. Taking

$$\frac{p_c}{p_l} = a$$

one can solve the resulting system of equations to obtain

$$p_b = \frac{1}{2N}\,\frac{kv + \sqrt{4Nlu(v + u/f_b) - uvk^2/f_b}}{u + f_b v}$$

where two additional constants u, v have been introduced

$$u = (f_l + af_c)^2, \qquad v = f_l + a^2 f_c.$$

The statistical error on p_b can be easily calculated using the standard statistical methods – in fact is is usually dominated by the statistical error on the number of double tags l.

Figure 4.19 shows the result of applying the double tag method to the data. Drawn is the fraction of b events in the tagged sample as a function of the separation cut with other cuts fixed at $\epsilon_{cut} = 23°$ and $Q_{cut} = -1$. The fractions taken from the Monte-Carlo were $f_l = 0.527$, $f_c = 0.373$, $f_b = 0.100$. These values differ slightly from those given by the quark model, due to different detector acceptance for different types of events. The errors are statistical, calculated for each point individually. As the same events are used to calculate the purity for each cut, the point-to-point errors are much smaller. This picture gives the raw estimation of the number of tagged b jets.

4.6.2 Systematic Effects

The above described idea of the measurement needs however some refinement in order to be reliably applied. In particular the key assumption about the independence of the tag probabilities needs careful checking. There exist a few effects which could cause correlations between the tag probabilities and should therefore be investigated. As these effects could in principle depend on special cuts used, it was decided to fix the cuts at this point. The following analysis could of course be repeated for different set of cuts if needed. The b tag for the rest of this chapter is defined as a jet which has a vertex fitted with

1. $S > 5.5$, S is the separation between the vertex and the interaction point.

---

[1] There standard hadronic cuts used can produce certain jet-jet correlations. This effect is discussed in the next section

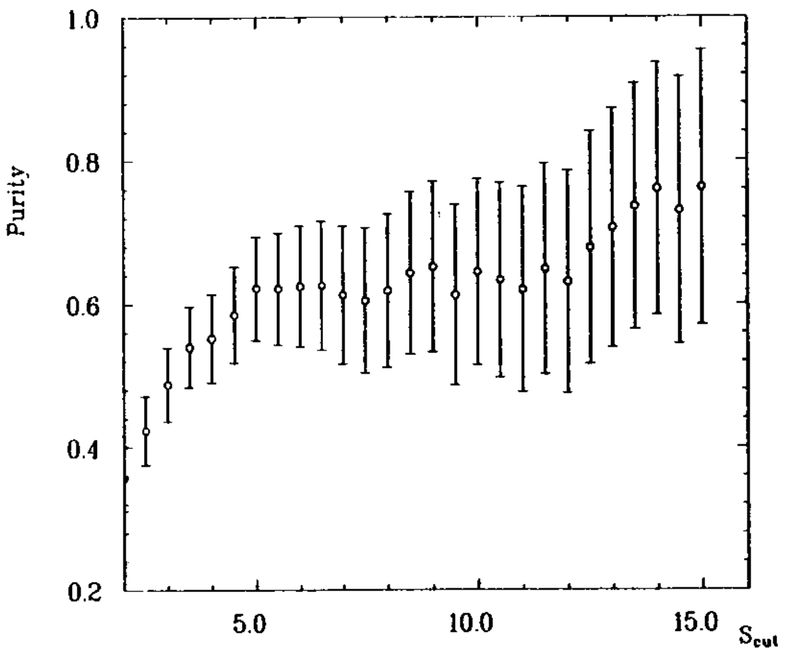

Figure 4.19: Tagged sample b purity calculated from double tags as a function of the separation cut for $\epsilon < 23°$ and $Q > -1$. The purity in the figure is defined as a fraction of b events among the events with at least one tag.

2. $\epsilon < 23°$, the angle ϵ is as defined in figure 4.13
3. $Q > -1$, Q is the quality of the vertex.

In the above sense there were 884 tags found in the data, 29 events had two tags. This translated to $p_b = 0.095 \pm 0.010$ and the purity of the b tags $P = 65 \pm 8\%$, P is defined as a percentage of *b jets* among all the tagged ones. The probability for tagging a light quark jet with these cuts was found to be $p_l = 4.4 \pm 1.5 \times 10^{-3}$ and for the charm quark jet $p_c = 7.8 \pm 2.0 \times 10^{-3}$.

The first effect investigated was an effect of the polar angle of the event, i.e. the angle between the event sphericity axis and the detector axis. The sphericity axis was used as an approximation of the jet axis, thus both jets in the event had always the same polar direction θ. If the probability of the tag depended on θ one would get a correlation in the tag probabilities.

It is easy to propose a mechanism which makes the tag probability θ dependent - it is enough to recall that the whole vertex reconstruction was done in two dimensions. The projected decay distance of the B hadron is related to the true decay distance by $\sin\theta_B$, where θ_B is the direction of the hadron and is usually close to θ. Thus, the decay vertices in jets with

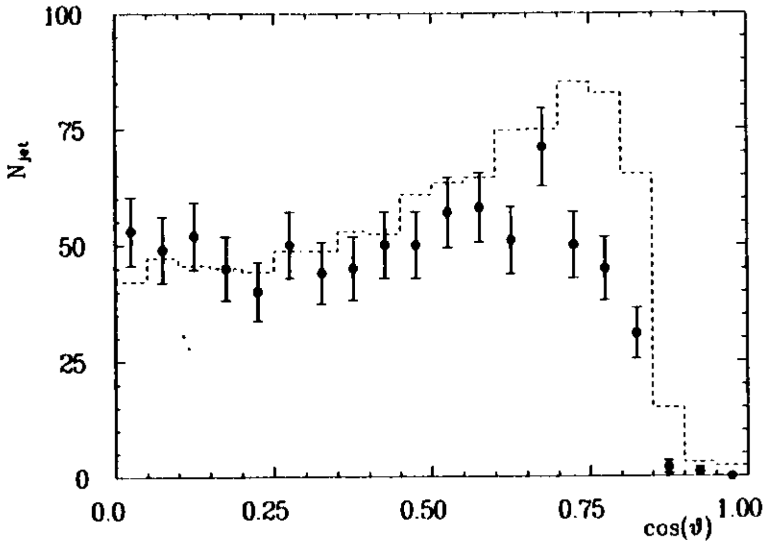

Figure 4.20: The distribution of the tags in $\cos(\theta)$ compared to the distribution of all jets (shown as broken line).

θ close to 0 (or π) lay nearer the interaction point and are more difficult to tag. Fortunately the variable used for tagging is not the distance but the separation, constructed from the distance and its error. The error along the flight direction is related to the projected opening angle of the decay products approximately as $1/\sin(\Delta\phi/2)$ (fig. 4.3). The three dimensional opening angle of the decay products does not depend on θ – it is easy to see that the projected angle $\Delta\phi$ grows when θ becomes smaller. The error on the decay distance determination is therefore expected to be smaller for small θ, possibly partially compensating for the shrinking decay distance.

To see if the tag probability depends on θ, a plot of the number of tags as a function of $\cos\theta$ was made and compared with the distribution in $\cos\theta$ of the original events (fig. 4.20). The circles with error bars show the distribution for the tags, dotted histogram is for all jets. The dotted histogram has been scaled to have the same number of entries in the interval $0 < \cos\theta < 0.4$ as the other one. One sees from the plot that no significant difference between both distributions can be seen up to $\cos\theta \approx 0.7$, but afterwards the the tag probability rapidly drops.

As follows from the above argument, one can use the double tag technique only for tags with $\cos\theta < 0.7$. In the data there are 23030 events fulfilling this condition. Among them 752 tags were found, 26 events were double tagged. The value of P deduced from these numbers is $63 \pm 8\%$.

The next effect studied was the dependence of the tagging probability on the ϕ angle of a jet. One can expect some dependence due to elliptical shape of the interaction region causing the IP errors in x and y direction to be different. The smaller y error makes it a bit easier to tag a vertically going jet than a horizontal one. As the two jets in an event have opposite directions in ϕ, one can expect a positive correlation between the tag probabilities.

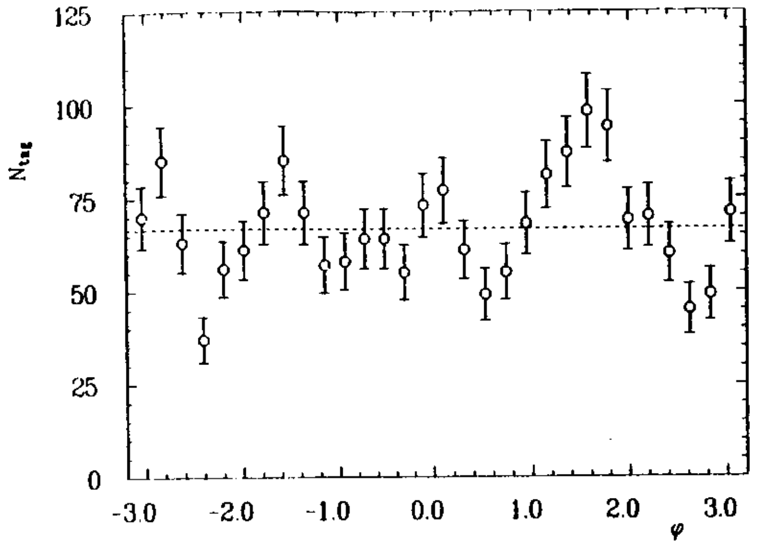

Figure 4.21: The distribution of the tagged jets in ϕ. The horizontal line marks the average value.

As a check a distribution of the number of tagged jets as a function of ϕ was made (fig. 4.21). In order to improve the statistical significance the separation cut was lowered when making this distribution. The plot shows some increase of the number of tags for vertical jets (around $\phi = \pm\pi/2$). One can estimate from this plot how much the probability of getting a double tag differs from $\langle p\rangle^2$ by multiplying the probabilities calculated from the bins separated by π and adding the results. This way it was estimated that the considered effect caused an increase in the probability of double tag by 1–5%, and thus created between 0.3 and 1.3 additional double tags. This correction was entered into the double tag formula giving the corrected value $P = 62 \pm 8\%$.

The last investigated cause for the correlation between the tags was the effect of the hadronic event selection. Recalling from chapter 3, the events must, among others, have some minimal charged multiplicity and some minimal charged energy in order to be accepted as hadronic event. This causes some negative correlations between the properties of the jets, as if one of the jets has for example a very low multiplicity, the other one must have it higher, otherwise the event would never be included in the hadronic data set. One can also say that the tagging method does not produce any correlation, but the original event sample is biased, so that as a net effect some correlation could appear.

To estimate the effect one has to go back to the Monte-Carlo simulation to get the number of hadronic events lost and the probability of getting tags in them. Unfortunately one can not extract this information directly from the data, because the 'lost' annihilation events are covered by background from $\gamma\gamma$ and beam-gas processes. An additional Monte-Carlo set was generated, containing only these annihilation events which did not pass the offline selection criteria. The QCDFF model was used for this purpose. The generated events were analysed in a normal way to find the vertices. The estimated number of events in $\cos\theta < 0.7$ range lost by the selection was 4000 ± 300. These would contain 12 ± 6 single tags and less than 0.1 double tag. Inserting these new values into the double tag formula with simultaneous change of the f's to the quark model values one obtains $P = 64 \pm 8\%$.

There was one more mechanism considered – this was the effect of the error in the interaction point location. A shift in the IP position could result in enlarging the probability of tag. However the geometrical cut on the vertex position allowed at best one jet in an event to profit from this mechanism, thus the net effect here would be a negative correlation between the tag probabilities, resulting in underestimation of the purity. The effect was studied by shifting the IP position in the Monte-Carlo and was found to be small.

Finally one has to consider the effects of the errors on the assumed values of f's and a. Changing these values in the range allowed by the models produced a change in the estimated purity of $^{+2}_{-4}\%$. It is worth noting that the result is very stable with respect to the assumed value of the c over light quark tag probability ratio a. Changing a in the range from 0 to $+\infty$ caused the calculated p_b to change by less then 3% (relative). These errors were added in quadrature, together with the uncertainties from the previous corrections to give a total systematic error of $^{+3}_{-5}\%$.

The value of the purity of the sample selected with cuts $S > 5.5$, $\varepsilon < 23^\circ$ and $Q > -1$ was therefore found to be

$$P = 64 \pm 8\,^{+3}_{-5}\%$$

which for 806 tags accepted (with containment cut $\cos\theta < 0.75$) means that there were 520 ± 80 b jets in the tagged sample. These values were used in subsequent physics analysis.

4.6.3 Cross-checks

To ensure that the double tagging method indeed gives a reliable estimate of the b content of the tagged sample, some checks were performed.

The first check applied was a comparison between the high-p_T lepton tagging method an the present one.

As the presence of a semileptonic B decay in the jet could change the probability of finding a vertex, the leptons were searched only in jets opposite to the tag.

The first check was performed using the muons found according to the procedure given in [48]. The signal muon was required to have the longitudinal momentum $p_l^\mu > 2\,\mathrm{GeV}/c$, and transverse momentum $p_T^\mu > 0.6\,\mathrm{GeV}/c$, both calculated with respect to the event sphericity axis. In this region 672 good muon candidates were found in all the 1986 data. This means that in a random sample of 806 jets one would expect to find 8.6 muons in the signal region. Reference [48] gives a table listing the various contributions to the muon yield in the signal region. Using this table it was estimated that if the quark content of the sample was as calculated in the previous section, one should find 19 muons in the tagged jets; 13 of them would come from b decay (either directly, or via an intermediate charm state), one from primary charm decay, the rest would be background from punch through hadrons or from π and K decays. 22 muons were found in the tagged jets, thus confirming the enrichment.

An attempt was also made to use electrons to check the b tagging. The electrons were selected using the barrel liquid argon calorimeters, according to the procedure described in [49] and [50]. The signal region was defined as $p^e_l > 2\,\mathrm{GeV}/c$, $p_T^e > 1\,\mathrm{GeV}/c$, again the p_T was calculated with respect to the event sphericity axis. Using the plots given in [49] it was estimated that 1.2 such electrons should be found in the random sample of 806 jets, as opposed to 4.3 electrons in the enriched sample. In the tagged jets 3 such electrons were seen. The result is thus consistent with expectation, however it lacks statistical significance.

The results of lepton search suggest that the sample is not dominated by light quark jets. They could not, however, completely exclude the hypothesis that the charm content of the tagged sample is much higher than anticipated. To check for this possibility charm search was performed in the tagged jets. The decay $D^{*\pm} \rightarrow D^0\pi^{\pm}$ was used as a charm tag. The D^* candidates were searched using the method described in [38]. 105 good D^* candidates with $x > 0.5$ were found in the 1986 data. In [38] it was estimated that those good candidates contain 20% background and up to 4% contribution from $b \rightarrow c$ decays, the rest comes from primary charm quarks. One therefore expects to find in the tagged jets 1.2 D^* candidates (0.3 from background, 0.3 from $b \rightarrow c$ transitions and 0.6 from primary c quarks). In the data no D^* candidate was found opposite to the tag. This result can be converted into a weak limit of less than 500 charm jets among the tagged ones at 90% confidence level. Again the result is consistent with the enrichment expected, but the statistical significance is poor.

4.7 Summary of the Tagging Method

A new technique for tagging the b production events has been developed. It is based on reconstruction of the B hadron decay vertex. The method is general in nature, and can be applied at any detector with sufficient tracking precision.

The method has been applied to the data collected by the TASSO detector at 35 GeV e^+e^- center-of-mass energy. For a particular set of cuts: vertex separation $S > 5.5$, vertex direction $\epsilon < 23°$, vertex quality $Q > -1$ and sphericity containment $|\cos\theta| < 0.75$ it yielded

$$n = 806$$

tagged jets in 30520 events. The b content of this sample was estimated from the rate of doubly tagged events in the data to

$$P = 64 \pm 8^{+3}_{-5}$$

The background contains, according to the Monte-Carlo studies, $54 \pm 10\%$ of charm jets, the rest are the light quark ones. The efficiency of the method, defined as a probability that a $b\bar{b}$ event will get a tag was with these cuts estimated to

$$\epsilon = 0.16 \pm 0.03$$

It is, of course, possible to apply a different set of cuts, to obtain samples of different purity and statistics.

The important feature of the vertex b tagging method is that its efficiency and reliability quickly grow with improving precision of track reconstruction, but only weakly depend on the energy of the decaying B hadron (this because at higher energies the decay length increases, but the opening angle of the products decreases causing higher error on the decay length measurement). The lifetime tagging of heavy flavours will therefore be a very powerful technique at the experiments at SLC, LEP or HERA, equipped with a new generation of high precision vertex detectors.

Chapter 5

Applications of b Tagging

This chapter presents a few examples of applications of the b tagging technique described in the previous chapter for studying the b quark physics. The first study made was a comparison between the b quark initiated and average jet properties. The results of these measurements were used to test one of the latest versions of the LUND model in its b sector (up till now this model has been tested only on 'average' events, without flavour separation). For the purpose of this measurement the jets opposite to the b tag (further called 'tagged jets') were used. The tag was defined by the cuts described in the previous chapter.

The second application was a measurement of the forward-backward asymmetry in $b\bar{b}$ production. The standard model predicts the existence of such asymmetry as a consequence of an interference between the electromagnetic and weak neutral current interactions. This measurement can bring information about the electroweak interactions of the b quark.

5.1 Properties of b jets

The first application of the b enrichment method was a look at the general properties of b jets. Some studies of the general properties of b events at high energies have been done before [10,11]. The other studies used however smaller b samples, therefore having larger statistical errors. The goal of the analysis was to measure differences between the b enriched and average jets in the distributions of simple kinematical variables. As already explained, one expects to see some difference as a simple consequence of the B decay kinematics. It is however interesting to check if all the differences can be explained by that effect only, without calling for any new or special form of the b quark interaction. To check for this the results were compared against a Monte-Carlo model (LUND version 6.3 [32]). The parameters of this model have been tuned before to reproduce the characteristics of an average annihilation event [36], it was thus checked if the model which has not been specially tuned to reproduce the b event characteristics, can predict the properties of the b enriched sample.

It was decided to use the MILL tracks in this analysis, because MILL is the standard track reconstruction program used in most TASSO studies of this type. The results can thus be better compared to the other TASSO data. Also the Monte-Carlo simulation program was optimised to give best agreement with the data when the MILL tracks were considered. This was an important point, as the simulation results were intensively used throughout the analysis. The high tracking precision of the vertex detector was on the other hand not required. One problem to cope with when using the MILL tracks is that some of them have an unphysically high momentum assignment. These tracks could strongly bias the distributions studied, mainly by pulling the event sphericity axis towards themselves. To overcome this problem all the tracks with momentum $p > 1.5\,E_{BEAM}$ had their momentum rescaled to $1.5\,E_{BEAM}$. Even through still unphysical, this momentum assignment allows to avoid strong biases in the sphericity distribution, and the analysis remains compatible with other similar analyses done usually without such rescaling.

For the purpose of this analysis an event was divided into two hemispheres by a plane perpendicular to the sphericity axis and a jet was defined as a collection of tracks belonging to one hemisphere. Only the jets opposite to the b tag (tagged jets) were used. As both jets fragment to some extend independently and the B hadrons on both sides decay in an independent way, these jets are 'unbiased' by the tagging method, i.e. they represent an average b jet sample. The jet constituting a tag is on the other hand strongly biased by the requirement of passing all the vertex reconstruction cuts. Also, for similar reasons, no properties of the whole events have been examined - these would by biased by the jet constituting a tag.

The b enriched jet has to be compared with an average one. The definition of an average jet requires however some care. One can not just average over all the jets in all the hadronic events as these are biased by the hadronic selection criteria. The problem here is similar to the one encountered during the measurement of the purity of the tagged sample – the cuts applied by the vertex reconstruction procedure are not orthogonal to these used for selection of the annihilation events, therefore the result of applying the hadronic selection and tagging is different then the result of the selection alone. To overcome, at least partially, this problem a concept of pseudo-tag was introduced. The pseudo-tag is a jet which has kinematical properties similar to the tag, but is not required to have a vertex fitted. The exact definition was:

1. The angle between the sphericity axis an the beam direction had to fulfil $|\cos\theta| < 0.75$
2. the jet had to have at least 3 tracks within 55° of the sphericity axis passing the first stage selection (section 4.3) with momentum $p > 0.6\,\mathrm{GeV/c}$.

The jets opposite to the pseudo-tags were used as an average jet sample.

All the distributions used in the analysis were corrected for the detector acceptance and electromagnetic radiative effects. In order to find the corrections an additional Monte-Carlo sample was generated using the LUND program version 6.3 without radiative corrections and without passing the particles through detector simulation. All the other program options were identical to those used in generation of the LUND63 events with full detector simulation. Particles with lifetimes shorter than $3 \times 10^{-10}\,\mathrm{s}$ (including the K^0_S and Λ^0) were decayed, all those with longer lifetimes were assumed stable. Event sphericity was calculated using all the charged products, and particles were assigned to jets in the above described way. The distributions of the quantity in question obtained from all the jets in the 'no-detector' sample and the pseudo-tagged jets from the sample with detector simulation were then divided bin-by-bin, yielding the distribution of the 'correction factor', which was then applied to the data. It was assumed that the correction was identical for the pseudo-tagged (average) and tagged (b enriched) jets. On the Monte-Carlo level it was always checked that the correction factors for the pseudo-tagged jets were flavour independent.

Figures 5.1–5.6 show the distributions of the track-related quantities: scaled momentum $x = p/E_{BEAM}$, rapidity $\eta = \frac{1}{2}\ln\frac{E+p_\parallel}{E-p_\parallel}$, transverse momentum p_T and the momentum component out of the event plane p_T^{out}. The event axis and the event plane were defined by the

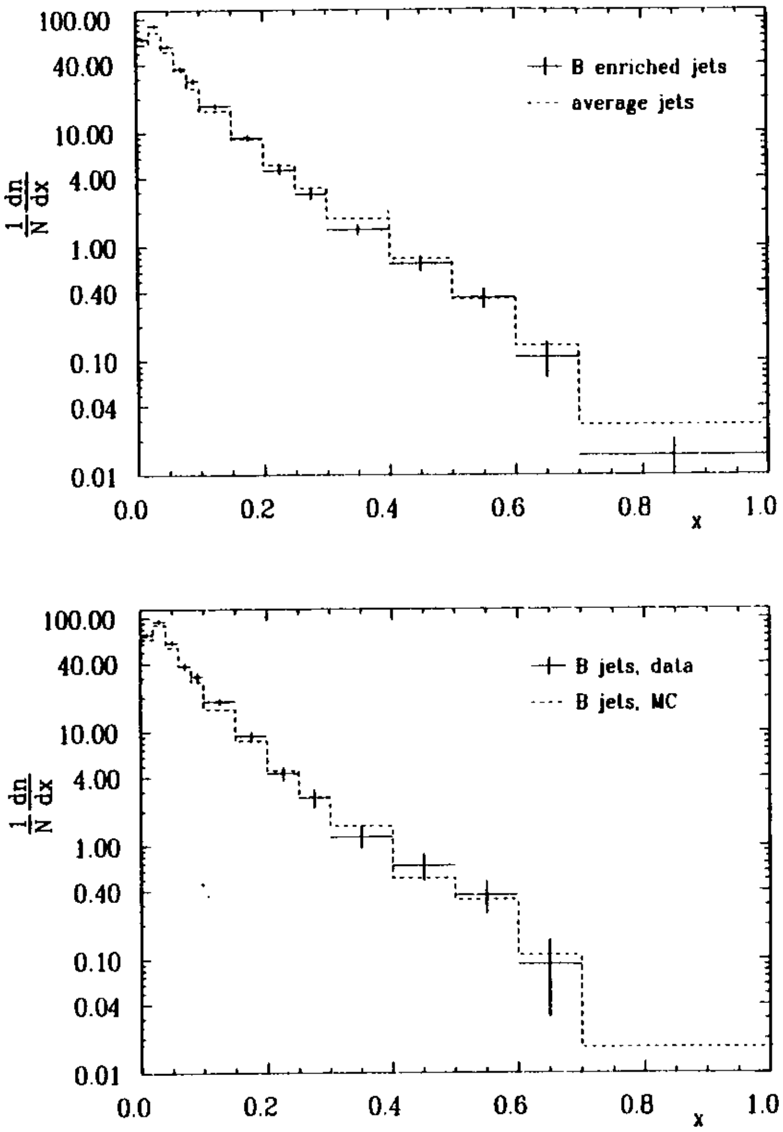

Figure 5.1: Distribution of track $x = p/E_{BEAM}$. Upper plot compares the average and b-tagged jets, the lower compares the background subtracted distribution to the prediction of LUND model (version 6.3). All distributions normalized to the number of jets N. The errors shown are statistical only.

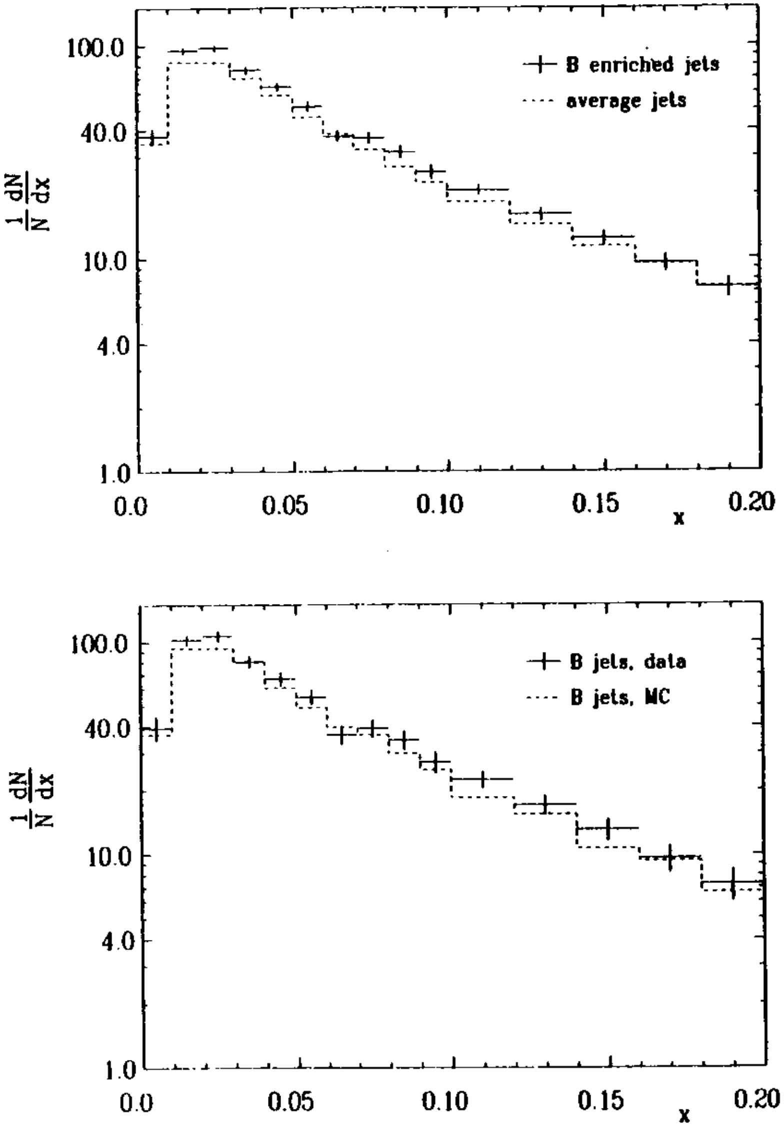

Figure 5.2: Detailed view of the low-x region of figure 5.1.

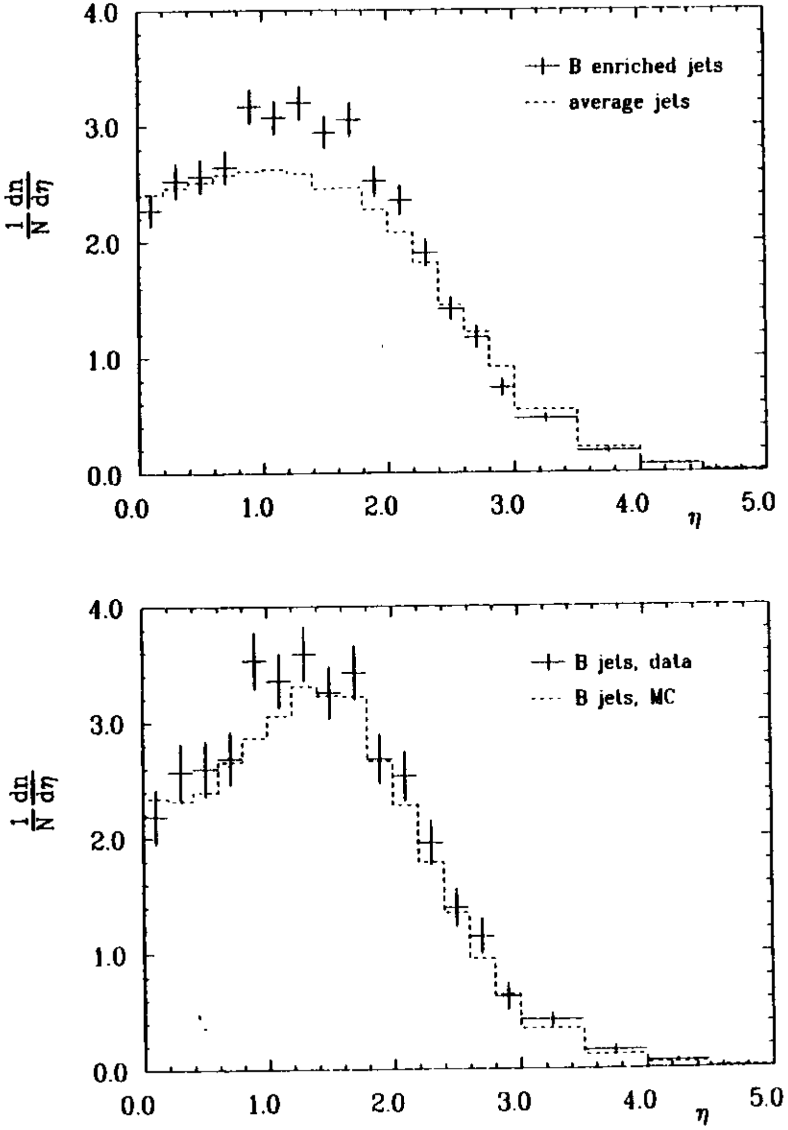

Figure 5.3: Track rapidity distributions. As fig. 5.1.

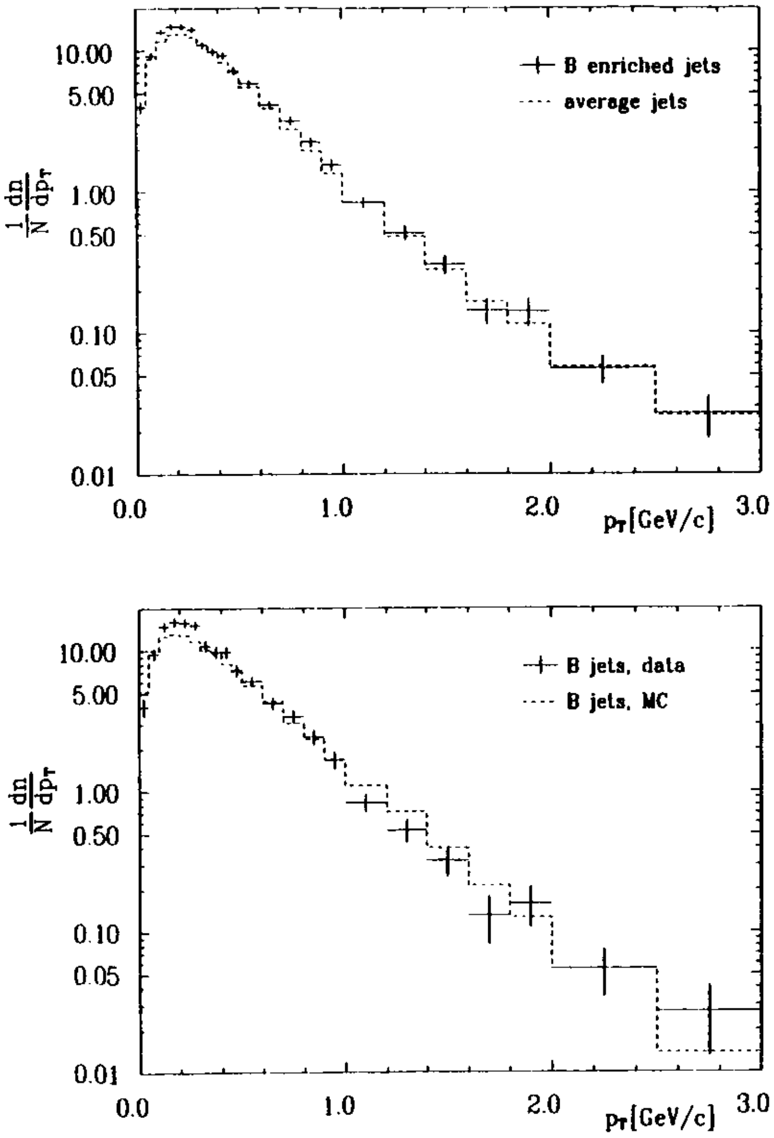

Figure 5.4: Distributions of track transverse momentum with respect to the event sphericity axis. As fig. 5.1.

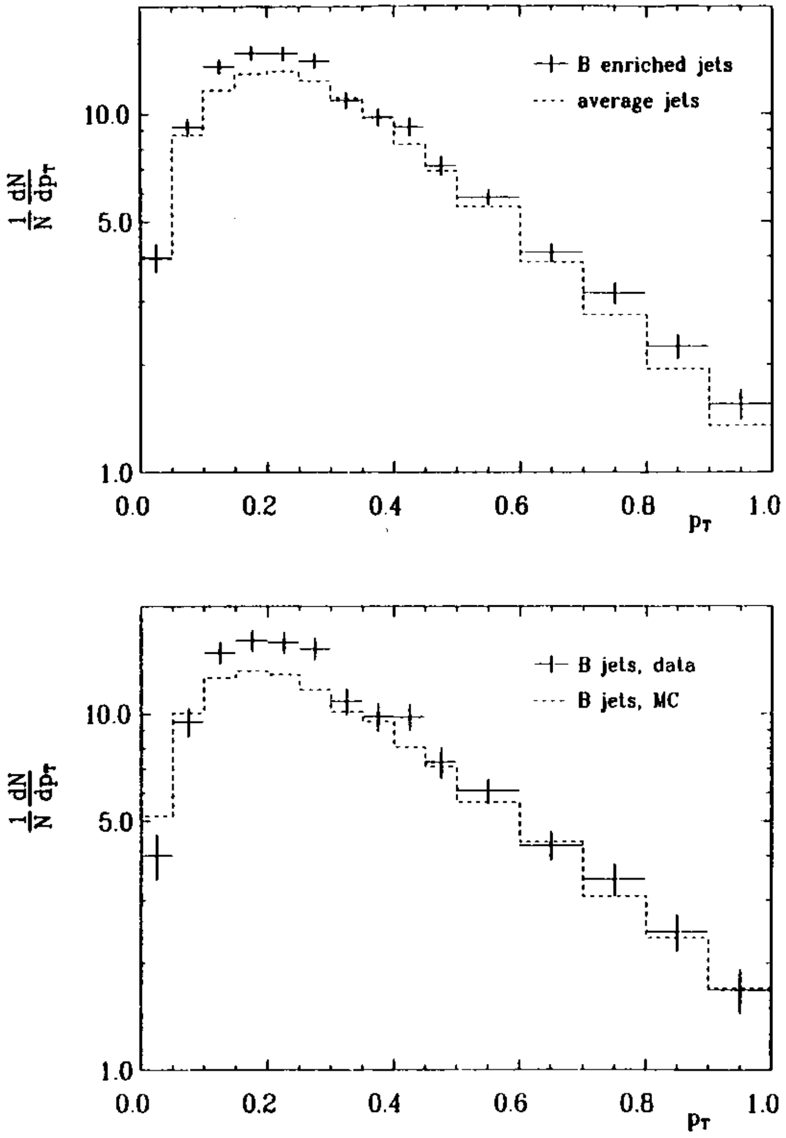

Figure 5.5: Enlarged view of the low-p_T region of fig. 5.4.

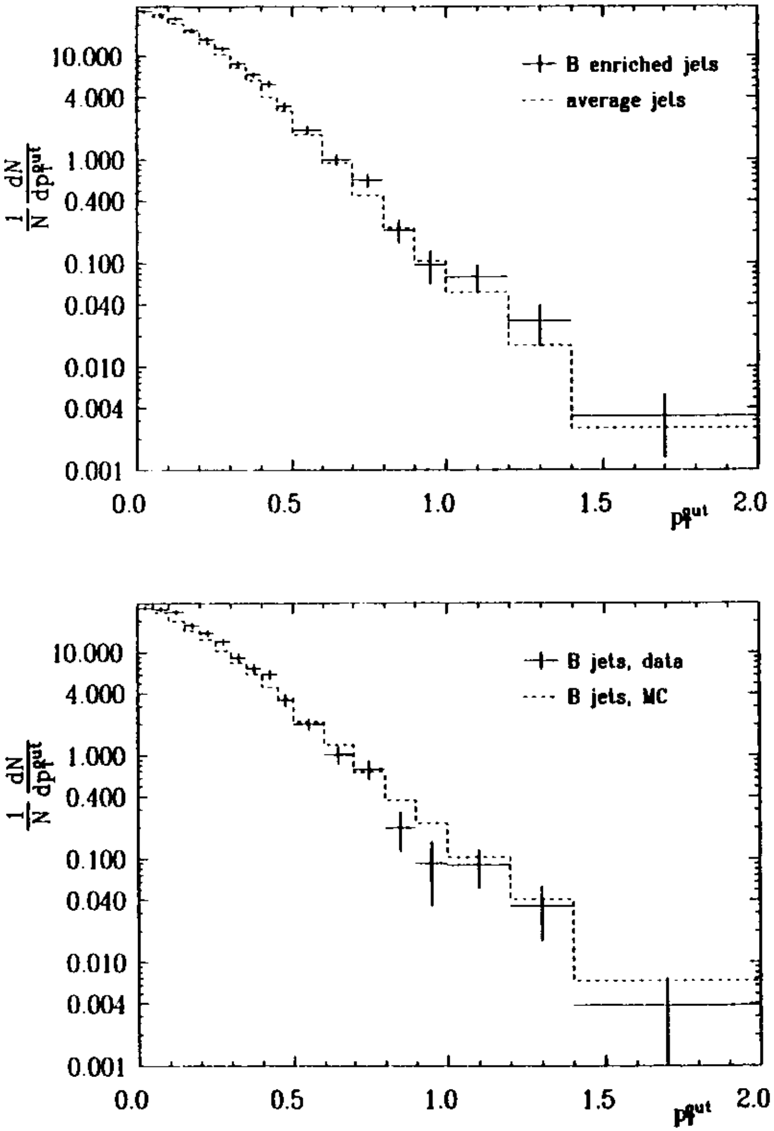

Figure 5.6: Distribution of the track momentum component perpendicular to the event plane. As fig. 5.1.

sphericity tensor, calculated from all charged tracks in the event. All the quantities have been calculated with respect to these axes. For the purpose of computing the rapidity, pion masses were assumed for all the tracks. In each of the figures the upper plot shows the b enriched jets compared to the average ones, the lower one shows the comparison of the 'pure b' jets (i.e. the b enriched jets with non-b background subtracted) compared with the prediction of the LUND model. The background subtraction was done bin-by-bin by subtracting the appropriately weighted average jet distribution from the tagged b one. This procedure contained an implicit assumption that the non-b background in the tagged jets had the same properties as the average jet. The potential source of differences was here the different quark content of the background in the tagged sample, the ratio between c and lighter species differs in the tagged and average events. This however is not expected to produce a significant bias, as charm jets have been seen to have very similar properties to the average ones [38]. All the plots were normalized to the number of jets used - the apparent differences in normalization come from different track multiplicities in a jet.

The most prominent differences between the b enriched and average jets can be seen in the rapidity and transverse momentum distributions. The rapidity plot shows an excess of tracks in the medium-rapidity region in the b enriched jets. This is well accounted for by the Monte-Carlo, which suggests that it is a simple kinematical effect. A hard b quark fragmentation results in production of a fast B hadron. The high multiplicity decay of this hadron produces particles mainly in the rapidity range of 1 to 2 units.

In the track p_T distribution the main difference appears in the low p_T region ($p_T \sim$ 0.2 GeV/c). A less significant excess of tracks appears in the b enriched jets at medium transverse momenta, around 1 GeV/c. It is interesting to note that no difference between b and average jets appears at higher values of transverse momentum. The naïve expectation would be that the excess tracks in b jets should, as the products of a heavy particle decay, appear up to the maximum momentum values allowed by the kinematics (which in case of a B hadron decay lies around 2.5 GeV/c). A possible explanation is that at the PETRA energies QCD production of additional jets can produce a similar number of high-p_T particles in lighter quark events as the B decay. In b events fewer such additional high-p_T jets are present, as most of the energy available is taken by the hard fragmentation of the heavy quark.

The differences in the two remaining variables (x and p_T^{out}) are less significant. The x plot shows some deficit of high-x tracks and clear excess at low x in b jets - this is an expected effect as in b jets the high-x leading particle (B hadron) decays, leaving the decay products at lower x. The p_T^{out} plot shows that b jets have somewhat more tracks sticking out of the event plane - in connection with the p_T plot this shows that average jets are more oblate than the b jets (the high-p_T tracks in an average jet tend to lie in the event plane, while those in a b jet are distributed more evenly around the jet axis).

The comparison with the Monte-Carlo model shows generally a good agreement, apart from the overall normalization (this suggests that the average track multiplicity of a b jet was not correctly predicted) and the low-p_T region, where the LUND model clearly had some problems.

In order to further investigate these differences between the data and the LUND model, the distributions of the jet multiplicity were made (see fig. 5.7). As in the previous figures, the pictures show the comparison between the average and b enriched jets (upper) and the comparison between the background subtracted b jets in the data and the LUND Monte-Carlo. One can see that the model indeed predicts too low a multiplicity of b jets. The

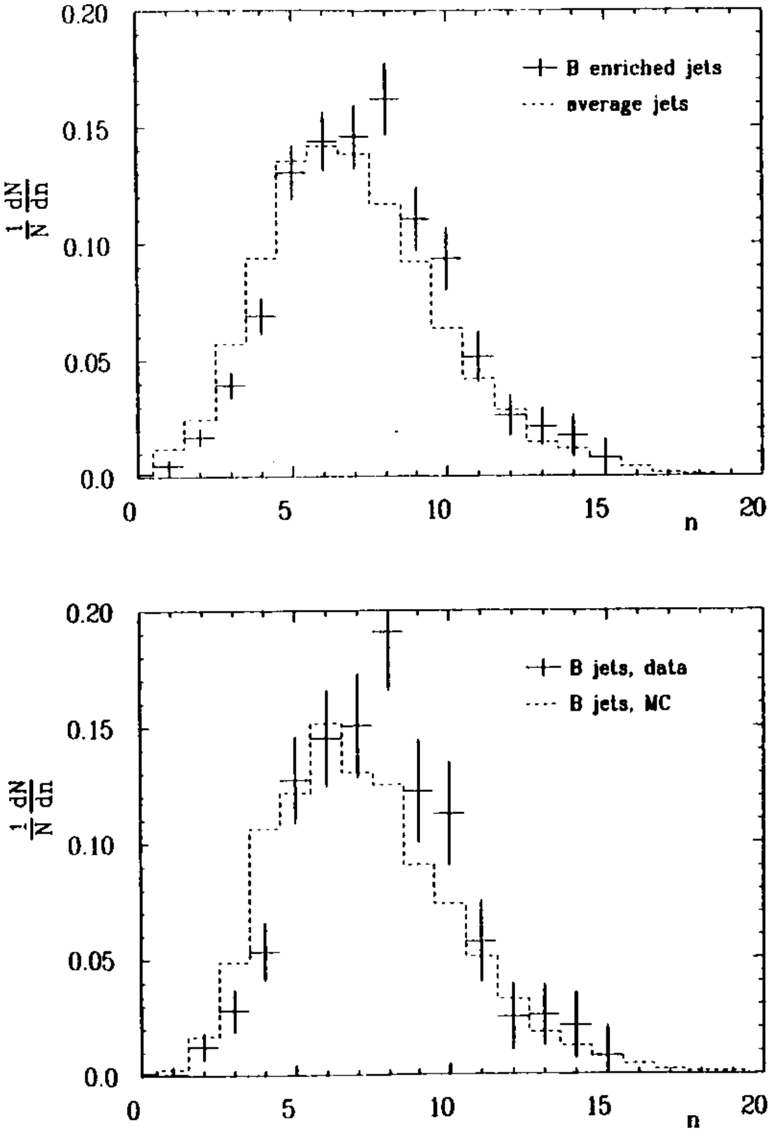

Figure 5.7: Distributions of charged multiplicity of a jet. As fig. 5.1.

averages found from these plots were

$$\begin{array}{lcll} \langle n \rangle & = & 6.98 \pm 0.02 & \text{data – average jets} \\ \langle n \rangle & = & 7.67 \pm 0.16 & \text{data – } b \text{ jets (background subtracted)} \\ \langle n \rangle & = & 7.24 \pm 0.04 & \text{LUND – } b \text{ jets.} \end{array}$$

The errors are statistical only. A word of warning is needed here: The numbers given above have been corrected using the same procedure as was used for all the other variables. In the case of a multiplicity measurement this is however an oversimplification - the multiplicity distribution has quite special properties, as it is directly affected by the trackfinding efficiency, which causes migration of events between different bins of the distribution, where the amount of migration depends on the multiplicity itself (as in dense jets the tracking efficiency is lower). The right correction procedure should therefore unfold the true distribution using the 'correction matrix' (see e.g. [26]). The procedure used would be correct only in case that the model were an ideal description of the data, which is not the case. Therefore the above numbers can have big systematic errors - the intention of citing them was solely to demonstrate the differences among them. To get some idea about the size of the systematic errors coming from this source: the average charged multiplicity of an average jet obtained by applying the unfolding procedure to the same data was [51]

$$\langle n \rangle = 7.51 \pm 0.01 \pm 0.2.$$

From the numbers given above it can be seen that the LUND model underestimates the b jet charged multiplicity by on average about 0.4 prongs per jet. In search for a possible source of this effect, the average multiplicity of a B hadron decay was checked. CLEO has measured the average decay multiplicity of the (unseparated) mixture of B_d and B_u mesons to be $5.5 \pm 0.03 \pm 0.015$ [52]. The measured average charged multiplicity of B_d and B_u meson decays in the LUND model (on the generator level) was found to be only 5.11. It is concluded that the difference in multiplicity can be easily accounted for by this deviation. The fact that the missing tracks appear mainly at low p_T could indicate that the real problem may lie in the decay of charmed hadrons created in the B hadron decay, because the secondary charm decay tracks are expected to appear at lower transverse momenta. It was however not possible to draw more firm conclusions on this topic on the basis of available data.

In addition to the track-related distributions, some jet-related quantities were also studied. Analogous plots were made for the jet sphericity S, jet thrust T, jet aplanarity A and the 'jet transverse thrust' $T_T = \sum |p_T^{out}| / \sum E$. The last variable is related to the 'jet transverse mass' and the 'transverse thrust', both used by JADE [46,53] for the purpose of flavour separation. The main difference was that here only charged particle information was used. All the quantities above were defined as usual and calculated from tracks belonging to one jet only - except that the *out* axis of the event for transverse thrust calculation was found using the sphericity tensor of the whole event. The results are shown in figs. 5.8 - 5.11. An unexpected feature is a rapid jump in the thrust distributions for the b enriched jets (around $T = 0.85$). This effect was neither expected, nor seen by others. It was carefully searched for possible biases or errors which could produce such effect - none were found. It is therefore most probably just a statistical fluctuation.

The differences seen between the b enriched and average jets in the sphericity and thrust distributions are not very significant - in the sphericity plot the b enriched jets are seen to have slightly higher average sphericities than the average jets. As both the quantities

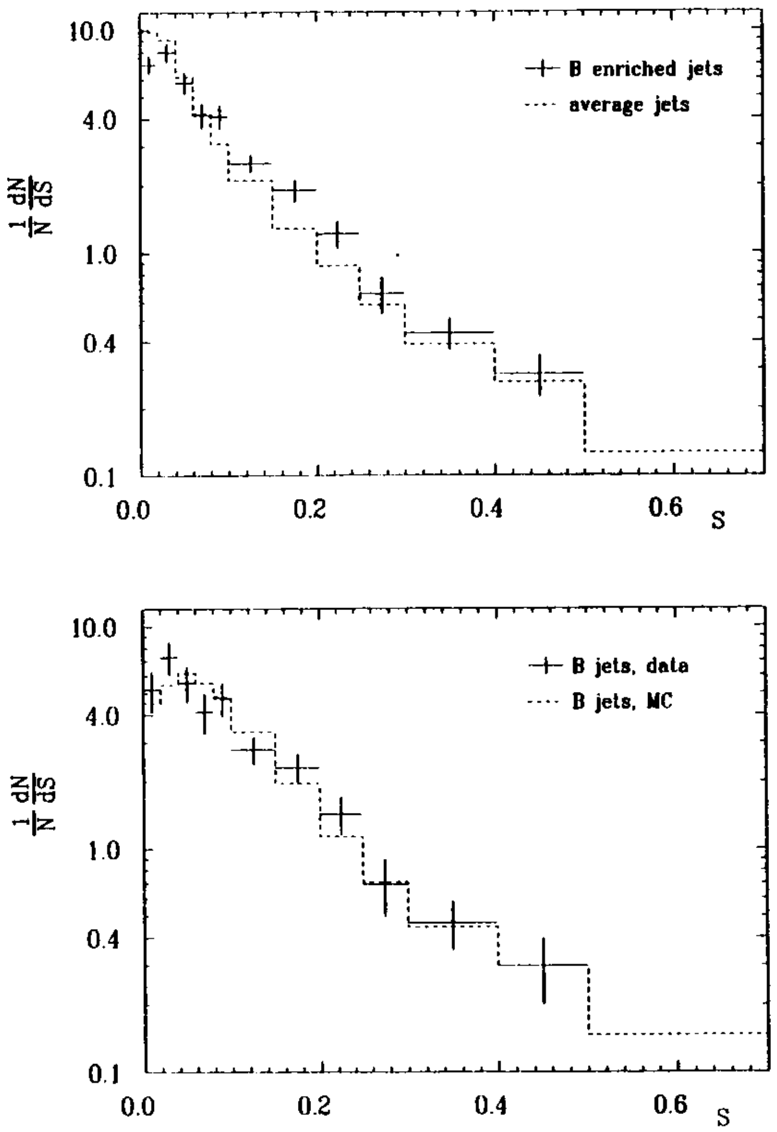

Figure 5.8: Distribution the jet sphericity. As fig. 5.1.

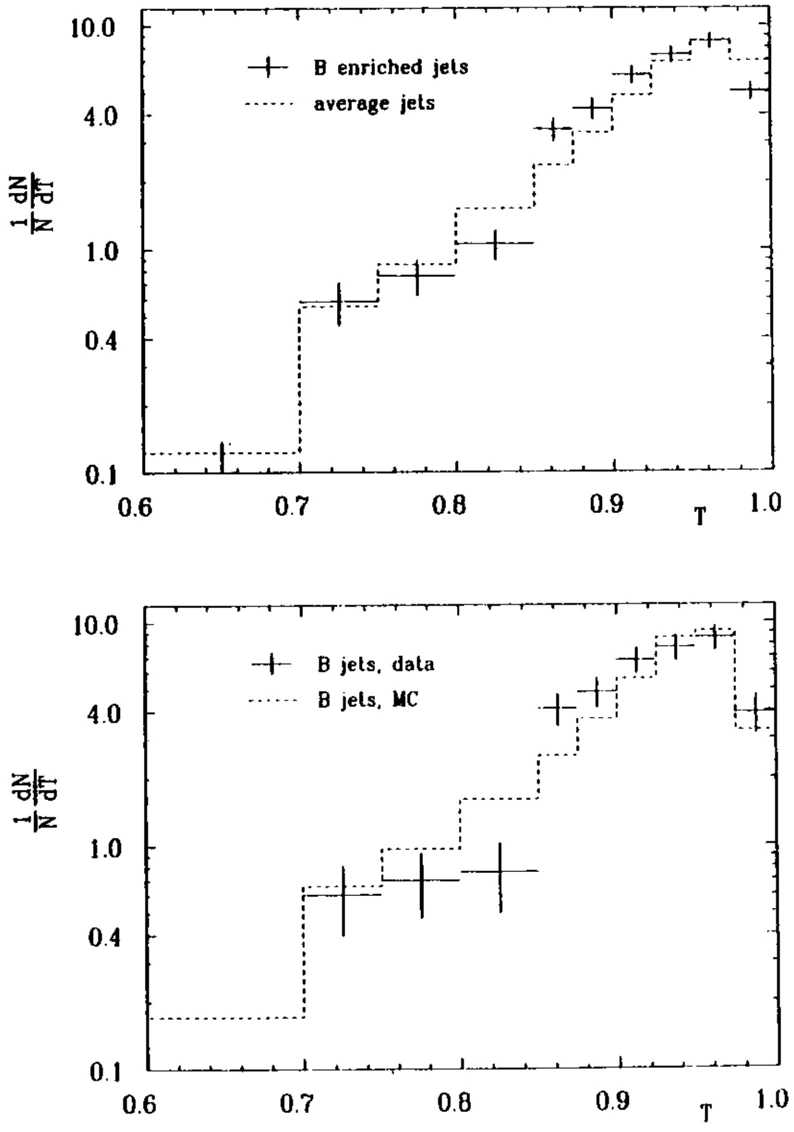

Figure 5.9: Distributions of the jet thrust. As fig. 5.1.

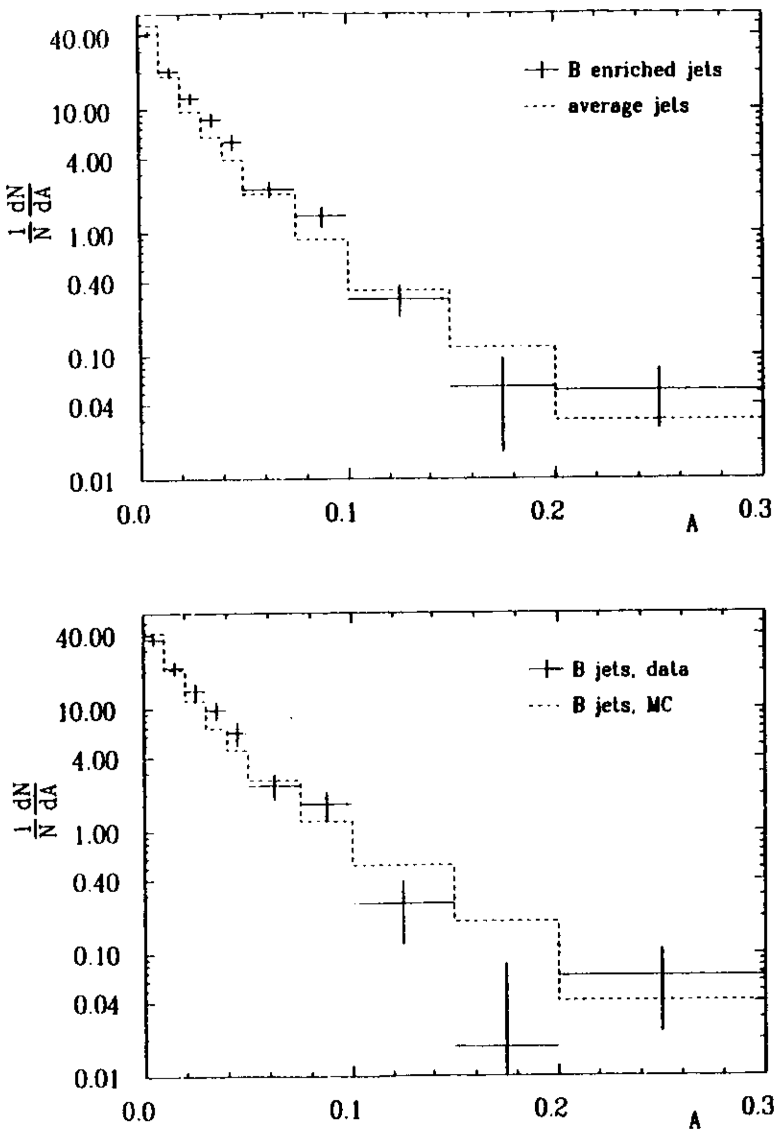

Figure 5.10: Distributions the jet aplanarity $A = \frac{1.5 x_1}{(x_1+x_2+x_3)}$, x_1, x_2 and x_3 are the eigenvalues of the sphericity tensor in ascending order. As fig. 5.1

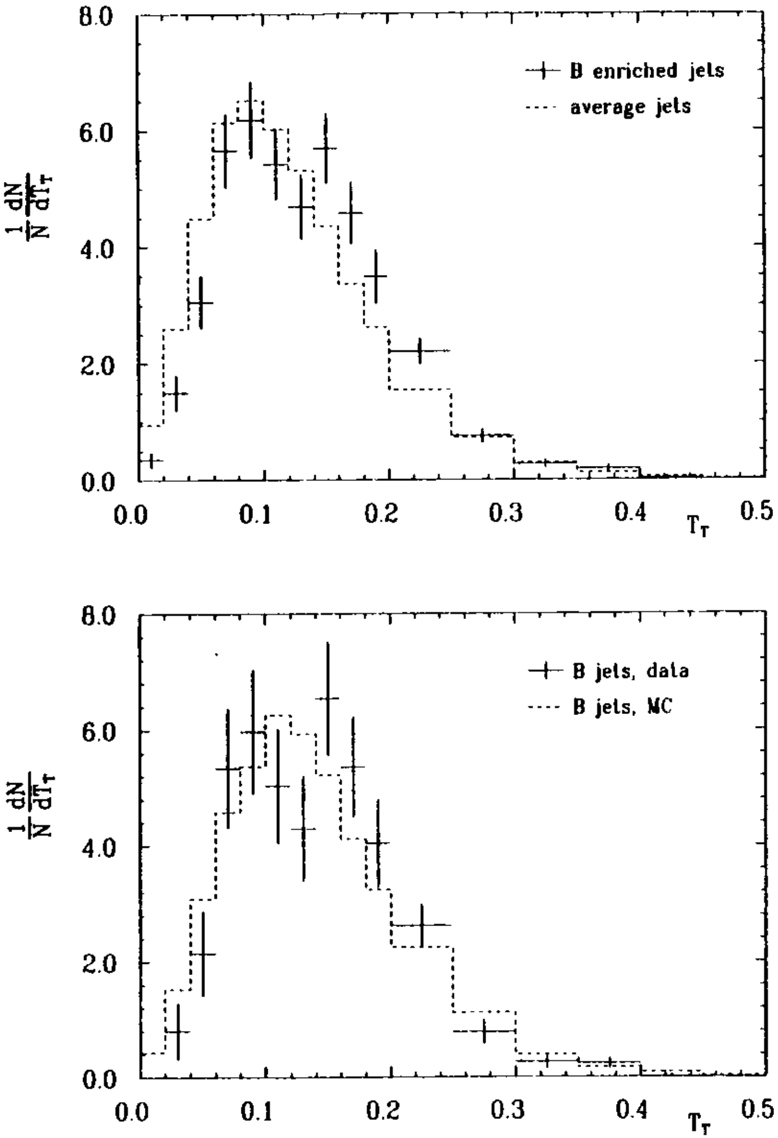

Figure 5.11: Distribution of the jet transverse thrust $T_T = \frac{\sum |p_T^{out}|}{\sum E}$, p_T^{out} is the momentum component along the shortest axis of the event sphericity tensor. As fig. 5.1.

measure the deviation of a jet from a linear structure, one may conclude that the width of the b enriched jets is similar to that of the average jets. This supports the conclusion drawn from the track transverse momentum plot that at the PETRA energies the production of additional jets can produce a jet broadening effect as strong as the B decay.

The other two variables plotted, A and T_T both measure the amount of momentum flowing out of the jet (resp. event) plane, and thus the deviation of a jet from a planar structure. If the hemisphere analysed contained in reality two high energy jets, one would get a high sphericity and thrust values, but still low aplanarity. Both plots show that b jets are less planar than average ones, this supports the observation made already when studying the p_T and p_T^{out} distributions. In none of the distributions any significant deviation from the model predictions could be seen. Certain small differences between the data and Monte-Carlo were nevertheless observed. One has however to be careful when drawing any conclusions, as in the case of the jet-related quantities some dependence of the correction factors on the flavour of the initiating quark could be observed. This suggests that the systematic errors on the corrected b distributions might be sizeable.

Summary

A comparison was made between the properties of the b enriched and average jets. Differences between them were noted, and compared to the predictions of the LUND model - version 6.3. The model was shown to give generally correct predictions about the b jet properties. The main discrepancy was found to be wrong charged track multiplicity - this could be traced back to the wrong multiplicity of B hadron decays as predicted by the LUND model version used here.

5.2 Forward-Backward Asymmetry in the b Quark Production

5.2.1 The Standard Model and Asymmetries

The last analysis done using the tagged b sample was a measurement of the electroweak induced asymmetry in the b quark production. In the standard model the asymmetry appears as a result of an interference between the γ and Z^0 exchange diagrams (fig. 1.1). The differential cross section for the production of a fermion-antifermion pair in the e^+e^- annihilation can in the lowest order be expressed as:

$$\begin{aligned}\frac{d\sigma_{ff}}{d\cos\theta} = \frac{\pi\alpha^2}{2s}\Big[&\left(Q_f^2 - 2Q_f v_e v_f \mathrm{Re}(\chi) + (v_e^2 + a_e^2)(v_f^2 + a_f^2)|\chi|^2\right)\left(1 + \cos^2\theta\right)\\ &+ \left(-4Q_f a_e a_f \mathrm{Re}(\chi) + 8v_e v_f a_e a_f|\chi|^2\right)\cos\theta\Big]\end{aligned}$$

where Q_f is the fermion charge (in units of e), θ is the angle between the incoming electron and the outgoing fermion, and χ contains the CM energy squared s, the ratio of the neutral to charged current coupling strength ρ, the Fermi constant G_F and the Z^0 propagator:

$$\chi = \frac{\rho G_F m_Z^2}{8\pi\alpha\sqrt{2}}\frac{s}{(s - m_Z^2 + i m_Z\Gamma_Z)}.$$

The cross section for quark pair production must be in addition multiplied by a colour factor of 3. At the PETRA energies $s \ll m_Z^2$ - this allows to ignore the Z^0 width Γ_Z. The formula a may be then rewritten in the form

$$\frac{d\sigma_{ff}}{d\cos\theta} = \frac{\pi\alpha^2}{2s}\left[(C_1(1 + \cos^2\theta) + C_2\cos\theta\right]$$

with

$$\begin{aligned}C_1 &= Q_f^2 - 2Q_f v_e v_f \chi_1 + (v_e^2 + a_e^2)(v_f^2 + a_f^2)\chi_1^2\\ C_2 &= \qquad -4Q_f a_e a_f \chi_1 + 8v_e v_f a_e a_f \chi_1^2\end{aligned}$$

where χ_1 is obtained from χ by setting $\Gamma_Z = 0$. The cross-section is thus asymmetric in θ by appearance of the term $C_2\cos\theta$. Experimentally it is convenient to express the results in terms of the integrated asymmetry:

$$A_{ff} = \frac{N_F - N_B}{N_F + N_B}$$

where N_F and N_B are the numbers of fermions found in forward and backward hemispheres (with respect to the incoming electron). By integrating the cross section one can find

$$A_{ff} = \frac{3}{8}\cdot\frac{C_2}{C_1}.$$

For a case of the b quark the standard model predicts $a_b = -1$, $v_b = -1 + 4/3\sin^2\theta_W$. Putting in the measured values, $\sin^2\theta_W = 0.229$, $M_Z = 92\,\mathrm{GeV}/c^2$ [54], $\alpha^{-1} = 137.036$ and $G_F = 1.16637 \times 10^{-5}\,\mathrm{GeV}^{-2}$ one can calculate the theoretical asymmetry in the process $e^+e^- \to b\bar{b}$ at 35 GeV CM energy to

$$A_{b\bar{b}}^{theor} = -0.274$$

It should be noted, that this value was calculated using the physical values for $\sin^2\theta_W$ and M_Z - this means that the standard model relation between these parameters was not used (in fact the values used did not satisfy the lowest-order relation $M_Z^2 = \frac{\pi\alpha}{\sqrt{2}G_F\sin^2\theta_W\cos^2\theta_W}$). Some discussion about the rationale behind this procedure can be found in [55]. The standard model is thus seen to give a definite prediction for the asymmetry, the role of the experiment is now to check that prediction.

In the past several experiments at PEP at PETRA measured the quark asymmetries for c and b quarks. Two measurements have been also done on the flavour unseparated annihilation events [58,59]. A review of the existing quark asymmetry measurements can be found in [55]. The existing $A_{b\bar{b}}$ measurements, when combined, lead to the product of the coupling constants $a_e a_b = -0.97 \pm 0.22$, in agreement with the standard model. However all the methods used up till now for b asymmetry measurements relied both in the b selection and its charge reconstruction on leptons coming from the decay $b \to l^- X$. There exist two sources of wrong sign leptons in the b decay (apart from the experimental background): cascade decays $b \to c \to l^+ X$ and $B_0 - \bar{B}_0$ mixing which flips the b quark charge between its production and decay. The second effect is more difficult to experimentally correct for, as it depends on the mixing parameters (up till now measured with very wide error margins) and unknown fractions of different B hadron species produced in the b quark fragmentation.

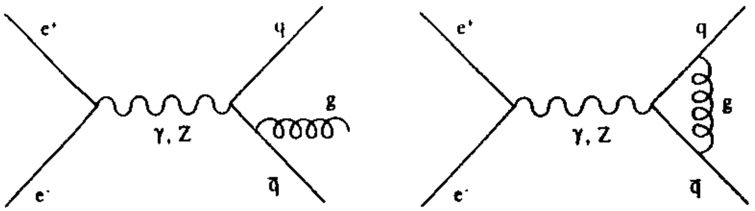

Figure 5.12: Diagrams contributing to the first order QCD correction to the asymmetry.

Most experiments have therefore only noted that their result depends on mixing, but did not attempt to actually make the correction. It is therefore interesting to measure $A_{b\bar{b}}$ using an alternative method of event selection and charge reconstruction, possibly less sensitive to the mixing phenomena.

Before comparing the prediction given above with the experimental results, a number of corrections has to be applied. First, the above formulae are correct only for a case of massless fermions. Outgoing fermions with finite mass have a velocity $\beta < 1$, and β enters differently into the vector and axial coupling terms in the interaction. The high mass of the b quark makes the correction non-negligible. For $\beta < 1$ C_1 and C_2 take the form

$$\begin{aligned} C_1 &= \beta\left[1 + \frac{1}{2}(1 - \beta^2)\right] \cdot \left[Q_f^2 - 2Q_f v_e v_f \chi_1 + (v_e^2 + a_e^2)v_f^2\chi_1^2\right] + \beta^3(v_e^2 + a_e^2)a_f^2\chi_1^2 \\ C_2 &= \beta^2(-4Q_f a_e a_f \chi_1 + 8v_e v_f a_e a_f \chi_1^2) \end{aligned}$$

Assuming the b quark mass of 5 GeV/c, a b quark created at 35 GeV/c CM energy has $\beta = 0.958$. This leads to the value

$$A_{b\bar{b}}^{theor} = -0.253$$

The second source of corrections are QCD radiative effects. They appear as a coupling of the final state quarks to gluons. These correction have been calculated in the first order by Jersák, Laermann and Zerwas [57] for diagrams shown in figure 5.12. It however happens that these corrections leave $A_{b\bar{b}}$ virtually unchanged - due to a fortunate cancellation of the corrections to C_1 and C_2. At other energies (or for lighter quarks) these corrections can however be more important (for example for the d quark asymmetry at the same energy the correction is -0.012). It is also important to note that inserting these corrections into the prediction forbids using any event-shape cuts (e.g. cuts against 3-jet events) in the analysis, as these have been already included in the calculation.

The last correction comes from the electroweak radiative effects. The main contributions come from the $O(\alpha^3)$ QED radiative processes of the type shown in the diagrams in fig. 1.2. To estimate the correction one needs however to take into account the detector acceptance, because the probability of accepting an event will generally depend on the energy and direction of the emitted photon. A common approach is to use the Monte-Carlo simulation to estimate this effect for a particular detector, and then to 'correct' the measured asymmetry (similarly to the corrections applied when measuring the b jet properties). This however led in the past to some confusion, as the experiments did not always state clearly how their radiative corrections were computed. Following the recommendation of Cashmore et al. [56] it was decided to quote the measured value uncorrected for any radiative effects, stating clearly the event acceptance criteria used. An attempt was made instead to estimate the correction to the predicted value using a Monte-Carlo simulation.

The LUND62 Monte-Carlo set, described in section 3.5, was used to find the corrections. The asymmetry was calculated using the b quark direction stored with the event fragmentation history. This was done once for events generated without electromagnetic radiative correction and once for events generated with radiative corrections, full detector simulation and event acceptance cuts. Only events with at least one vertex fitted were used, in order to get a more realistic simulation of the tagged sample. The observed relative difference in the b asymmetry was $-4 \pm 6\%$. This led to the prediction

$$A_{b\bar{b}}^{pred} = -0.242 \pm 0.015 \pm 0.015$$

where the first error is purely statistical in origin, coming from finite number of Monte-Carlo events available for calculation of the radiative correction and detector effects, and the second is a crude estimate of the "theoretical" error, coming from uncertainties in the standard model parameters and from neglecting the higher order corrections.

5.2.2 Quark Charge

For the measurement of an asymmetry in the $b\bar{b}$ production one needs some means of finding the direction of the primary b quark and for distinguishing quarks from antiquarks. The quark direction is usually well approximated by the sphericity axis, in fact this feature has been already used for the tagging (where the sphericity axis was used to approximate the B hadron direction, and this is usually close to the quark direction). More problem is how to distinguish quarks from antiquarks or, equivalently, how to measure the sign of the primary quark charge.

Those methods which use leptons to tag the b production get the charge determined 'for free' - the lepton created in the decay carries the charge of the primary b quark (neglecting the $b\bar{b}$ mixing for a moment). The vertex method of b tagging does not give such kind of information.

The method used is this work to determine the quark charge was based on an idea coming from Field and Feynmann [30] of using a "weighted charge" of a jet as a measure of the charge of the primary quark. They have defined the weighted charge of a jet as

$$q_{jet} = \sum_i Q_i z_i^\gamma$$

where the sum extends over the particles belonging to the jet. z_i denotes the fraction of the jet energy carried by i-th hadron, Q_i is a charge of this hadron and γ is some small positive constant, chosen so to give the best charge separation. The justification for this procedure comes from the observation that the fastest particles in a jet appear first in the fragmentation chain, and thus have the highest chance of carrying the primary quark. The meson which in the final state carries the primary quark can have only the same charge sign as the quark or be neutral - in the latter case the quark which goes next in the fragmentation chain gets the charge of the primary quark. This simple picture is somewhat complicated by decays of mesons created in the fragmentation, but still q_{jet} was shown by the authors of [30] to give the most reliable estimate of the primary quark charge in their simple Monte-Carlo model.

Experimentally the problem gets an additional complication arising from difficulties in defining a jet and measuring its energy. Therefore it is more common to use $x_i = p_i/E_{BEAM}$ in the jet charge formula, and define a jet as a collection of particles moving in the same direction with respect to some event axis.

The weighted charge method was used in different variations to establish the existence of charged partons in $e^+e^- \rightarrow$ jets [60] and to measure the charge asymmetry in $e^+e^- \rightarrow q\bar{q}$ without flavour separation [58,59].

In this analysis the method was to be used on the event sample strongly enriched in b quark jets. The original work of Field and Feynmann considered only the light quark jets, and the experimental studies done up till now used it at best on "average" jets, containing less than 10% b quarks. It is however clear that the weighted charge of a b quark jet will behave differently from that of lighter quark jets. In a b quark jet only the decay products of the hadron containing the primary quark are observable, these fall into lower x region, due to the high B decay multiplicity. Moreover, the b quark fragmentation function is much harder than the one for light quarks - therefore the particles produced later in the fragmentation chain behave differently from those in lighter quark jets. The method needed therefore an intensive reevaluation, before it could be used to tag the b quark charge.

The optimization of the method and the calculation of the probability of a correct primary quark charge assignment was performed using the Monte-Carlo technique. QCDFF35 and LUND63 sets (see section 3.5) were used. Jets were defined by dividing an event into two hemispheres by the plane perpendicular to the event sphericity axis and collecting the tracks in each hemisphere. The jet charge definition was

$$q_{jet} = \sum_i q_i \left(\frac{p_i}{E_{BEAM}} \right)^{\gamma}$$

where the sum is over all tracks belonging to the jet. For a given event the jet with higher q_{jet} was called "positive jet" - no cuts were applied at this point (in particular it was allowed that both jets had the same sign of q_{jet}, so that the positive jet could actually have negative charge). Figures 5.13 and 5.14 show the probability of getting the correct primary quark charge assignment (i.e. probability that a positive jet was initiated by a positively charged quark) as a function of the exponent γ, for average and b events respectively. Two sets of points on each picture are calculated from the two Monte-Carlo models. The errors attached to the points are statistical - due to largely overlapping samples used in calculating p^{guess} for each γ the points drawn for a given model are not statistically independent (the error bars should be understood as indicators of a confidence interval for p^{guess}).

The figures show that a b quark jet indeed behaves quite differently from an average one. In the average case best results are obtained using $\gamma \leq 0.5$ - in agreement with other studies of this type. In the b case, the optimum γ is however much higher - both models suggest that the maximum probability of recovering the jet charge is somewhere around $\gamma = 1$. Both models agree approximately in this point - they differ however somewhat in the absolute values of the guess probabilities, especially at low γ values. In the case of b jets the difference can be still consistent with the statistical errors, but in the plot for all jets it is significant. It is interesting to note that the sign of the difference is opposite for both plots - the Lund model predicts higher probability for the b jet, but lower for the average jet.

Similar plots were also made using the momentum component along the sphericity axis instead of total momentum in the jet charge formula. The results obtained were very similar, with slightly lower p^{guess} values.

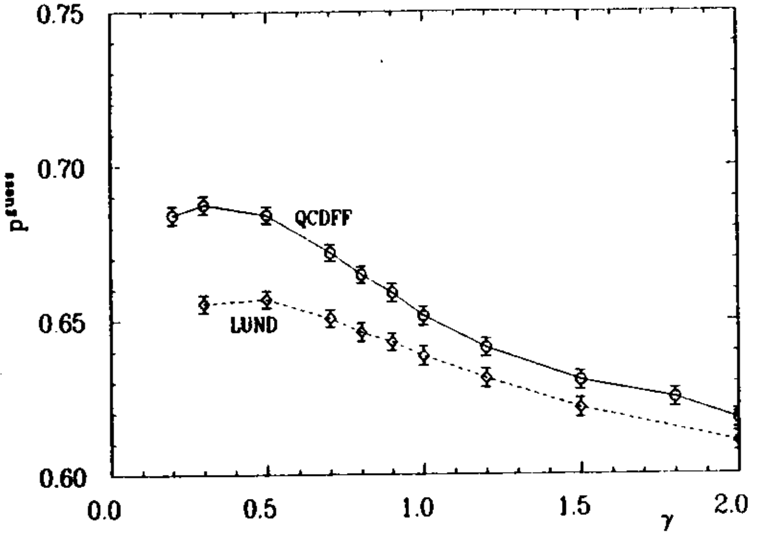

Figure 5.13: The probability of correct reconstruction of the primary quark charges in an average event as a function of the exponent γ used in the jet charge definition. The results of two Monte-Carlo models are shown.

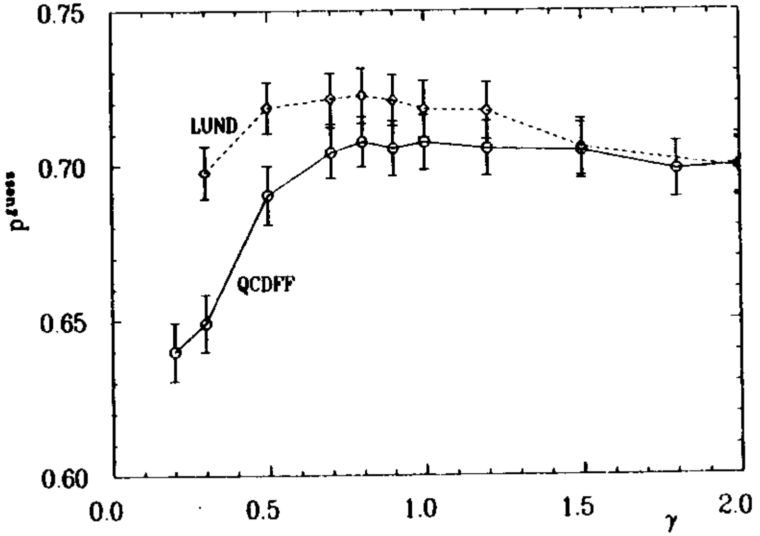

Figure 5.14: Same as fig. 5.13 but for b events only.

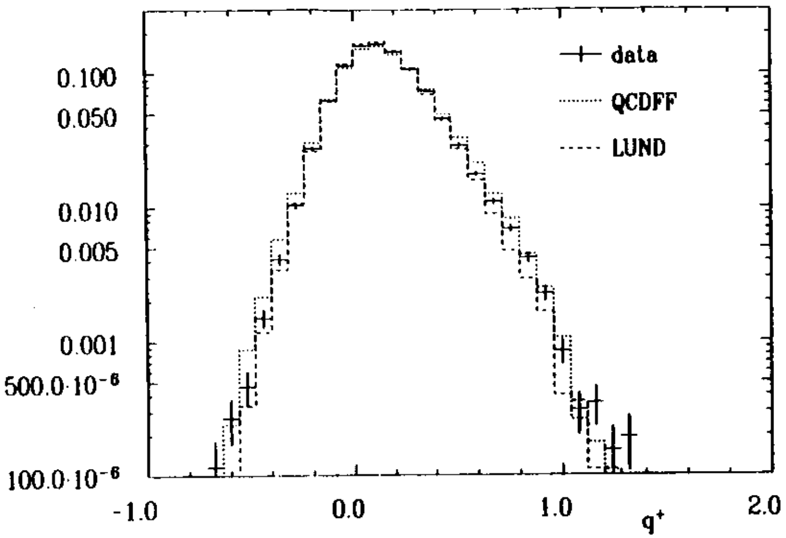

Figure 5.15: The distribution of the higher of two jet charges in an event. Data compared with predictions of two models. The jet charge was calculated with $\gamma = 1$.

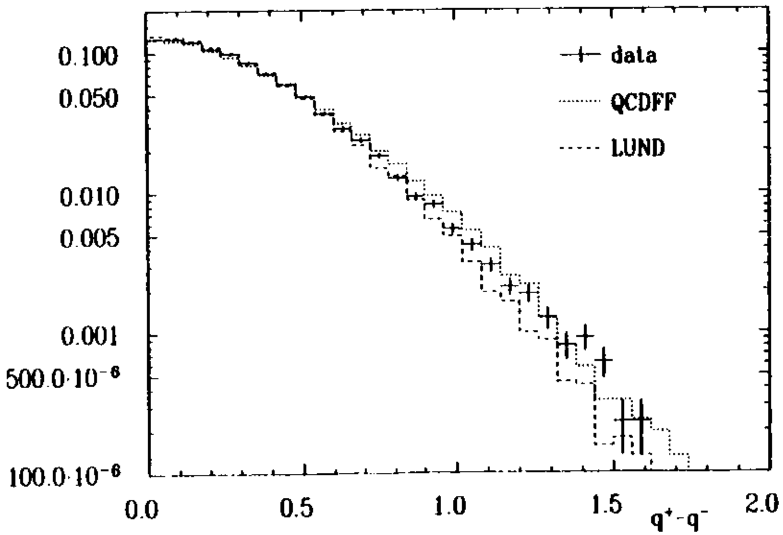

Figure 5.16: The distribution of the difference between the two jet charges in an event. Jet charges calculated with $\gamma = 1$.

In order to decide which of the two models offers a better description of the data a few directly comparable quantities were plotted in the data and compared with the predictions of both models. Two examples of such comparison are shown in figures 5.15 and 5.16. The quantities plotted are q^+, the higher of two jet charges in an event and $q^+ - q^-$, the difference between the two jet charges. The charges were calculated using $\gamma = 1$. The differences between the models are small, but significant. The data points do not clearly prefer any of the two models, staying rather between their predictions. The moments of the distributions as obtained from the data also lie in the middle between the two models – slightly closer to the QCDFF predictions. Also, at lower γ the quality of LUND prediction becomes gradually worse, the data compare better to the QCDFF plots. It was therefore decided to use the QCDFF model for calculating the efficiencies of the charge tagging and to use LUND for systematic error estimation. Table 5.1 shows the predictions for the probabilities of the correct charge guess given by the two models for various quark flavours.

Table 5.1: Probability of a correct quark charge guess for different primary flavours, as predicted by two Monte-Carlo models.

Quark	Model			
	QCDFF $\gamma = 0.5$	LUND 6.3 $\gamma = 0.5$	QCDFF $\gamma = 1$	LUND 6.3 $\gamma = 1$
u	0.7416 ± 0.0034	0.6817 ± 0.0037	0.7233 ± 0.0035	0.6749 ± 0.0037
d	0.6571 ± 0.0075	0.6087 ± 0.0078	0.6351 ± 0.0076	0.5991 ± 0.0078
s	0.6630 ± 0.0076	0.6110 ± 0.0078	0.6540 ± 0.0076	0.6072 ± 0.0078
c	0.6338 ± 0.0037	0.6445 ± 0.0037	0.5646 ± 0.0038	0.5989 ± 0.0038
b	0.6985 ± 0.0067	0.7157 ± 0.0055	0.7160 ± 0.0065	0.7162 ± 0.0067
average	0.6834 ± 0.0022	0.6587 ± 0.0022	0.6506 ± 0.0022	0.6383 ± 0.0023

In the context of the asymmetry measurement one has to consider the effect of a finite probability of charge reconstruction on the result. Assume that the probability of a correct charge guess is P. Assume further that one makes a distribution of the θ direction of the positively charged quark. Let n_1 be the true number of positively charged quarks falling into some θ bin. Due to charge misidentification only Pn_1 of them will be recognised as positive and found inside this bin, the rest will be classified as negative and the direction of the opposite jet will go into the plot. In exchange for this loss some negative jets will be taken as positive and found within the bin. If the true number of negative quarks were n_2 in the same bin, $(1 - P)n_2$ jets will be seen as positive. The number of jets classified as positive (negative) will thus be

$$n_+ = Pn_1 + (1 - P)n_2 \qquad n_- = (1 - P)n_1 + Pn_2$$

The measured charge asymmetry in this bin will be thus

$$A^{meas} = \frac{n_+ - n_-}{n_+ + n_-} = (2P - 1)\frac{n_1 - n_2}{n_1 + n_2} = (2P - 1)A^{true}$$

Where A^{true} is the true asymmetry. The measurement result must be therefore corrected by the factor $1/(2P - 1)$ in order to get the true asymmetry – the same factor will multiply the

Table 5.2: The dependence of the charge reconstruction results on the charge difference cut. QCDFF prediction for b events with $\gamma = 1$. Errors are statistical only.

$q^+ - q^-$ cut	charge identification probability P	fraction of events left	$\frac{1}{2P-1}$
0.00	0.7150 ± 0.0061	1.0000	2.33
0.05	0.7393 ± 0.0063	0.8818 ± 0.0043	2.09
0.10	0.7589 ± 0.0065	0.7716 ± 0.0056	1.93
0.15	0.7833 ± 0.0068	0.6646 ± 0.0063	1.76
0.20	0.8062 ± 0.0071	0.5576 ± 0.0067	1.63
0.25	0.8254 ± 0.0075	0.4650 ± 0.0067	1.54
0.30	0.8428 ± 0.0079	0.3856 ± 0.0065	1.46
0.40	0.8754 ± 0.0088	0.2533 ± 0.0058	1.33
$q^+q^- < 0$	0.7855 ± 0.0074	0.5543 ± 0.0067	1.75

statistical error of the measurement. For $P = 0.7$ (as given by the jet weighted jet charge method) this would mean an error increase by a factor 2.5. It was therefore checked if it were possible to increase the charge reconstruction probability, even at a cost of some loss in the number of events.

One obvious way to attempt to increase P is to accept only events in which the measured charges of both jets have opposite signs. This method of increasing the probability was often applied by experiments using the weighted charge method. In the special case of this analysis: using $\gamma = 1$ for the b events the QCDFF Monte-Carlo predicts a loss of 44% of events through this requirement, and the probability of correct charge assignment of 0.7855 ± 0.0074 among the remaining ones (to be compared with 0.7160 before the cut).

Another way to increase the charge identification probability would be to exclude events with low difference between the jet charges. The charge assignment in an event with small charge difference can be easily reversed by measurement errors – leaving these events out could increase the reliability of the method. Table 5.2 shows the results of applying the charge difference cut to the QCDFF Monte-Carlo events. The results shown were obtained for b events, using the exponent $\gamma = 1$. For comparison, the result obtained with the "opposite charge" requirement is also displayed. The table shows, that it is more advantageous to cut on the charge difference than to require that the events have opposite charges. It shows also, that the cut gives only modest increase of the identification probability, while the price paid in the number of events lost is quite high. In the further course of the analysis it was seen that an additional cut on the jet charge difference could reduce the statistical error on the measured asymmetry by at best 10%. In view of additional contribution to the systematic error introduced, it was decided not to apply any cuts on the jet charges in the analysis.

To complete the considerations about charge identification, a word about the effect of neutral B mixing on the results is needed. As was already said, the methods which use leptons for charge identification are sensitive to the $B - \bar{B}$ oscillations, if the mixing between neutral B's would be maximal, the lepton tag would be able to identify the B quark charge only in charged B decays. The weighted charge method was from the beginning designed to use the event fragmentation history to tag the quark charge, and should be basically insensitive to mixing phenomena, which occur long after the fragmentation has finished. One can for example check that in the s quark jets the $K^0 - \bar{K}^0$ mixing will not affect the charge reconstruction - this because the K^0 decays into charged particles are symmetric.

The B^0 case is however not that simple. The B^0 decay proceeds via an intermediate charm state, and is thus not completely charge symmetric. It can therefore be expected that the mixing affects the charge reconstruction. Still, the effect expected is smaller than in the lepton tag. An additional safety factor comes from the fact, that the weighted charge method always compares the two jets in an event – therefore a change on one event side does not necessarily produce the wrong answer.

One can roughly estimate the effect of mixing on the asymmetry measured with jet charge tagging. Taking the upper limits on the mixing parameters from the experiments [7], and making reasonable assumption about numbers of various B species in the fragmentation products, one can estimate that in at most 20% of events a $B - \bar{B}$ transition occurs. Assuming that 30% of those events will get their jet charge assignment changed (which is probably the worst case) this would result in reducing the measured asymmetry by at most 6%. It was therefore decided that on the precision level of this experiment the effect can be neglected. However in future high precision analyses one should more carefully evaluate how the jet charge determination is affected by mixing.

5.2.3 Results

Having developed a method for primary quark charge determination, a measurement of the asymmetry was done. The input event sample was taken from the vertex tagging method, with cuts slightly released in comparison to those used in the previous analysis. This decision was taken after it was checked that the increase in the statistical error caused by higher non-b background was offset by improvements from the larger number of events and better knowledge of the sample purity (due to higher number of double tags). The actual cuts used were:

$$S > 4.5 \qquad \epsilon < 23^\circ \qquad Q > -1.5.$$

These cuts selected 979 tagged events – the double tag method told that out of those $59 \pm 6\%$ are $b\bar{b}$ production events. The charm content was estimated to 21%.

In the next step a distribution of the polar direction of the positive jet axis was found (figure 5.17). The sphericity axis was used as jet axis. As in the TASSO coordinate system the electron goes in the *negative* z direction, this is the distribution of the angle between the incoming electron and outgoing negative quark. Therefore for the $Q = -1/3$ quarks this is directly the asymmetry plot, while for the $Q = 2/3$ ones this is a "reversed plot" (showing the outgoing antifermion). For comparison a $1 + \cos^2\theta$ function is also plotted.

The next step was to calculate the asymmetry of this distribution. Several methods can be used in principle for this purpose, a review of various methods can be found in [61]. For this analysis the maximum likelihood method was chosen. The idea of the maximum likelihood fit is to maximise the joint probability function

$$L = \prod_{i=1}^{n} P(x_i)$$

where $P(x)$ is the probability density function for the measurement ($P(x)dx$ is the probability of obtaining in a single measurement the value between x and $x + dx$) and the product extends

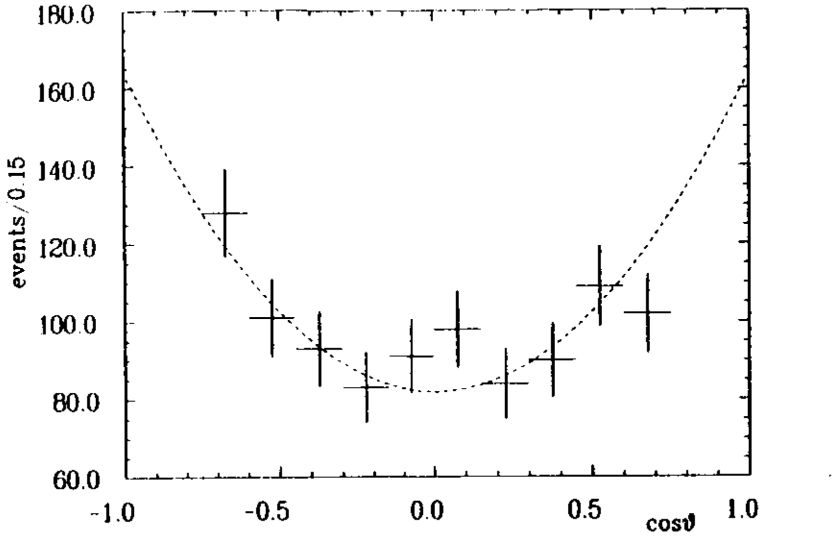

Figure 5.17: The $\cos\theta$ distribution of the positively charged jet direction in the tagged sample. Dashed line shows the symmetric distribution $1 + \cos^2\theta$.

over all the measurement results x_i. In the particular case $x = \cos\theta$ and $P(x)$ has the form

$$P(x) = \frac{\left(1 + x^2 + \frac{8}{3}Ax\right) E(x)}{\int_{-1}^{1} \left(1 + x^2 + \frac{8}{3}Ax\right) E(x)dx}$$

$E(x)$ is here the detector acceptance function and A is the asymmetry (to be determined). One can thus construct the log likelihood for the given set of measurements $x_i = \cos\theta_i$

$$l(A) = \log L = \sum_{i=1}^{n} \log\left(1 + x_i^2 + \frac{8}{3}Ax_i\right) + \sum_{i=1}^{n} \log(E(x_i)) - n\log\int_{-1}^{1}(1 + x^2 + \frac{8}{3}Ax)E(x)dx$$

In this formula the second term does not depend on A, and can therefore be dropped in maximum finding. Moreover, if $E(x)$ is an even function (as it is in the case of a symmetric detector) then also the integral does not depend on A and can be dropped. The problem is thus limited to finding a maximum of the function

$$l = \sum_{i=1}^{n} \log\left(1 + x_i^2 + \frac{8}{3}Ax_i\right)$$

or, equivalently, to the problem of solving an equation

$$\frac{dl}{dA} = \frac{8}{3}\sum_{i=1}^{n} \frac{x_i}{1 + x_i^2 + \frac{8}{3}Ax} = 0$$

which is an easy numerical task. Also the estimate of the variance of A is easy to find - it can be shown [62] that

$$\sigma^2(A_0) = \frac{1}{l''(A_0)}$$

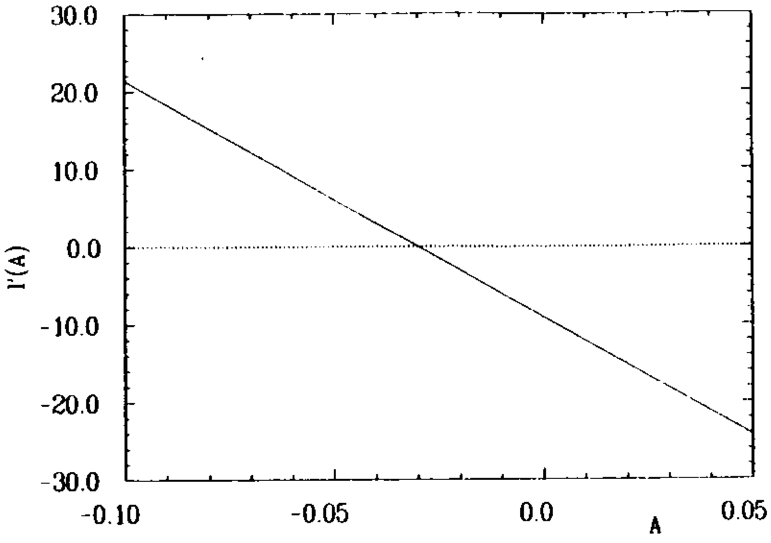

Figure 5.18: Derivative of the log likelihood function as a function of A for the tagged events from figure 5.17.

is an asymptotically unbiased estimator of the variance (in the limit $n \to \infty$). The main advantage of the maximum likelihood method is thus that it does not require knowledge about the acceptance function $E(x)$ - most of the other methods need it at least for variance estimation.

Figure 5.18 shows the first derivative of the log likelihood l' as a function of the assumed asymmetry A. It is seen that the derivative is to a very good approximation a linear function of A - this means that the asymptotic behaviour has been reached and the likelihood function itself is very well approximated by a gaussian curve. The asymmetry read from this plot was

$$A_{raw} = -0.0300 \pm 0.0352.$$

This value is a combination of individual quark contributions. The contributions to the asymmetry add linearly, so one can write

$$A_{raw} = \sum_i f_i(2P_i - 1)A_i$$

where the sum is over quark flavours, f_i is the fraction of events with primary quark flavour i in the sample, A_i is the asymmetry contribution from this flavour, and P_i is the probability of correct charge assignment. This formula was used to extract the b asymmetry. In order to be able to do it, one has to assume that the asymmetries for other flavours are as given by the standard model. Doing this, taking the f's from the double tag prediction (with an assumption added that the $u : d : s$ ratio is $4 : 1 : 1$) and the P's from table 5.1 the following result was obtained:

$$A_{bb} = -0.14 \pm 0.14$$

The various sources contributing to the systematic error on $A_{b\bar{b}}$ are listed in table 5.3 together with their estimated contributions.

Table 5.3: Contributions to the systematic error on $A_{b\bar{b}}$.

Source	Contribution
b content of the tagged sample	±0.025
flavour composition of the background events	±0.020
model dependencies of the charge identification probabilities for light flavours	±0.011
error on the probability of charge identification in the b events	±0.005
errors on the predicted asymmetries of the light flavours	±0.005

Adding the above systematic contributions in quadrature a total systematic error of ±0.04 was obtained. The final result is thus

$$A_{b\bar{b}} = -0.14 \pm 0.14 \pm 0.04$$

consistent with the standard model predictions. The result compares also well to the other measurements and has a smaller error then most of the lepton methods (with exception of the JADE [46] result). The error is dominated by the sample statistics – this could be improved by more data, but also by a more precise vertex detector. The method can be thus seen as potentially very powerful.

Summary of the Asymmetry Measurement

A tagged b event sample of about 1000 events with an estimated $b\bar{b}$ content of 59 ± 6% has been used to measure the forward-backward asymmetry in the b quark production. The quark charge was identified using a method based on a weighted jet charge. The measured asymmetry value is

$$A_{b\bar{b}} = -0.14 \pm 0.14\,(\text{stat.}) \pm 0.04\,(\text{syst.})$$

to be compared with the Standard Model prediction of

$$A_{b\bar{b}}^{pred} = -0.242 \pm 0.015 \pm 0.015.$$

Bibliography

[1] S.W. Herb et al., Phys. Rev. Lett. 39 (1977) 252.

[2] DASP II Collaboration, C.W. Darden et al., Phys. Lett. 76B (1978) 246,
PLUTO Collaboration, C. Berger et al., Phys. Lett. 76B (1978) 243,
DASP II Collaboration, C.W. Darden et al., Phys. Lett. 78B (1978) 364,
DESY-Heidelberg Collaboration, J.K. Bienlein et al., Phys. Lett. 78B (1978) 360.

[3] C. Behrends et al. (CLEO Collaboration), Phys. Rev. Lett. 50 (1983) 881.

[4] ARGUS Collaboration, H. Albrecht et al., Phys. Lett. B185 (1987) 218.

[5] C. Bebek et al. (CLEO Collaboration), Phys. Rev. D36 (1987) 1289.

[6] ARGUS Collaboration, H. Albrecht et al., Phys. Lett. 192B (1987) 245.

[7] W. Schmidt-Parzefall, talk,in 'Proceedings of the 1987 Internationl Symposium on Lepton and Photon Interactions at High Energies', Nucl. Phys. B (Proc. Suppl.) 3 (1988) 257.

[8] S. L. Wu, talk, in 'Proceedings of the 1987 Internationl Symposium on Lepton and Photon Interactions at High Energies', Nucl. Phys. B (Proc. Suppl.) 3 (1988) 39.

[9] C. Peterson et al., Phys. Rev. D27 (1983) 105.

[10] DELCO Collaboration, M. Sakuda et al., Phys. Lett. 152B (1985) 399.

[11] TASSO Collaboration, W. Braunschweig et al., DESY preprint 88-112, to be published.

[12] A. Piwinski, IEEE Trans. V. NS-30, No. 4 (1983) 2378.

[13] C. Youngmann, Ph.D thesis, Imperial College, London 1980.

[14] S. Jaroslawski, Nucl. Instr. Meth. 176 (1980) 261.

[15] H. Boerner et al., Nucl. Instr. Meth. 176 (1980) 151.

[16] H. Boerner, Ph.D thesis, Universität Bonn, 1981.

[17] D.M. Binnie et al., Nucl. Instr. and Meth. 228 (1985) 267.

[18] D. Su, Ph.D thesis, Imperial College, London, 1987.

[19] D.G. Cassel, H. Kowalski, DESY 80/107 (1980).

[20] W. Schütte, Ph.D thesis, Universität Hamburg, DESY Internal report F1-84/3 (1984).

[21] A.J. Campbell, Ph.D thesis, Imperial College, London (1983).

[22] Nijenhuis an Wilf, Combinatorical Algorithms, Academic Press 1984.

[23] D. Strom, Ph.D thesis, University of Wisconsin, Madison 1986.

[24] M. Hildebrandt, Internal TASSO note #329, unpublished.

[25] D.H. Saxon, Nucl. Instr. Meth. A234 (1985) 258.

[26] TASSO Collaboration, M. Althoff et al., Z. Phys. C22 (1984) 307.

[27] The program was written by G. Rudolph.

[28] K. Fabricius et al., Z. Phys. C11 (1982) 315.

[29] TASSO Collaboration, M. Althoff et al., Z. Phys. C26 (1984) 157.

[30] R.D. Field and R.P. Feynmann, Nucl. Phys. B136 (1978) 1.

[31] J. Izen, Internal TASSO note #322, unpublished.

[32] T. Sjöstrand, Comput. Phys. Comm. 39 (1986) 347,
T. Sjöstrand, M. Bengtsson, Comput. Phys. Comm. 43 (1987) 367.

[33] R.K. Ellis, D.A. Ross, A.E. Terrano, Nucl. Phys. B178 (1981) 421.

[34] B. Andersson et al., Phys. Rep. 97 (1983) 31.

[35] K. Genser, Internal TASSO note #366, unpublished.

[36] P. Burrows, Internal TASSO Note #375, Publication in preparation.

[37] F.A. Berends, R. Kleiss Nucl. Phys. B178 (1981) 141.

[38] TASSO Collaboration, M. Althoff et al., Phys. Lett. 136B (1984) 130.

[39] JADE Collaboration, W. Bartel et al., Phys. Lett. 146B (1984) 121.

[40] DELCO Collaboration, H. Yamamoto et al., Phys. Rev. Lett. 54 (1985) 522.

[41] M. Derrick et al. (HRS Collaboration), Phys. Rev. Lett. 53 (1984) 1971.

[42] DELCO Collaboration, H. Aihara et al., Z. Phys. C27 (1985) 39.

[43] MARK-J Collaboration, B. Adeva et al., Phys. Rev. Lett. 51 (1983) 443.

[44] P. C. Rowson et al. (MARK-II Collaboration), Phys. Rev. Lett. 54 (1985) 2580.

[45] TASSO Collaboration, M. Althoff et al., Phys. Lett. 149B (1984) 524.

[46] JADE Collaboration, W. Bartel et al., Phys. Lett. 146B (1984) 437.

[47] W. Hoffmann et al., in 'Proceedings of the workshop on e^+e^- Physics at high Luminosities' SLAC 283 (1985) 35.

[48] TASSO Collaboration, M. Althoff et al., Z. Phys. C22 (1984) 219.

[49] E. Wicklund, Ph.D thesis, University of Wisconsin (1984).

[50] TASSO Collaboration, M. Althoff et al., Phys. Lett. 146B (1984) 443.

[51] J. Chwastowski, private communication.

[52] R. Giles et al. (CLEO Collaboration), Phys. Rev. D30 (1984) 2279.

[53] JADE Collaboration, W. Bartel et al., Phys. Lett. 114B (1982) 71.

[54] P. Jenni, talk, in 'Proceedings of the 1987 Internationl Symposium on Lepton and Photon Interactions at High Energies', Nucl. Phys. B (Proc. Suppl.) 3 (1988) 341.

[55] R. Marshall, Preprint RAL 87-031 (1987).

[56] R.J. Cashmore et al., Z Phys. C30 (1986) 125.

[57] J Jersák, E. Laermann and P.M. Zerwas, Phys. Lett. 98B (1981) 363.

[58] W. W. Ash et al. (MAC Collaboration), Phys. Rev. Lett. 58 (1987) 1080.

[59] W. Zeuner, Ph.D. thesis, Universität Hamburg, DESY internal report F35D-88-01 (1988).

[60] TASSO Collaboration, R. Brandelik et al., Phys. Lett. 100B (1981) 357.

[61] R. Marshall, preprint RAL-84-003 (1984).

[62] S. Brandt, Datenanalyse, 2 Aufl., Bibliographisches Institut Mannheim/Wien/Zürich 1981, pp. 163-176.

Acknowledgements

The analysis presented would not be possible without the effort of many people, who contributed their work to the result presented.

I am deeply indebted to my advisor, prof. Erich Lohrmann for his help and guidance, for the many discussions, and for careful reading of the manuscript.

I express my thanks to dr. Roman Walczak for giving me the idea of this analysis and for guiding me in its early stages.

I am very grateful to prof. J. Zakrzewski for making my trip to DESY possible and for his continuous interest in my work.

Many members of TASSO shared with me their knowledge of physiscs and the detector. In particular I am grateful to dr. B. Löhr, prof. D. Saxon, D. Su, A. Martin, D. Muller and W. Zeuner. Without the many discussions I had with them the analysis would not be complete.

I thank the entire TASSO group for creating a beautiful working atmosphere. In particular I owe much to K. Genser, with whom I shared an office most of the time.

I wish to thank the DESY directoriate for giving me the opportunity of working at the DESY laboratory, for the financial support and for the hospitality extended to me during my stay at DESY.

Finally, I have to thank my wife for her patience, help and 'silent support' she gave me and to my sons for the joy they brought into my life.

Members of the TASSO Collaboration

W. Braunschweig, R. Gerhards, F.J. Kirschfink, H.-U. Martyn
I. Physikalisches Institut der RWTH Aachen, Federal Republic of Germany [a]

B. Bock[1], H.M. Fischer, H. Hartmann, J. Hartmann, E. Hilger, A. Jocksch, R. Wedemeyer
Physikalisches Institut der Universität Bonn, Federal Republic of Germany [a]

B. Foster, A.J. Martin, A.J. Sephton
H.H. Wills Physics Laboratory, University of Bristol, Bristol, UK [b]

E. Bernardi[2], J. Chwastowski[3], A. Eskreys[4], K. Gather, K. Genser[5], H. Hultschig, P. Joos, H. Kowalski, A. Ladage, B. Löhr, D. Lüke, P. Mättig[6], D. Notz, J.M. Pawlak, K.-U. Pösnecker E. Ros, D. Trines, R. Walczak[5], G. Wolf
Deutsches Elektronen-Synchrotron DESY, Hamburg, Federal Republic of Germany

H. Kolanoski
Institut für Physik, Universität Dortmund, Federal Republic of Germany [a]

W. Gerhardt, T. Kracht[8], H.L. Krasemann, J. Krüger, E. Lohrmann, G. Poelz, P. Rehders, G. Tysarczyk, C. Winand, W. Zeuner
II. Institut für Experimentalphysik der Universität Hamburg, Federal Republic of Germany [a]

J. Hassard, J. Shulman, D. Su
Dept. of Physics, Imperial College, London, UK [b]

F. Barreiro, A. Leites, J. del Peso
Universidad Autonoma de Madrid, Madrid, Spain [c]

C. Balkwill, M.G. Bowler, P.N. Burrows, R. Cashmore G.P. Heath, P. Ratoff, I. Silvester, I.R. Tomalin, M.E. Veitch
Dept. of Nuclear Physics, Oxford University, Oxford, UK [b]

G.E. Forden[9], J.C. Hart, D.H. Saxon
Rutherford Appleton Laboratory, Chilton, Didcot, UK [b]

S. Brandt, M. Holder, L. Labarga[10]
Fachbereich Physik der Universität-Gesamthochschule Siegen, Federal Republic of Germany [a]

Y. Eisenberg, U. Karshon, G. Mikenberg, A. Montag, D. Revel, E. Ronat, A. Shapira, N. Wainer, G. Yekutieli
Weizmann Institute, Rehovot, Israel [d]

D. Muller, S. Ritz, D. Strom[11], M. Takashima, Sau Lan Wu, G. Zobernig
Dept. of Physics, University of Wisconsin, Madison, WI, U.S.A. [e]

[1] Now at Krupp Atlas Elektr. GmbH, Bremen, F.R.G.
[2] Now at Robert Bosch GmbH, Schwieberdingen, F.R.G.
[3] On leave from Inst. of Nuclear Physics, Cracow, Poland
[4] Now at Inst. of Nuclear Physics, Cracow, Poland
[5] Now at Warsaw University, Poland
[6] Now at IPP Canada, Carleton University, Ottowa, Canada
[7] On leave from Warsaw University [f], Poland
[8] Now at Hasylab, DESY.
[9] Now at SUNY Stony Brook, Stony Brook, NY, USA
[10] Now at SLAC, Stanford, CA, U.S.A.
[11] Now at University of Chicago, Chicago, IL, U.S.A.

[a] Supported by Bundesministerium für Forschung und Technologie
[b] Supported by UK Science and Engineering Research Council
[c] Supported by CAICYT
[d] Supported by the Minerva Gesellschaft für Forschung GmbH
[e] Supported by US Dept. of Energy, contract DE-AC02-76ER000881 and by US Nat. Sci. Foundation Grant number INT-8313994 for travel.
[f] Partially supported by grant CPBP 01.06